

Structure-reactivity relationships in modified V_xO_y/CeO_2 catalysts for selective catalytic reduction of NO_x

Dissertation

zur Erlangung des akademischen Grades

doctor rerum naturalium (Dr. rer. nat.)

an der Mathematisch-Naturwissenschaftlichen Fakultät

der Universität Rostock

vorgelegt von

Thanh Huyen Vuong, geboren am 24.04.1983 in Thanh Hoa

aus Vietnam

Rostock, 20.03.2017

1. Gutachter Prof. Dr. Angelika Brückner
 Leibniz-Institut für Katalyse e.V. an der Universität Rostock
2. Gutachter Prof. Dr. Wolfgang Grünert
 Lehrstuhl Technische Chemie, Ruhr-Universität Bochum

Tag der Einreichung: 20.03.2017

Tag der mündlichen Aussprache: 04.07.2017

Erklärung

Hiermit erkläre ich, dass ich die vorliegende Arbeit selbstständig verfasst und keine anderen als die angegebenen Quellen und Hilfsmittel benutzt zu habe.

Rostock, 20.03.2017

Thanh Huyen Vuong

Acknowledgment

First of all, I would like to express my sincere appreciation and thanks to my advisor Prof. Dr. Angelika Brückner for giving me the opportunity as a PhD student in her group and especially for the tremendous support and encouragement during my research. I am very grateful to her for invaluable guidance, continuous teaching, affection, and all her contribution of time and ideas, which helped me to learn a lot and strongly motivated me through the rough road to finish my thesis on time. I am also thankful for the excellent example she has provided as a successful woman chemist, professor, and manager.

I would like to acknowledge Dr. Jabor Rabeah for helpful guidance, the experience shared and discussions during my research. At the same time, I also want to thank Dr. Ursula Bentrup for her support, great contribution and feedbacks on the publications. Further thank goes to Dr. Jörg Radnik for the XPS measurements and useful ideas. Special thanks go to PD. Dr. Evgenii Kondratenko, Dr. Sergey Sokolov, and Dr.-Ing.Udo Armbruster for the good collaboration in this research. I gratefully acknowledge Mr. Reinhard Eckelt for useful technical support, help with solving lab problems, as well as BET measurements. Additionally, I would like to send appreciations to Prof. Dr. Wolfgang Grünert for fruitful contribution regarding to activity test at high GHSV measurements, Dr. Matthias Schneider for the valuable advice in relation to X-Ray measurements, Dr. Hanan Atia for H₂-TPR measurements, Dr. Jana Engeldinger and Dr. Nils Rockstroh for Raman spectroscopy experiments, Mrs. Christine Rautenberg for FTIR measurements, Mrs. Anja Simmula for the ICP-OCS measurements, Mr. Ulrich Marx for EPR measurements, and last but not least all other members of analytic group for their direct or indirect help.

I also thank Dr. Roxana Pérez Vélez for all her help during my initial PhD time, and most importantly for becoming one of my close friends. A special thank goes to my office-mates Dr. Dirk Hollmann and Sven Adomeit who have been very supportive in every way. Moreover, I want to thank all other group-mates including Denise Heyl, Andrea Bellmann, Sonja Keller, Reni Grauke, and Thuan Doan for the supportive atmosphere, enjoyable time, kindness, and great parties at LIKAT. Further tributes go to all other members of the workshop, administration and purchasing department of LIKAT for all assistances and the congenial work atmosphere.

I am also grateful for the financial support from Ministry of Education and Training (MOET), Vietnam and LIKAT, and additional support from Hanoi University of Science and Technology, especially Assoc. Prof. Dr. Le Minh Thang throughout my research.

I want to say thank to the Vietnamese community in Rostock for the friendly events we shared together.

Finally, I would like to express my deepest appreciation to my family for all their love, patience, encouragement, and unconditional support throughout my life including the years of PhD studying.

Zusammenfassung

Die selektive katalytische Reduktion (SCR) von Stickoxiden, basierend auf der Umsetzung mit Ammoniak an V_2O_5 - WO_3 / TiO_2 Katalysatoren, ist eine sehr wichtige und etablierte Technologie zur Reinigung von Abgasen aus stationären Quellen. Dieser Prozess benötigt hohe Temperaturen von 300-500 °C. Demgegenüber haben die stickoxidhaltigen Abgase von Diesel- und Magermixmotoren eine deutlich geringere Temperatur. Für deren Reinigung werden Katalysatoren benötigt, die bereits im Bereich von 150-300 °C und bei hohen Raumgeschwindigkeiten (GHSV) aktiv sind.

Ziel dieser Arbeit ist die Entwicklung neuartiger modifizierter $VO_x/Ce_{1-x}M_xO_2$ -Katalysatoren ($M = Zr, Ti, Mn$), die möglichst vollständige Umsätze von NO_x und NH_3 zu N_2 bereits deutlich unter 300 °C bei hohen GHSV ermöglichen. Ein weiteres Ziel lag in der Analyse und Identifizierung der aktiven Zentren, sowie der Aufklärung des Reaktionsmechanismus.

Der Einbau von isovalenten Kationen kleineren Durchmessers auf Ce-Gitterplätzen führte zu einer deutlichen Aktivitätssteigerung der $VO_x/Ce_{1-x}M_xO_2$ im Vergleich zu VO_x/CeO_2 . Gründe liegen in der Verbesserung der Redoxeigenschaften von aktiven V Zentren auf den $Ce_{1-x}M_xO_2$ Träger. Mit den besten $VO_x/Ce_{1-x}Ti_xO_2$ -Katalysatoren konnten vollständige NO - und NH_3 -Umsätze sowie 100%ige N_2 -Selektivität bereits unterhalb von 200 °C bei einer Raumgeschwindigkeit von $GHSV=70,000\ h^{-1}$ erreicht werden. Dies sind Spitzenwerte im Vergleich zum Stand der Literatur.

Verschiedenen Herstellungsmethoden des Trägers, sowie der Einfluss der Co-Komponenten (Zr^{4+} , Ti^{4+} , Mn^{n+}) wurden hinsichtlich der strukturellen Eigenschaften und katalytischen Aktivität untersucht und ausgewertet. Die Analyse der Katalysatoren unter Reaktionsbedingungen mit Hilfe von *in situ* Techniken, wie EPR, UV-Vis-DRS, und DRIFTS-Spektroskopie, ermöglichte die Identifizierung von Struktur-Aktivitäts-Beziehungen. Es zeigte sich, dass an den reinen Trägern und den mit Vanadiumoxid belegten Katalysatoren unterschiedliche Reaktionsmechanismen auftreten. Auf den reinen Trägern verläuft die SCR nach einem Langmuir-Hinshelwood-Mechanismus. Dabei reagiert adsorbiertes Oberflächennitrat mit adsorbiertem Ammoniak. Demgegenüber lagert sich kein oder nur sehr wenig NO_x (mit Mn^{n+}) auf den V-haltigen Katalysatoren ab. In diesem Fall erfolgt die Umsetzung von gasförmigen NO mit adsorbierten NH_3 und NH_4^+ nach einem Eley-Rideal-Mechanismus.

Abstract

Selective catalytic reduction (SCR) of nitrogen oxides by ammonia over V_2O_5 - WO_3/TiO_2 catalysts is a critical and established technology for the purification of exhaust gases from stationary sources. This process requires high temperature (300-500 °C). On the other hand, the nitrogen oxide-containing exhaust gases of diesel or lean-burn gasoline engines have a significantly lower temperature. For reduction these NO_x emissions, catalysts are needed to be already active in the range of 150-300 °C and at high space velocities (GHSV).

The aim of this thesis is to develop novel modified $VO_x/Ce_{1-x}M_xO_2$ catalysts ($M = Zr, Ti, Mn$) that are capable of converting NO_x and NH_3 to N_2 well below 300 °C at a high GHSV. A further goal is to analyse and identify the active centres, as well as to elucidate the mechanism of the reaction.

The incorporation of smaller-diameter isovalent cations on Ce lattice sites led to a marked increase in activity of $VO_x/Ce_{1-x}M_xO_2$ compared to VO_x/CeO_2 . The reason for this is the improvement of the redox properties of active V centres on the $Ce_{1-x}M_xO_2$ supports. With the best $VO_x/Ce_{1-x}Ti_xO_2$ catalysts, full NO and NH_3 conversion with 100% N_2 selectivity could already be achieved below 200 °C at a GHSV of 70,000 h^{-1} . These results are better compared to the literature.

Various methods of preparation of the supports, as well as the influence of the co-components (Zr^{4+} , Ti^{4+} , Mn^{n+}), were investigated and evaluated to study the structural properties and catalytic activity. Furthermore, analysis of the catalysts under reaction conditions using *in situ* techniques, such as EPR, UV-Vis-DRS, and DRIFTS-spectroscopy, allowed the identification of structure-reactivity relationships. It was found that different reaction mechanisms occur on the pure supports and the supported vanadia catalysts. On the pure supports, SCR proceeds via a Langmuir-Hinshelwood mechanism comprising reaction of adsorbed surface nitrates with adsorbed NH_3 . On the other hand, no or negligible NO_x (with Mn^{n+}) is adsorbed on the V-containing catalysts. In this case, the reaction of gaseous NO and adsorbed NH_3 and NH_4^+ follows an Eley-Rideal mechanism.

Contents

Acknowledgment.....	I
Zusammenfassung.....	II
Abstract.....	III
List of abbreviations	VII
1. Motivation and Objective.....	1
2. State of the Art	5
2.1. NO _x emissions and abatement	5
2.2. Selective catalytic reduction of NO _x with NH ₃	7
2.3. Catalysts for low-temperature NH ₃ -SCR of NO _x	9
2.4. Structure-Reactivity relationships of supported vanadia catalysts for NH ₃ -SCR of NO _x	12
2.4.1. Structure of VO _x species	12
2.4.2. Acid-base properties of catalysts and supports.....	14
2.4.3. Redox properties of VO _x surface sites and supports.....	15
2.5. Mechanisms of NH ₃ -SCR of NO _x at low temperature over supported vanadia catalysts.....	16
3. Experimental section.....	19
3.1. Catalyst preparations.....	19
3.1.1. Synthesis of Ce _{1-x} Zr _x O ₂ supports	19
3.1.2. Synthesis of Ce _{1-x} Ti _x O ₂ supports.....	19
3.1.3. Synthesis of Ce _{0.5} Ti _{0.5-x} Mn _x O _δ supports.....	20
3.1.4. Synthesis of supported V ₂ O ₅ catalysts	20
3.2. NH ₃ -SCR activity test.....	21
3.3. Catalyst characterization techniques	22
3.3.1. X-ray diffraction (XRD)	22
3.3.2. Low-temperature N ₂ adsorption	23
3.3.3. Inductively coupled plasma optical emission spectrometry (ICP-OES) ..	25
3.3.4. Temperature programmed reduction by H ₂ (H ₂ -TPR)	25
3.3.5. X-ray photoelectron spectroscopy (XPS)	25
3.3.6. Electron paramagnetic resonance (EPR) spectroscopy	26
3.3.7. UV-Vis diffuse reflectance spectroscopy (UV-Vis-DRS).....	30
3.3.8. Diffuse reflectance infrared Fourier transform spectroscopy (DRIFTS) ..	32
3.3.9. Raman spectroscopy	33

4.	$V_2O_5/Ce_{1-x}Zr_xO_2$ catalysts	35
4.1.	Effect of Zr content on the DeNO _x catalytic performance of $V/Ce_{1-x}Zr_xO_2$ catalysts	35
4.2.	Phase composition, the structural and surface properties.....	36
4.3.	Behaviour of VO _x species in the presence of reactants	42
4.4.	Conclusions.....	48
5.	$V_2O_5/Ce_{1-x}Ti_xO_2$ catalysts.....	49
5.1.	Catalytic performance of $V_2O_5/Ce_{1-x}Ti_xO_2$	49
5.2.	Effect of Ti on the structure and redox properties of $V_2O_5/Ce_{1-x}Ti_xO_2$ catalysts	52
5.2.1.	Physicochemical properties of $V_2O_5/Ce_{1-x}Ti_xO_2$ catalysts	52
5.2.2.	Structure and redox behaviour of VO _x species visualised by <i>operando</i> EPR and pseudo- <i>in-situ</i> -XPS	58
5.3.	Mechanism of NH ₃ -SCR over $Ce_{1-x}Ti_xO_2$ and $V_2O_5/Ce_{1-x}Ti_xO_2$ catalysts	61
5.4.	Conclusions.....	66
6.	$V_2O_5/Ce_{0.5}Ti_{0.5-x}Mn_xO_{2-\delta}$ catalysts	69
6.1.	Catalytic behaviour of $Ce_{0.5}Ti_{0.5-x}Mn_xO_{2-\delta}$ in the presence and absence of V	69
6.2.	Structure-reactivity relationships and active sites.....	70
6.2.1.	Catalyst characterization	70
6.2.2.	<i>In-situ</i> investigation of active sites	75
6.3.	Conclusions	83
7.	Effect of preparation methods of supports on structure and performance of VO _x /CeO ₂ catalysts.....	85
7.1.	Catalytic performance	85
7.2.	Catalyst characterization	86
7.3.	<i>In-situ</i> investigation of the formation and structure of active moieties	88
7.4.	Conclusions.....	91
8.	General conclusions and outlook.....	93
	References	97
	Appendix.....	A1
	Scientific publications	A17

List of abbreviations

a.u.	A rbitrary u nits
BET	B runauer- E mmet- T eller
CP	C o- p recipitation
CTAB	Hexadecyltrimethylammonium b romide
cw	C ontinuous w ave
DFT	D ensity f unctional t heory
DR	D iffuse reflectance
DRIFTS	D iffuse reflectance infrared F ourier t ransform spectroscopy
EPR	E lectron p aramagnetic resonance
Eq.	E quation
E-R	E ley- R ideal
EXAFS	E xtended X -ray a bsorption fine s tructure
FTIR	F ourier t ransform infrared
GC	G as chromatography
GHSV	G as h ourly s pace v elocity
hfs	H yperfine s tructure
H ₂ -TPR	H ydrogen t emperature- p rogrammed reduction
ICDD	I nternational C entre for D iffraction D ata
ICP-OES	I nductively c oupled p lasma o ptical e mission spectrometry
IRAS	I nfrared r eflection a bsorption s pectroscopy
L-H	L angmuir- H inshelwood
LMCT	L igand m etal c harge t ransfer
MS	M ass s pectrometry
NH ₃ -SCR	S elective c atalytic r eduction of NO _x with NH ₃
NMR	N uclear m agnetic r esonance
ODH	O xidative h ydrogenation
OSC	O xygen s torage c apacity
PES	P hotoelectron s pectroscopy
STM	S canning t unnelling m icroscopy
TPD	T emperature p rogrammed d esorption

TPSR	T emperature p rogrammed s urface r eaction
TRM	T ransient r esponse m ethods
TWCs	T hree- w ay c atalysts
UV-Vis	U ltraviolet- v isible
UV-Vis-DRS	D iffuse r eflectance u ltraviolet- v isible s pectroscopy
wt. %	W eight percentage
XANES	X -ray a bsorption n ear e dge s tructure
XPS	X -ray p hotoelectron s pectroscopy
XRD	X -ray d iffraction

1. Motivation and Objective

Motivation

The combustion of fossil fuels used in power plants, vehicles, and factories is one of the largest contributions to air pollution.² The exhaust air pollutants consist of sulphur oxides, carbon monoxide, particulate matter, unburned hydrocarbons and nitrogen oxides (NO_x). Among them, NO_x are considered the primary pollutants causing a variety of environmental problems such as acid rain, photochemical smog, ozone depletion, fine particulate pollution and even accelerated global warming.²⁻⁵ Increasing requirements for reducing NO_x emissions have stimulated interest in the improvement of currently used methods and development of new technologies for NO_x emission control. Depending on the type of NO_x emission source, three primary techniques for NO_x control are available: fuel control, combustion control, and post-combustion control. Selective catalytic reduction with NH₃ (NH₃-SCR), in which ammonia is used as the reducing agent of NO_x in the presence of a catalyst, is one of the most popular post-combustion techniques to control NO_x emission from combustion processes.⁶⁻⁷

Commercial NH₃-SCR catalysts used for cleaning flue gases from power plants are based on V₂O₅-WO₃/TiO₂ oxides which, however, operate only in a rather high and narrow temperature range of 300-500 °C. The temperature of NO_x-containing exhaust gases from other sources such as diesel or lean-burn gasoline engines is much lower.⁸ Therefore, the improvement of commercial vanadium-based catalysts and/or the development of new NH₃-SCR catalysts being sufficiently active and selective at low temperature is a scientific and technological need for NO_x emission control. Since vanadium-based catalysts have numerous advantages, for example, high conversion efficiency, high N₂ selectivity, excellent resistance to sulphur, and low cost, these catalysts bear a significant potential for low-temperature NH₃-SCR if appropriate supports are used to extend the temperature working window. Furthermore, copper-exchanged zeolites are beginning to be used as promising catalysts for diesel vehicles; however, their limited hydrothermal stability and N₂ selectivity are disadvantages for applications.⁹⁻¹¹

Among the wide variety of catalysts tested in recent years, those based on (modified) ceria have proved to be the most promising ones.¹²⁻¹⁴ With MnO_x as co-component, almost total NO conversion has been obtained at 100 °C.¹⁵⁻¹⁶ However, such catalysts suffer from undesired N₂O formation and deactivation by other flue gas components such as SO₂ or H₂O. CeO₂ reveals to be a useful catalyst component not only for SCR but also for other redox reactions since it can store and release oxygen efficiently by a relatively facile reduction from Ce⁴⁺ to Ce³⁺.¹⁷⁻¹⁹ This property is promoted even more when isovalent metal cations of

smaller diameter such as Zr^{4+} or Ti^{4+} are incorporated in Ce lattice positions,²⁰⁻²¹ since doping with such kind of cations can create both short and long metal-oxygen bonds. Thus, the oxygen atoms bonded by long bonds to the metal become weaker and easier to remove. For this reason, SCR catalysts based on ceria-containing mixed oxide supports are almost always expected to be more active than those based on pure ceria.

The mechanism of NH_3 -SCR over vanadia-containing catalysts reported in the literature usually assumes that acidic sites are needed for facilitating ammonia adsorption. However, the question remains to decide which kind of acidic sites is responsible for the ammonia adsorption. Some authors believed that Lewis sites are preferred for this purpose,²²⁻²³ others proposed that it is the Brønsted–OH surface groups,²⁴⁻²⁵ or both Lewis and Brønsted sites on which NH_3 is adsorbed.^{14, 26-27}

In contrast to the ammonia adsorption, there is a significantly different point of view for the adsorption of NO, which was considered to depend on the supports and the oxidation state of vanadium. In this regard, NO was found to adsorb significantly on V_2O_5 /activated semi-coke,²⁸ V_2O_5 – $\text{CeO}_2/\text{TiO}_2$,²⁹ and reduced $\text{V}_2\text{O}_5/\text{TiO}_2$ catalysts but weakly on the oxidised $\text{V}_2\text{O}_5/\text{TiO}_2$ catalyst.³⁰

Moreover, different opinions exist about the role of redox-active sites. Both, a $\text{Ce}^{4+}/\text{Ce}^{3+}$ or a $\text{V}^{5+}/\text{V}^{4+}$ redox cycle and even the participation of V^{3+} have been discussed.³¹ Furthermore, it has been controversially debated whether a Langmuir-Hinshelwood (L-H)³² or an Eley-Rideal (E-R) mechanism³³⁻³⁴ is relevant. In order to clarify these issues for modified VO_x/CeO_2 systems, detailed spectroscopic *in-situ* studies are needed to address both the interaction of feed components with surface adsorption sites and changes of the valence states of metal ions in the catalyst. Information on how the replacement of Ce in CeO_2 by other metal ions and the synthesis method of supports can affect the structural properties of vanadium catalysts as well as their catalytic behaviour is accessible only by the combination of suitable *in-situ* spectroscopies under real catalytic reaction conditions.

Objective

As explained above, there is an urgent need to improve the activity of NH_3 -SCR de NO_x catalysts at low temperature. It is the aim of this PhD thesis to explore whether this is possible with supported $\text{VO}_x/\text{Ce}_{1-x}\text{M}_x\text{O}_2$ catalysts in which metal ions of smaller size than Ce^{4+} and different redox potential ($\text{M} = \text{Zr}, \text{Ti}, \text{Mn}$) replace Ce in its lattice positions to improve the redox behaviour of the catalysts. Moreover, the influence of these metal ions on structure-reactivity relationships and the mechanism of the NH_3 -SCR reaction would be investigated by a combination of different *in-situ/operando* spectroscopies. To this end, the following synthesis strategies have been employed:

- incorporation of Zr into CeO₂ (Chapter 4)
- incorporation of Ti into CeO₂ (Chapter 5)
- Mn doping of the Ce_{0.5}Ti_{0.5}O₂ support (Chapter 6)
- use of different methods for the synthesis of supports (Chapter 7)

Among the various spectroscopic techniques, *in-situ* electron paramagnetic resonance (EPR) spectroscopy has been applied to monitor and discern different VO_x species and their redox behaviour during NH₃-SCR. Pseudo-*in-situ* X-ray photoelectron spectroscopy (XPS) and *in-situ* ultraviolet-visible in diffuse reflectance mode (UV-Vis-DRS) spectroscopy were applied to follow changes in the oxidation state of catalyst components under reaction conditions. Furthermore, *in-situ* infrared spectroscopy in diffuse reflectance mode (DRIFTS) was performed to reveal the interaction of reactants with the catalyst surface as well as to identify intermediates and reaction mechanisms. Standard characterization methods such as nitrogen adsorption at low temperature (BET), inductively coupled plasma optical emission spectrometry (ICP-OES), hydrogen temperature programmed reduction (H₂-TPR), X-ray diffraction (XRD), and Raman spectroscopy were also applied. In the combination of these techniques, a comprehensive picture of the phase compositions and surface properties of the catalysts has been derived, and the role of these properties in the performance and stability of the catalysts is discussed.

2. State of the Art

2.1. NO_x emissions and abatement

Nitrogen oxides exist in the environment in various species such as N₂O, NO, NO₂, N₂O₃, N₂O₄, and N₂O₅.² By definition, the abbreviation NO_x is used for nitric oxide (NO) and nitrogen dioxide (NO₂). They are considered to be toxic and harmful gases although nitric oxide is less toxic than nitrogen dioxide. NO is unstable and reacts readily with O₂ to form NO₂ which can be a source of the acute pulmonary disease even in small doses.³⁵ It has been previously shown in some studies on the risk assessment that high concentration of outdoor NO₂ in residential areas contributes to increasing respiratory and cardiovascular diseases and mortality. Additionally, NO_x and many volatile organic compounds are regarded as smog precursors which react together in the presence of heat and sunlight to form photochemical smog. Also, NO and NO₂ along with sulphur dioxide (SO₂) mainly contribute to acid rain, which can severely damage the ecosystems, for example, by deforestation, soil and water acidification. Acid rain can also cause material losses such as destruction of building and crop damage. N₂O is known as one of the greenhouse gases, which can absorb infrared radiation at a 270 times higher intensity than carbon dioxide (CO₂). N₂O participates in complex reactions in the stratosphere, which can lead to a depletion of the ozone layer.^{2-4, 36} Besides, it indirectly affects the ozone layer through photochemical reactions.³⁷ Unlike NO and NO₂, N₂O has a long half-life around 100 to 150 years since it is not highly reactive.

NO_x is discharged into the atmosphere from natural and anthropogenic sources. Anthropogenic sources comprise fossil fuel combustion of automobiles, power plants or industrial processes. NO_x stems partly from nitrogen compounds, but mostly from atmospheric nitrogen oxidation at high temperatures. It is also naturally produced by lightning, volcanic activities, and biomass burning from forest fires, and to a small extent by microbial processes in soils.^{2, 38} The largest anthropogenic NO_x emissions are contributed by China (about 21,546 Gg per year), which is almost twice the emissions produced by the United States (14,687 Gg) and European Union (10,074 Gg).³⁹ In the United States and the European Union, approximately 50% of total anthropogenic NO_x emissions are emitted from mobile sources. In the emerging countries such as China, power production and industrial processes are the primary NO_x sources, for example, in 2008, about 8209 Gg and 6598 Gg were discharged from power production and industrial process, respectively. Although the levels of NO_x are still prominent, Western countries achieved a gradual reduction in NO_x emission. The environmental protection agency in the USA also reported that a decrease of about 60% in the US national average of NO₂ had been achieved in 30 years. However, reducing NO_x emission is one of the main challenges faced by the

emerging countries like China, where the total emissions grew from 9071 Gg in 1995 to 22,679 Gg in 2010.³⁹⁻⁴⁰

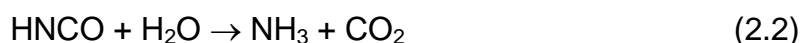
Of the emitted NO_x from vehicles, around 80% is created by diesel-powered vehicles, for which the proportion of harmful NO_2 is much higher than that coming from petrol cars.³⁵ Over the past years, increasing strict vehicle emission standards (i.e. the so-called 'Euro' standards) have been introduced in Europe to limit the extent of air pollution from vehicles. The Euro 1 standard was adopted in 1992 as a final rule, which required the fitting of catalytic converters to petrol cars to reduce carbon monoxide (CO), hydrocarbons (HC) and NO_x emissions. The latest standard, Euro 6, applied to all new vehicles from September 2015, which requires a further drastic drop of NO_x emitted by diesel engines down to a maximum of 80 mg/km. This value is much lower than the level (180 mg/km) that was required for diesel cars to meet the previous Euro 5 standard. The limit for NO_x from petrol cars remains at 60 mg/km, which is similar to the Euro 5 standard.

In view of the urgent regulations of NO_x emissions, many technologies including fuel control, combustion control and post-combustion control have been developed, and are commercially available for monitoring and abatement of NO_x .^{2, 41-42} The fuel control techniques aim at minimization of the nitrogen contained in the fuels before the combustion process by using ultra-low nitrogen fuel like ethanol, natural gas instead of diesel oil, or pure oxygen instead of air. Combustion control technologies can reduce NO_x formation during the combustion process by altering or modifying the firing conditions. Therefore, the primary objectives of these techniques are to create a fuel rich condition at the maximum flame temperature, to reduce the flame temperature or to vary the residence time within different parts of the combustion zone. However, the effectiveness of combustion control technologies strongly depends on the type of the combustion system. In general, about 30-70% NO_x reduction can be obtained. Only for gas turbines, higher efficiencies of 70-85% can be achieved.³ Post-combustion methods or after-treatment methods comprise the selective reduction of NO_x formed in exhaust gases from incineration processes. Post-treatment methods can be categorised into two groups taking into account the type of control approach: NO_x removal from flue gas and NO_x destruction.⁴³ In the first method, absorption or adsorption processes are used to remove NO_x , taking advantage of the better solubility of NO_x at high concentration.⁴⁴ Therefore, this method is mainly applied to reduce NO_x emission from industrial processes, for example, nitric acid or oxalic production. However, the formation of nitrates and other potential water pollutants, and expensive equipment requirements are the main disadvantages of this method. The second approach prevents such drawbacks since NO_x is usually transformed to N_2 by selective catalytic reduction with ammonia, urea or cyanuric acid.^{2, 45}

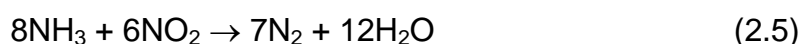
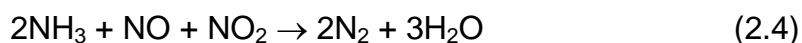
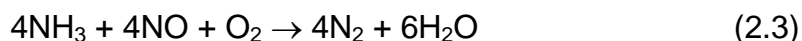
On the other hand, projections for road transport growth and vehicle ownership for the next few decades have also motivated the development of other technologies. For example, hybrid vehicles are designed as a combination of a combustion engine and an electric motor. These vehicles can reduce emissions substantially. Fuel cell and hydrogen hybrid vehicles have near-zero emissions.⁴⁶ However, as these emerging technologies are still expensive and require a reliable supply of electricity or hydrogen, they are not expected to play an important role soon. Therefore, traditional vehicles with catalytic converters using NO_x storage and reduction and selective catalytic reduction to reduce NO_x emissions are still the most attractive because of their low cost and high efficiency.

2.2. Selective catalytic reduction of NO_x with NH₃

Selective catalytic reduction of NO_x with NH₃ (NH₃-SCR) is one of the most popular post-combustion techniques to control NO_x emission from combustion processes. This technology was first developed in Japan in the 1970s and is today worldwide applied in stationary sources and diesel vehicles.^{2, 47-49} Generally, NH₃-SCR comprises reaction NO_x with ammonia to N₂ and water in the presence of oxygen by the promotion of a suitable catalyst. For mobile applications, storage of ammonia in pressurised vessels inside the vehicle is not practicable because of the toxicity of ammonia. For those requests, NH₃ is replaced by urea tanks. The required amount of ammonia is released by decomposing aqueous urea:⁶

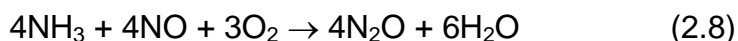
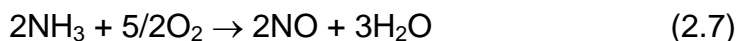
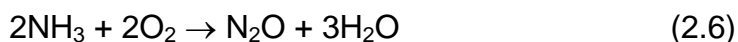


The NH₃-SCR process is described by the following reactions:



Reaction (2.3) is the so-called standard SCR reaction which typically works well at high temperatures (300-500 °C) in the presence of oxygen and constitutes the overall stoichiometry of the reaction (NH₃/NO = 1/1). This reaction can proceed faster when a 1:1 mixture of NO and NO₂ reacts with NH₃ (Eq. 2.4), which is referred to as “fast SCR”, due to the stronger oxidizing ability of NO₂ compared to that of O₂.^{6, 48} When the feed contains only NO₂, the reaction with NH₃ is called “NO₂-SCR” (Eq. 2.5). Since the investigations in this thesis are focused on standard SCR only, the following description of state of the art is restricted to this reaction.

Frequently, the N_2 selectivity in NH_3 -SCR is limited by undesired NH_3 oxidation giving rise to N_2O and/or NO (Eq. 2.6-2.8), which depends on the catalyst and is usually most pronounced at high temperature.⁶



Moreover, N_2O can arise from NO alone (Eq. 2.9-2.10):



Since the early 1970s, various catalytic materials have been developed for the SCR of NO_x to meet the stringent regulation of NO_x reduction.⁵ The most popular NH_3 -SCR catalysts used for cleaning flue gases from power plants are V_2O_5 - WO_3 / TiO_2 oxides which, however, operate only in a rather high and narrow temperature range of 300-500 °C.⁵⁰⁻⁵¹ The temperature of NO_x -containing exhaust gases from other sources such as diesel or lean-burn gasoline engines is much lower around 150-300 °C.^{8, 52} Moreover, it should be considered that catalytic performance at low temperatures commonly is affected by several deactivations from the permanent presence of SO_2 and water vapour in flue gases even after the desulphurization. The competitive adsorption between H_2O and reactants, for example, NH_3 and NO or the formation of additional surface hydroxyls created by dissociative adsorption or decomposition of H_2O on the catalyst surface. This effect results in a decrease of available active sites leading to the partial deactivation of catalysts. On the other hand, the oxidation of SO_2 creates SO_3 which can combine with NH_3 and H_2O to form sulfur-containing species, resulting in the corrosion and plugging of equipment. Moreover, these sulfur-containing species also can cover the active sites on the catalyst surface, leading to the deactivation of catalysts.^{16, 21, 53} Another important issue for mobile applications is that catalysts need to be active under high gas hourly space velocity (GHSV) conditions but at low-pressure drop due to the restricted volume of catalytic converters in engines. Therefore, the development of new NH_3 -SCR catalysts being sufficiently active and selective at temperatures well below 300 °C, at high GHSV and high stability against SO_2 and H_2O is crucial for NO_x emission control.

2.3. Catalysts for low-temperature NH₃-SCR of NO_x

Many catalysts have already been investigated for low-temperature NH₃-SCR.^{8, 16, 21} A survey of selected representative examples is presented in Table 2.1. Among them, MnO_x has been attracted significant interest in the development of low-temperature SCR catalysts. With MnO_x-based catalysts, almost total NO conversion has been obtained already at temperatures well below 150 °C (Table 2.1, entries 1-8). The catalytic performance strongly depends on the type of MnO_x since several stable oxides such as MnO₂, Mn₅O₈, Mn₂O₃, Mn₃O₄, and MnO exists at ambient conditions. Amorphous MnO₂ with high surface area exhibited the highest activity, followed by Mn₅O₈, Mn₂O₃, Mn₃O₄, and MnO in decreasing order.⁵⁴ Although significant efforts have been given to the investigation of MnO_x for low-temperature SCR, poor resistance to SO₂ and H₂O as well as large N₂O formation are serious problems for practical applications.

To solve these problems, mixing or doping MnO_x with other metal elements, such as Ce, Zr, Ni, etc. has been studied (Table 2.1, entries 3-7). It has been found that CeO₂ can be used as both suitable support and a co-component for MnO_x to promote the deNO_x efficiency because of high redox ability of the Ce⁴⁺/Ce³⁺ redox pair and oxygen mobility within this oxide.^{15, 55} The low-temperature deNO_x performance of MnO_x-CeO₂ catalysts can be further improved by a third metal co-component such as Sn⁵⁶ and Ti.⁵⁷ Liu *et al.* showed that Mn-Ce-Ti mixed oxide catalysts enhanced the catalytic performance of Mn-Ce and Ce-Ti binary oxides, showing more than 90% NO conversion at temperatures of 150–350 °C under a GHSV of 64,000 h⁻¹ with nearly 100% N₂ selectivity.⁵⁷ Despite considerable progress that has been achieved with Mn-based catalysts for low-temperature NH₃-SCR, more research is still needed to ensure high activity together with high N₂ selectivity, better resistance against SO₂ and H₂O.

Besides MnO_x-based catalysts, the ion exchanged zeolites containing Fe, Cu, and Mn ions have been reported as promising catalysts for diesel vehicles (Table 2.1, entries 10-13).^{11, 58-59} Recent studies have shown Cu-SSZ-13 and Cu/SAPO-34 to be efficient catalysts under relevant SCR conditions.^{11, 60} However, these catalysts can quickly adsorb sulphur species, leading to a severe decrease of the SCR performance at low temperatures.^{10, 61} Furthermore, some early reports found the poor stability of SAPO-34 powders and membranes, due to hydration at low temperature which in turn led to the substantial deactivation of Cu/SAPO-34 catalysts.⁶² Therefore, a potential application of these catalysts in low-temperature NH₃-SCR will require significant improvement of hydrostability, of N₂ selectivity, and of the sulphur resistance.

Table 2.1: Maximum NO conversion and N₂ selectivity reached at respective temperatures and GHSV for selected representative low-temperature NH₃-SCR catalysts

Entry	Catalyst	X _{max} (NO)/ %	T/ °C	S(N ₂)/ %	GHSV/ h ⁻¹	Ref
1	β-MnO ₂	86	150	56	90,000	63
2	MnO _x	98	80	n. a.	47,000	64
3	MnO _x -CeO ₂	80	140	57	24,000	65
4	Mn ₄ Ce ₆ O _x	98	100	87	64,000	15
5	Mn _{0.3} Ce _{0.7} O ₂	100	110	n. a.	42,000	55
6	Mn(0.5)-ZrO _x	100	100	n.a.	30,000	66
7	Ni-Mn-O _x	100	120	≈100	38,000	67
8	Sn(0.1)-Mn(0.4)-Ce(0.5)-O	97	110	n. a.	35,000	56
9	Mn _{0.2} Ce _{0.1} Ti _{0.7} O _x	95	200	≈100	64,000	57
10	Cu/SAPO-34	85	250	99	35,000	11
11	Cu-Beta zeolite	100	175	n. a.	50,000	58
12	Fe-Mn/ZSM-5	90	125	n. a.	45,000	68
13	Fe-CuO _x /ZSM-5	98	180	n. a.	38,000	59
14	Ce _{0.5} Zr _{0.5} O ₂	35	220	n. a.	30,000	69
	MnO _x /Ce _{0.5} Zr _{0.5} O ₂	95	120	95		
15	CeO ₂	18	220	45	70,000	70
	VO _x /CeO ₂	100	220	100		
16	V ₂ O ₅ /CeO ₂	95	250	100	50,000	71
	V ₂ O ₅ /CeTiO _x	≈100	225	100		
17	Ce _{0.6} Ti _{0.4} O ₂	98	300	100	50,000	72
18	Ce _{0.16} Ti _{0.84} O ₂	100	220	95-100	50,000	73
19	Ce _{0.3} TiO _x	100	175	98	25,000	74
20	30% Nb-1% VO _x /CeO ₂	90	175	100	50,000	75
21	2.5% V ₂ O ₅ , 7% WO ₃ /TiO ₂	95	200	n. a.	14,200	76
22	2% V ₂ O ₅ , 5% WO ₃ /TiO ₂	80	200	100	40,000	77
23	3.5% V ₂ O ₅ , 10% WO ₃ /TiO ₂	100	350	n. a.	50,000	78

Among the wide variety of catalysts tested in recent years, those based on (modified) ceria belong to the most promising ones for low-temperature NH₃-SCR (Table 2.1, entries 14-20).^{12, 14, 75} This might be due to its unique ability to release and store oxygen. Cerium dioxide, CeO₂, has the fluorite crystal structure with space

group Fm3m over the temperature range from room temperature to the melting point. This structure consists of a face-centered cubic (f.c.c.) unit cell of cations (Ce^{4+}) with lattice constant $a = 5.411\text{\AA}$ anions and a cubic lattice of anions (O^{2-}) with a lattice constant $a/2$ (as shown in Figure 2.1A).⁷⁹⁻⁸⁰

When treated in a reducing environment at elevated temperature, CeO_2 forms non-stoichiometric $\text{Ce}^{4+}_{1-2y}\text{Ce}^{3+}_{2y}\text{O}_{2-y}\square_y$ phases ($0 < y \leq 0.5$) with oxygen vacancies (\square) that can be replenished by gas-phase oxygen. Therefore, the Ce valence state can easily shuttle between +4 and +3. To maintain electroneutrality, a high density of oxygen vacancies in ceria is related to an increase of its Ce^{3+} content.⁸⁰ With this property, ceria acts as an oxygen buffer to store oxygen under oxygen-rich environment and release oxygen under oxygen-lean environment, which is also called oxygen storage capacity (OSC). The OSC and the reducibility of ceria play a significant role in its applications in heterogeneous catalytic reactions, energy conversion, and other fields.¹⁷⁻¹⁹ This property is very critical for a Mars-van-Krevelen mechanism (postulated, too, for $\text{NH}_3\text{-SCR}$) in which the substrate is oxidized by lattice oxygen, and the resulting O vacancies are replenished by uptake of gas-phase O_2 .^{6, 81}

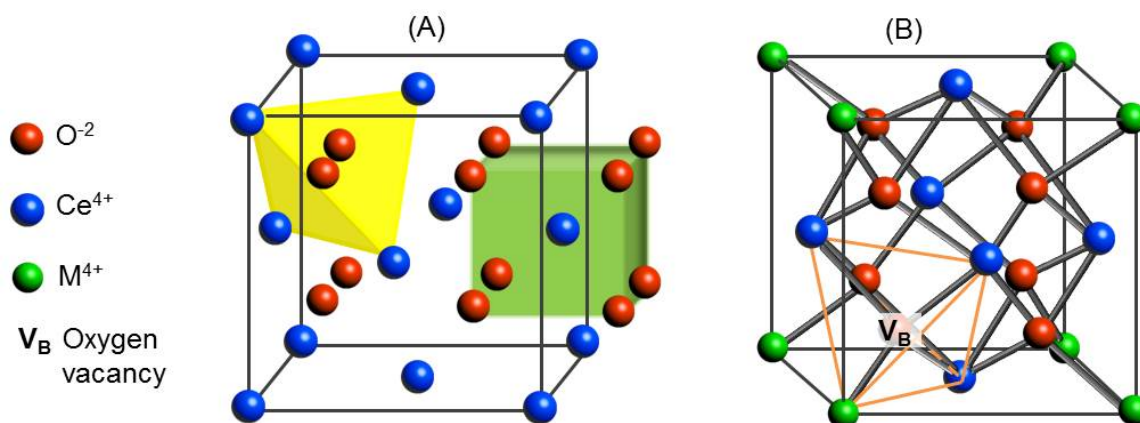


Figure 2.1: (A) The fluorite crystal structure of CeO_2 , (B) The crystal structure of modified ceria.⁸²

The high oxidation power of Ce(IV) enables pure ceria only to catalyse total oxidations. Its selectivity, however, can be tuned to a variety of selective heterogeneous catalytic redox reactions by modification with other metal ions that modify both redox and acid-base properties of ceria. Incorporation of divalent or trivalent cations into the ceria lattice creates lattice oxygen anion vacancies by a charge-compensating effect of doped cations. This increases the oxygen mobility. In other cases, incorporation of tetravalent cations like Zr^{4+} or Hf^{4+} in Ce^{4+} lattice positions strongly affects the redox properties of ceria by increasing total oxygen capacity and the oxygen mobility.^{17, 83} Compared to pure CeO_2 , Ce^{4+} in solid solutions $\text{Ce}_{1-x}\text{M}_x\text{O}_{2-\delta}$ ($\text{M} = \text{Zr}, \text{Ti}, \text{Hf}$) is easier reduced.^{80, 84-87} This reduction

creates Ce^{3+} , which in turn results in the formation of oxygen vacancies (Figure 2.1B, V_B) and improves the OSC of these mixed oxides.^{79, 85, 88} This could lead to a higher activity of ceria-containing mixed oxide supports compared to pure ceria (compare entries 15-20 in Table 2.1).^{21, 89-91} An additional enhancement of catalytic activity could frequently be obtained by depositing a small amount of highly dispersed vanadia on such supports (entry 15, 16, and 20). Such materials showed even higher performances than commercial $\text{V}_2\text{O}_5/\text{WO}_3/\text{TiO}_2$ catalysts (compare with entries 21-23 in Table 2.1).

Therefore, in this work, catalysts containing vanadium supported on modified ceria have been investigated for low-temperature NH_3 -SCR. The reason to use modified ceria support is that co-components such as Zr, Ti, Mn are expected to tune acid and redox properties, surface area, oxygen mobility, and also thermal and chemical stability. As a consequence, modified ceria might: (1) increase the dispersion of VO_x surface species and prevent the formation of V_2O_5 crystalline species, (2) improve the acidity of supported vanadia catalysts, and (3) enhance the redox behaviour of vanadium species, leading to better catalytic performance for this reaction.

2.4. Structure-Reactivity relationships of supported vanadia catalysts for NH_3 -SCR of NO_x

Owing to the development of *in-situ* and *operando* spectroscopy techniques, the structure and properties of active surface sites, the interactions between catalyst surface and the reactants as well as the different coexisting adsorbed species can be distinguished. This allows tracking the catalyst action under real catalytic conditions. It has been shown that the structure and properties of supported VO_x species are governed by the chemical identity and the surface area of the chosen supports. The catalytic behaviour of supported vanadia catalysts in NH_3 -SCR is mainly controlled by three important factors: the structure of the VO_x surface species, the acid-base properties of the catalysts and supports, and the redox properties of VO_x surface sites and supports.

2.4.1. Structure of VO_x species

The structure of surface vanadia species on different metal oxide supports, such as alumina, titania, ceria, silica, and zirconia has been investigated with many different spectroscopic methods: *in-situ*-Raman,⁹²⁻⁹⁴ FTIR,⁹⁵ UV-Vis-DRS, EPR, solid nuclear magnetic resonance (NMR), XANES/EXAFS,⁹⁶ or by a combination of scanning tunnelling microscopy (STM), infrared reflection absorption spectroscopy (IRAS), and photoelectron spectroscopy (PES).⁹⁶⁻⁹⁷ These studies showed that depending on the vanadia loading, four kinds of VO_x surface species exist on the supports (Figure 2.2). At low vanadium coverage, highly dispersed isolated VO_4 species

(monovanadate) are formed. Increasing vanadium loading leads to an increase in VO_x surface density and a conversion of isolated species to dimeric and polymeric VO_4 species (polyvanadates) until monolayer surface coverage is reached. At high vanadium loading, nanoparticles of crystalline V_2O_5 can be formed.⁹⁸

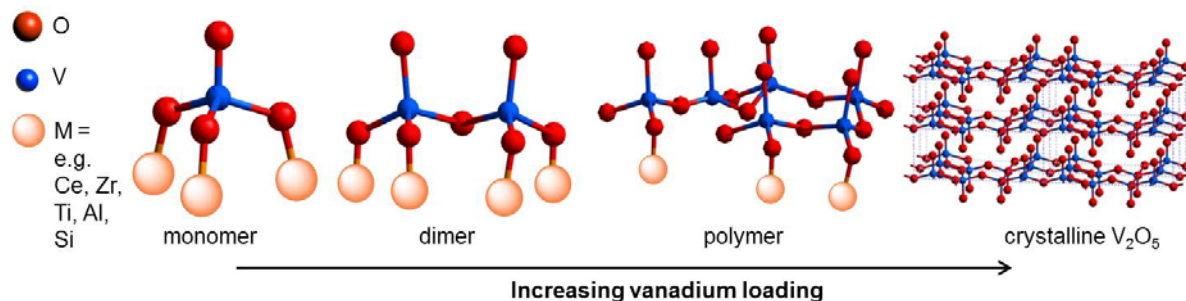


Figure 2.2: Possible structures of the VO_x species reported for supported vanadia catalysts depending on the vanadium loading.⁹⁸

Many investigations of supported vanadia catalysts for NH_3 -SCR comprise as TiO_2 support. With this regard, both isolated VO_4 species (at low V loading) and polyvanadate species (at high V loading) were found at the surface of sub-monolayer VO_x/TiO_2 catalysts.^{23, 99-102} The activity of the catalysts is increased with an increase in the V loading or an addition of WO_3 or MoO_3 . That means polyvanadate species are more active than isolated VO_4 species. However, polyvanadates accelerate the transformation of anatase to rutile phase, leading to the anatase sintering and loss of surface area of TiO_2 .^{6, 103} Whereas, WO_3 ¹⁰³ or MoO_3 ¹⁰⁴ can hinder both loss of anatase surface area and anatase to rutile transformation.

Previously, the structure and reactivity of vanadia supported on ceria have been mostly studied for oxidative hydrogenation (ODH). In particular, using a combination of high-resolution STM, IRAS, and PES, Baron *et al.*¹⁰⁵ demonstrated the formation of monomeric $\text{O}=\text{V}^{5+}\text{O}$ species on the CeO_2 (111) surface at low V loading. In this case, the reducibility of ceria stabilises the vanadium +5 oxidation state of vanadia species such as monovanadates and divanadates or trivanadates. Such stabilisation probably plays a significant role in the activity improvement of ODH reactions over ceria-supported vanadia.¹⁰⁵⁻¹⁰⁶ In line with this opinion, an explanation has been given by Abbott *et al.*⁹⁷ in a study of $\text{V}_2\text{O}_5/\text{CeO}_2$ catalysts for the ODH of methanol at low temperature. They found that catalytic activity is related to the monomeric $\text{V}=\text{O}$ species which is surrounded by a reduced ceria surface. The presence of oxygen defects on low index facets of ceria has been reported to improve the interaction of VO_x species with the defect sites and labile surface oxygen. Therefore, both the surface VO_x species and the ceria were reduced by H_2 at 400 °C while the reoxidation of reduced VO_x species occurred via ceria lattice

oxygen instead of the gas phase oxygen.⁹⁴⁻⁹⁵ On the other hand, using *in-situ* multiwavelength Raman spectroscopy, IR, isotopic labelling and TPR, Wu *et al.*^{94, 107} found that CeVO₄ can coexist with other vanadia species from monomers to polymers on the ceria surface. In this regard, the more dispersed the polyvanadates, the easier the reduction of ceria-supported vanadia sample in flowing 4% H₂/Ar is. This reduction results in the partial formation of an inactive phase CeVO₄, which cannot be reversibly reoxidized back to dispersed VO_x species under 5% O₂/He flow. The inactive phase CeVO₄ was also exhibited on VO_x/CeO₂ catalysts under propane ODH reaction.¹⁰⁸ In contrast, CeVO₄ was suggested by Martinez-Huerta *et al.*⁹³ to be both active and selective for the ethane ODH since V₂O₅/CeO₂ and CeVO₄/CeO₂ catalysts exhibited the same behaviour on activity and selectivity for this reaction.

Surprisingly, the interest in using CeO₂ as supports for vanadia in NH₃-SCR has rarely been studied up to now. So far, the relation between the structure of VO_x species and the deNO_x activity has been reported by only one paper of Peng *et al.*¹⁴ in an investigation of VO_x/CeO₂ nanorods catalysts. By analysing the catalysts with *in-situ*-Raman and DRIFT spectroscopy, they found that polymeric VO_x could create more Lewis acid sites compared to ceria, while CeVO₄ significantly improved the Brønsted acid sites, which are both assumed to contribute to the good reactivity of this catalyst.

2.4.2. Acid-base properties of catalysts and supports

The role of the acid-base properties in the catalytic behaviour of vanadia supported catalysts in NH₃-SCR has been investigated by many authors.^{6, 14, 81, 109} It was established in these investigations that ammonia adsorbs on the surface of the catalysts to form active intermediate species such as coordinated NH₃, NH₄⁺ and/or -NH₂ via different acid sites.^{31, 33} By combined *in-situ*-FTIR and on-line activity measurements, Topsøe *et al.*²⁶ have found that active sites in VO_x/TiO₂ during NH₃-SCR include predominantly Brønsted acid sites such as V⁵⁺-OH groups responsible for activating the adsorbed ammonia, while new reduced V⁴⁺-OH groups are essential for the regeneration of active sites. The role of Brønsted acidity in NH₃-SCR over supported vanadia catalysts has also been studied by other research groups.¹¹⁰⁻¹¹³ In contrast, Ramis *et al.*²² demonstrated that Lewis acid sites mainly contribute to the activation of ammonia, and Brønsted acid sites are not necessary for NH₃-SCR activity. This is in line with the observation of Hu *et al.* who applied ¹⁵N-NMR to investigate V₂O₅-TiO₂ catalysts. Furthermore, the participation of both Lewis and Brønsted acid sites has been suggested by Busca *et al.*¹¹⁴ In this case, the use of different spectroscopic methods such as IR, Raman, and UV-Vis-DRS allowed to detect V⁵⁺=O species as Lewis acid sites and V-OH species as Brønsted acid sites.

The acidity of supported vanadia catalysts also strongly depends on the supports. The pure TiO_2 support only shows Lewis acidity. The addition of WO_3 or MoO_3 to TiO_2 increases the acidity of this support since, besides Lewis acid sites of titania, additional Brønsted acid sites of W-OH or Mo-OH are present.¹⁰¹ This can improve the acidity of supported vanadia catalysts resulting in better catalytic performance. Moreover, the acidity of the TiO_2 support can be enhanced by a sulfation process, in which strong Brønsted acidity is formed while the strength of the Lewis sites is also increased.^{27, 115} Therefore, the SCR activity of $\text{V}_2\text{O}_5/\text{sulfated TiO}_2$ catalysts is higher than that of $\text{V}_2\text{O}_5/\text{TiO}_2$.

Similar to TiO_2 , pure CeO_2 has only Lewis acid sites. However, compared to TiO_2 , the Lewis acid strength of cerium ions is weaker. Moreover, the strength of these acid sites depends on the valence state of Ce. Since the polarising power (charge/radius) of Ce^{3+} (radius 1.14 Å) is lower than that of Ce^{4+} (radius 0.97 Å), the Lewis acid strength of the former is weaker.¹¹⁶ Therefore, the acidity of CeO_2 decreases upon a reduction treatment. Fortunately, the acid-base properties of ceria can be improved by its modification with other dopants (ZrO_2 , La_2O_3 , MnO_x , V_2O_5 , ZnO).¹⁹

2.4.3. Redox properties of VO_x surface sites and supports

The reducibility of vanadium oxide is considered as one of the main factors influencing its activity in $\text{NH}_3\text{-SCR}$.^{101, 111, 117-118} The catalytic redox cycle between oxidised $\text{V}^{5+}=\text{O}$ sites and reduced $\text{V}^{4+}\text{-OH}$ sites has been first proposed by Topsøe *et al.*³³ using *in-situ*-FTIR. In line with this study, an increase in the reactivity of $\text{V}_2\text{O}_5/\text{TiO}_2$ after adding WO_3 into TiO_2 for $\text{NH}_3\text{-SCR}$ in the low-temperature region was also explained by the superior redox properties of $\text{V}_2\text{O}_5\text{-WO}_3/\text{TiO}_2$ catalysts.^{101, 117} Further investigations were found in $\text{V}_2\text{O}_5/\text{WO}_3/\text{TiO}_2$ using $\text{NO}+\text{NH}_3$ TPR,¹¹⁸ transient response methods (TRM),¹¹⁹ and density functional theory (DFT) calculations.²³

It has been reported that the catalyst reducibility is closely related to the structure of VO_x surface species on a given support. In this respect, the reducibility of the surface VO_x species increases with surface VO_x coverage. Thus, the reducibility of the different supported vanadia species decreases in the order: polymeric surface $\text{VO}_x > \text{isolated surface VO}_x > \text{crystalline V}_2\text{O}_5 \text{ nanoparticles}$.^{94, 107} Moreover, the gain of the reducibility of supported vanadia catalysts is affected by the type of support used.

Comparative studies on several vanadia catalysts supported on different supports for ODH of alcohols clearly indicated that reducible supports (TiO_2 , CeO_2 , ZrO_2) are more active than non-reducible ones such as SiO_2 and Al_2O_3 .¹²⁰ This variation of

vanadia reducibility might be related to the reducibility of the different V-O-Support bonds existing on various types of support used.

In the case of ceria supports, it is unclear whether a $\text{Ce}^{4+}/\text{Ce}^{3+}$ or a $\text{V}^{5+}/\text{V}^{4+}$ redox cycle or both contribute to the overall catalytic activity.⁹⁴⁻⁹⁵ Some authors even postulated the participation of significant amounts of V^{3+} .^{31, 93, 121} A serious problem and probably a primary reason for these discrepancies is that almost all of the conclusions on structure-reactivity relationships in different reactions over ceria-supported VO_x catalysts are based on a comparison of catalytic data with the results of *ex-situ* catalyst characterization, which may not reflect the state of the working catalyst, or with only a single *in-situ* technique that cannot give comprehensive information on the structure and behaviour of different active sites. This calls for an in-depth analysis of the redox behaviour of supported VO_x /ceria catalysts under related reaction conditions by a combination of different *in-situ* and *operando* spectroscopies.

2.5. Mechanisms of NH_3 -SCR of NO_x at low temperature over supported vanadia catalysts

As far as the mechanism of NH_3 -SCR over vanadia-containing catalysts is concerned, it has been suggested that acidic sites be necessary for facilitating ammonia adsorption. However, the question remains if Lewis acid sites, or Brønsted acid sites, or both of them are responsible for this process. The role of Lewis acid sites was proposed by Ramis *et al.*²² on $\text{V}_2\text{O}_5/\text{TiO}_2$ and $\text{V}_2\text{O}_5\text{-WO}_3/\text{TiO}_2$. In this regard, a SCR mechanism based on an Eley-Rideal (E-R) mechanism has been proposed, in which ammonia is first adsorbed on the surface of the catalysts to form coordinated NH_3 and protonated NH_4^+ species, which then react with gaseous NO to form N_2 and H_2O . Moreover, the FTIR bands at 1200 cm^{-1} corresponding to coordinated ammonia disappeared faster than those of NH_4^+ (ca. 1450 cm^{-1}) during heating in the presence of NO, indicating that NH_3 species adsorbed at Lewis acid sites are thermally more stable than that at Brønsted acid sites. A combined *in-situ*-FTIR-MS study of the co-adsorption of NH_3 and NO has been carried out by Topsøe *et al.*³³ In agreement with an E-R mechanism, these authors, however, recommended that ammonia adsorbed on the Brønsted acid sites associated with $\text{V}^{5+}\text{-OH}$ species is predominantly involved in the SCR reaction. Moreover, besides the participation of acid sites, a surface redox cycle between $\text{V}^{5+}=\text{O}$ and $\text{V}^{4+}\text{-OH}$ sites was found to be essential for catalytic behaviour. For this reason, an overall reaction mechanism involving two separate catalytic functions of acid and redox properties has been proposed.^{6, 33} According to results of temperature programmed surface reaction (TPSR) and temperature programmed desorption/reaction (TPD/TPR) techniques, the catalyst redox properties are key

factors in controlling reactivity of V_2O_5/TiO_2 catalysts, which is enhanced by increasing the V and/or W loading.^{81, 101, 122}

Nevertheless, a different SCR mechanism was proposed by Liu *et al.* for $V_2O_5-CeO_2/TiO_2$ catalysts, in which both adsorbed NO_2 and monodenate nitrate were found to react with adsorbed NH_3 following a Langmuir-Hinshelwood (L-H) mechanism.²⁹ Besides, a dual pathway including E-R and L-H mechanisms was also suggested based on TPD and *in-situ*-DRIFTS.^{28, 123} In this case, during NH_3 -SCR over V_2O_5 supported on carbon nanotubes or activated semi-coke, NH_3 and NO were adsorbed on Lewis acid sites provided by V_2O_5 and oxygen functional groups of the support after nitric acid modification, respectively. Then the coordinated NH_3 reacted with gaseous NO following the E-R mechanism, while an L-H mechanism was responsible for the reaction between the adsorbed NO_2 and adsorbed NH_3 . The latter plays an important role in the improvement of low-temperature de NO_x performance over this catalyst due to the oxidation property of activated semi-coke.²⁸

Numerous investigations on the mechanism of NH_3 -SCR were performed on supported VO_x/TiO_2 catalysts, while such studies on catalysts containing ceria or modified ceria supports are widely missing. Up to now, only one study of Peng *et al.*¹⁴ has discussed reaction mechanisms over VO_x/CeO_2 nanorod catalysts during NH_3 -SCR. Two different mechanisms depending on temperature have been proposed based on *in-situ*-DRIFTS and *operando* Raman results. At low temperature (150 °C), both Lewis (from CeO_2 and polymeric VO_x) and Brønsted ($CeVO_4$) acid sites were involved. Adsorbed NO_2 and $cis-N_2O_2^{2-}$ formed during purging in $NO+O_2$ flow, reacted with adsorbed NH_3 . However, at high temperature (250-350 °C), a part of the Lewis acid sites was converted to Brønsted acid sites. Instead of adsorbed NO_2 and $cis-N_2O_2^{2-}$, surface nitrite or nitrate species were postulated as being involved in the reaction with adsorbed NH_3 . Since the complicated mechanism of NH_3 -SCR over vanadia-containing catalysts depends on a variety of factors, for example, on the type of active VO_x and acid sites, on the kind of the support and the reaction conditions, further investigations are still needed to get the better understanding of these materials for NH_3 -SCR.

3. Experimental section

Since this thesis aims at modifying CeO₂ support for supported V₂O₅ catalysts available to reduce NO_x emissions, different elements including Zr, Ti, and Mn are chosen as the modifier to enhance the texture properties and the reductive behaviour of this support.

In this chapter, at first, preparation procedures of all supports and catalysts are described. Afterwards, NH₃-SCR activity tests are described, including calculation of NO and NH₃ conversion and N₂ selectivity. In the subsequent section, the purposes and basic concepts of all characterization technique followed by their experimental descriptions are introduced. Primarily, *in-situ*-UV-Vis-DRS, *in-situ*-DRIFTS, and *operando* EPR spectroscopies are described as an in-depth analysis of the behaviour of supported V₂O₅ catalysts under relevant reaction condition.

3.1. Catalyst preparations

3.1.1. Synthesis of Ce_{1-x}Zr_xO₂ supports

To study the impact of smaller isovalent cation Zr into the cubic cell of ceria (Chapter 4), Ce_{1-x}Zr_xO₂ with different $x = 0, 0.1, 0.2, 0.3, 0.5, 0.7,$ and 1 were synthesised by a citrate sol-gel method.¹²⁴⁻¹²⁵ Appropriate amounts of 0.125 M zirconium nitrate (ZrO(NO₃)₂·6H₂O, Sigma Aldrich, 99.99%) and 0.125 M cerium nitrate (Ce(NO₃)₃·6H₂O, Acros, 99,5%) solutions with the desired Ce/Zr ratio were mixed under vigorous stirring at room temperature. A suitable amount of a 10 wt.% citric acid (C₆H₈O₇·H₂O, Alfa Aesar, 99%) solution was added to this mixed solution to adjust a molar ratio of citric acid/Ce+Zr of 2.5 for the complete complexation of the metal ions. After stirring at room temperature for 1 h, the obtained solution was evaporated at 60-80 °C to form a viscous gel. Subsequently, this gel was dried at 120 °C for 2 h and then calcined in air at 550 °C for 3 h.

3.1.2. Synthesis of Ce_{1-x}Ti_xO₂ supports

Similar to the Zr⁴⁺ cation, Ti⁴⁺ is also smaller than Ce⁴⁺. However, it is more redox-active which may lead to even higher oxygen mobility and reducibility. This is the reason to prepare such mixed oxides (Chapter 5). A co-precipitation method was chosen to synthesise all Ce_{1-x}Ti_xO₂ supports ($x = 0, 0.1, 0.3, 0.5,$ and 1) because, compared with the sol-gel method, this protocol has the advantage of production of small particles with an amorphous structure and higher surface area. Suitable amounts of 0.125 M ammonium titanyl oxalate ((NH₄)₂TiO(C₂O₄)₂·H₂O, Acros, 98%) and 0.125 M cerium nitrate (Ce(NO₃)₃·6H₂O, Acros, 99,5%) solutions were added

dropwise to an aqueous solution of the ammonia (28% NH_3 in H_2O , Sigma Aldrich, > 99.99%) under vigorous stirring at room temperature to adjust the desired Ce/Ti ratio. During this time, the pH was kept at about 10. After stirring at room temperature for 1 h, the obtained solution was aged at 60 °C for 6 h, filtered and the precipitate was washed with deionized water. The obtained solid was dried first at room temperature, then at 100 °C for 12 h and subsequently calcined in air at 550 °C for 5 h.

3.1.3. Synthesis of $\text{Ce}_{0.5}\text{Ti}_{0.5-x}\text{Mn}_x\text{O}_8$ supports

To improve the effect of supports on the catalytic behaviour of supported V_2O_5 catalysts at even lower temperatures (around 150 °C), Mn is added into the best mixed-oxide of ceria with titania (Chapter 6). Hydrothermal synthesis combined with co-precipitation method in the presence of a surfactant was used to prepare these supports. For preparation, ammonium titanyl oxalate $((\text{NH}_4)_2\text{TiO}(\text{C}_2\text{O}_4)_2 \cdot \text{H}_2\text{O})$, Acros, 98%), cerium nitrate $(\text{Ce}(\text{NO}_3)_3 \cdot 6\text{H}_2\text{O})$, Acros, 99.5%) and manganese nitrate $(\text{Mn}(\text{NO}_3)_2 \cdot 4\text{H}_2\text{O})$ were chosen as the sources of titanium, cerium, and manganese, respectively, and hexadecyltrimethylammonium bromide (CTAB, Signal Aldrich, $\geq 98\%$) was used as surfactant. Appropriate amounts of $\text{Mn}(\text{NO}_3)_2 \cdot 4\text{H}_2\text{O}$ and $\text{Ce}(\text{NO}_3)_3 \cdot 6\text{H}_2\text{O}$ were dissolved in deionized water at room temperature to get the first 0.125 M mixed solution. Meanwhile, a second solution was also prepared, in which a suitable amount of CTAB (with $(\text{Ce}+\text{Ti}+\text{Mn})/\text{CTAB}$ molar ratio is 1) was dissolved in deionized water at 30 °C, then an aqueous ammonia solution was added to this solution under vigorous stirring at room temperature. To co-precipitate, an appropriate amount of 0.125 M ammonium titanyl oxalate and the first mixed solution were added dropwise to the second solution under vigorous stirring to adjust the pH at about 9. After stirring for 1 h, the obtained suspension was transferred to a glass-sealed autoclave and aged at 120 °C for 48 h. The obtained precipitate was filtered and washed first with deionized water, then with ethanol. The resulting powder was dried first at room temperature, then at 100 °C for 12 h, and subsequently calcined in air at 550 °C for 5 h.

3.1.4. Synthesis of supported V_2O_5 catalysts

After preparing the bare supports, supported V_2O_5 catalysts were synthesised by impregnation using ammonium metavanadate (NH_4VO_3 , Sigma Aldrich, 99%) as precursor. For the first system, the $\text{V}/\text{Ce}_{1-x}\text{Zr}_x\text{O}_2$ catalysts with the content of 3, 5, and 10 wt.% V_2O_5 were prepared. After activity testing, the catalyst with 5 wt.% V_2O_5 obtained the best performance. Therefore 5 wt.% V_2O_5 was chosen for preparing all other catalyst systems in this thesis. In detail, a certain quantity of ammonium metavanadate (NH_4VO_3 , Sigma Aldrich, 99%) was dissolved in 0.2 M

oxalic acid ($C_2H_2O_4 \cdot 2H_2O$, Acros, 99.5%) solution. The required amount of the calcined support powder was suspended in this aqueous solution. After 2 h stirring at room temperature, the excess water was evaporated using a water bath, and the solid residue was oven dried at 120 °C for 12 h and subsequently calcined in air at 400 °C for 5 h.

3.2. NH_3 -SCR activity test

NH_3 -SCR activity tests were performed in a continuous-flow fixed-bed quartz reactor (length 200 mm, internal diameter 6 mm). The feed contained 1000 ppm NO, 1000 ppm NH_3 , 5 vol.% O_2 , balance He. For all experiments, 100 mg catalysts of 250-350 μm particle size and the same GHSV of 70,000 h^{-1} were used. Analysis of the product mixture was performed by on-line gas chromatography (HP 6890) using a molecular sieve 5A column for analysis of N_2 , N_2O and O_2 . Simultaneously, the product stream composition was continuously analysed by a multigas sensor (Limas 11HW, ABB, Germany), including a catalytic converter delivering NO, NO_2 , and NH_3 concentrations. Due to inlet temperature and chemical equilibrium, NO was partly converted into NO_2 before entering the reactor, and this was considered when calculating conversion and selectivity. Reactant and product contents in the effluent gas were monitored during 1 h of continuous reaction in steady state at each temperature chosen.

A long term test of catalyst $V/Ce_{0.7}Zr_{0.3}O_2$ was performed under the same conditions at 250 °C during 190 hours. Furthermore, to analyse the effect of space velocity on the catalytic behaviour, the catalysts $V/Ce_{1-x}Ti_xO_2$ were tested with the same feed composition in the range of 150 – 400 °C with higher GHSV of 300,000 and 750,000 h^{-1} . These experiments were done at the University of Bochum; more details were described elsewhere.¹²⁶

NO_x and NH_3 conversion, and N_2 selectivity were obtained by the following equations:

$$NO_x \text{ conversion (\%)} = \frac{[NO+NO_2]_{in} - [NO+NO_2+N_2O]_{out}}{[NO+NO_2]_{in}} \times 100\% \quad (3.1)$$

$$NH_3 \text{ conversion (\%)} = \frac{[NH_3]_{in} - [NH_3]_{out}}{[NH_3]_{in}} \times 100\% \quad (3.2)$$

$$N_2 \text{ selectivity (\%)} = \frac{[NO+NO_2+NH_3]_{in} - [NO+NO_2+NH_3]_{out} - 2[N_2O]_{out}}{[NO+NO_2+NH_3]_{in} - [NO+NO_2+NH_3]_{out}} \times 100\% \quad (3.3)$$

3.3. Catalyst characterization techniques

Characterization is a vital concern in any practical catalytic research and industrial activities since it provides vital parameters including chemical composition and structure, texture properties, and surface properties which are correlated with catalytic performance. In this section, the basic principle and experimental procedures of the methods used in this thesis are presented.

3.3.1. X-ray diffraction (XRD)

X-ray powder diffraction has been used to identify crystalline phases, crystallite sizes, lattice parameters and disorder in the catalysts. Diffraction effects are observed when the X-ray radiation passes through the material with the geometrical variation on the length scale of the radiation wavelength, leading to the interaction of the electron cloud of the atoms and the radiation.

Since the distances between the atoms are of similar magnitude as the wavelength of the x-rays, phenomena like constructive and destructive interference are observed when these materials are exposed to X-rays (Figure 3.1).¹²⁷ These phenomena result in diffraction where x-rays are emitted at specific angles based on the spaces between the atoms organised in crystalline structures (planes).

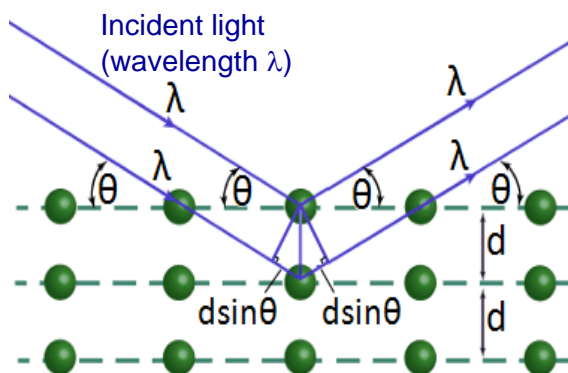


Figure 3.1: Visualisation of Bragg diffraction.

Most crystals can have many sets of planes passed through their atoms. Each plane has a particular interplanar distance and will give rise to a characteristic angle of diffracted x-rays. The relationship between wavelength, atomic spacing and diffraction is known as the Bragg equation, in which n is an integer (reflection order), λ is the wavelength of the incident X-ray beam, d is the distance between parallel lattice planes, and θ is the angle of diffraction (E.q. 3.4).

$$n \cdot \lambda = 2d \cdot \sin \theta \quad (3.4)$$

The interplanar distance can be calculated from the Bragg equation when the wavelength is known (based on the type of X-ray tube applied and if using monochromator) and the angle can be measured (with a diffractometer). With a single compound, a set of 'd-spaces' is obtained, which can be used for comparison with sets of d-spaces obtained from standard compounds and/or from a database.

Moreover, without considering the strain, the mean crystallite size is determined from the width of the diffraction lines using Scherrer's formula (Eq. 3.5)¹²⁸⁻¹²⁹

$$D = \frac{k \cdot \lambda}{\beta \cdot \cos \theta} \quad (3.5)$$

in which D , λ , β , and θ are the average crystalline diameter, X-ray wavelength, full width at half maximum, and diffraction angle respectively; k is a constant.

Furthermore, the crystallite size and lattice strain can be derived together by the Williamson-Hull equation (Eq. 3.6)¹²⁸

$$\beta_{hkl} = \frac{k \cdot \lambda}{D \cdot \cos \theta} + 4\varepsilon \cdot \tan \theta \quad (3.6)$$

in which β_{hkl} is the integral width of a reflection after removal of the instrumental broadening from the observed line profile, k is the shape factor (~ 1.0), λ is the X-ray wavelength, D is the crystallite size and ε is the strain parameter.

Experimental description: XRD powder patterns were recorded at room temperature using a theta/theta diffractometer (X'Pert Pro, Panalytical, Almelo, Netherlands) with Cu $K\alpha$ radiation ($\lambda = 1.5418 \text{ \AA}$, 40 kV, 40 mA) and a X'Celerator RTMS Detector. The data were collected in the 2 Theta range from 5 – 80°. The phase composition of the samples was determined using the program suite WinXPOW by STOE&CIE with an inclusion of the Powder Diffraction File PDF2 of the ICDD (International Centre of Diffraction Data).

3.3.2. Low-temperature N₂ adsorption

It is already realised in heterogeneous catalysis that better comprehension of catalytic behaviour requires the knowledge of the surface area and pore properties. Hence, the surface area, the specific pore volume, and the distribution of the pore size are of extraordinary importance, which makes the method for their determination very attracting. Nitrogen adsorption at its boiling temperature (77 K) represents the most widely used technique for this purpose. Based on the Langmuir theory of monolayer physisorption, the BET theory derived by Brunnauer, Emmett, and Teller is extended to multilayer adsorption. Thus, additional layers can be adsorbed on top of the monolayer with heats of adsorption equivalent to the latent heat of vaporisation of the gas (ΔH_L) (Figure 3.2).¹³⁰

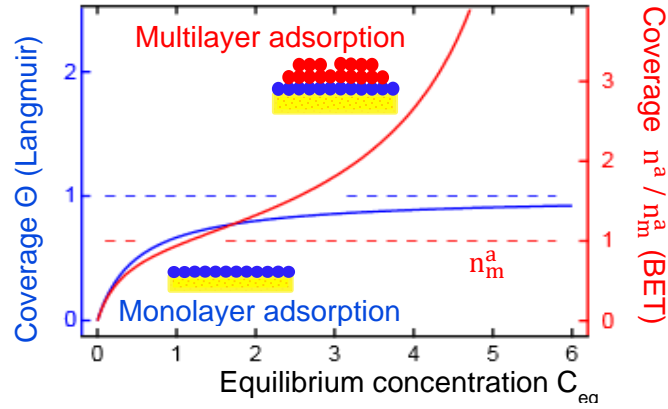


Figure 3.2: BET isotherm (red) compare to Langmuir isotherm (blue).

The resultant equation of BET adsorption isotherm in the linear form is¹³¹

$$\frac{p}{n^a \cdot (p^0 - p)} = \frac{(C - 1)}{n_m^a \cdot C} \frac{p}{p^0} + \frac{1}{n_m^a \cdot C} \quad (3.7)$$

in which n^a is the amount adsorbed gas at the relative pressure p/p^0 , n_m^a is the monolayer capacity, p is the measured pressure of the gas, p^0 is the saturated vapour pressure of the gas at the temperature of adsorption, and C is a constant.

The constant C related to the enthalpy of adsorption in the first adsorbed layer can be used to characterise the shape of the isotherm in the BET range. Notably, the BET equation requires a linear relation between $P/(n^a(P_0 - P))$ and P/P_0 (BET plot, Figure 3.3) in the limited P/P_0 range of 0.05-0.30.

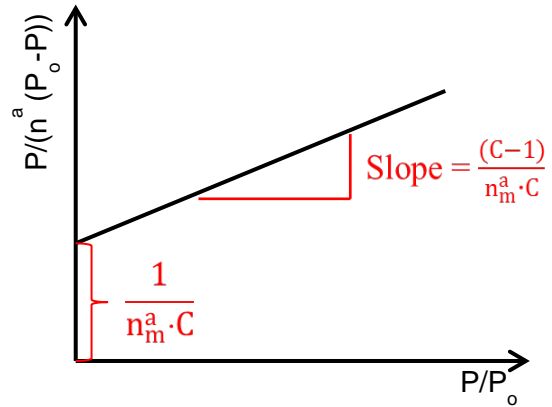


Figure 3.3: Visualization of BET.

Hence, the specific surface area (S_{BET}) can be determined from Eq. 3.8

$$S_{BET} = \frac{n_m^a \cdot L \cdot a_m}{m} \quad (3.8)$$

in which a_m is molecular cross-sectional area, m is the mass of adsorbent, and $L = 6.023 \cdot 10^{23}$ is the Avogadro constant.

Experimental description: A Micromeritics, ASAP 2010 apparatus (Micromeritics GmbH, Aachen, Germany) was used to measure the N_2 adsorption at 77 K. The samples were degassed at 200 °C in vacuum at 0.01 mbar for 3 h before the analysis. Then the specific surface areas were determined from BET plot.

3.3.3. Inductively coupled plasma optical emission spectrometry (ICP-OES)

Catalyst composition at the end of preparation can be different from that calculated according to the expected stoichiometry of the target compound. Therefore, checking the elemental composition of synthesised materials is crucial to the comparative study of catalytic activity. The weight percentages of metal ions can be quantified by ICP-OES. In this method, the sample is subjected to temperatures high enough by inductively coupled plasma source to cause significant amounts of collisional excitation. The atomic emission emitting from the plasma is displayed in either a radial or axial configuration, collected with a lens or mirror, then imaged onto the entrance slit of a wavelength selection device.¹³²

Experimental description: In a typical procedure, the sample (10 mg) was dissolved in 8 mL aqua regia and 2 mL hydrofluoric acid by treatment with the microwave-assisted sample preparation system “MULTI WAVE Pro” (Anton Paar) at ca. 200 °C and 60 bar. The solution was filled up to 100 mL with distilled water and analysed using a Varian 715-ES ICP-emission spectrometer and the ICP Expert software.

3.3.4. Temperature programmed reduction by H₂ (H₂-TPR)

As mentioned above, the redox properties play a significant role in enhancing deNO_x performance over V₂O₅-based catalysts at low temperature. The reducibility of catalysts can be characterised by H₂-TPR. Based on H₂-TPR patterns, reduction peaks of different species were obtained at temperatures needed for their total reduction. The hydrogen consumption can be used for the quantitation of the reduction capacity of active species.

Experimental description: The H₂-TPR measurement was done using a Micromeritics Autochem II 2920 instrument. A 30-200 mg sample was loaded in a U-shaped quartz reactor and heated from room temperature to 400 °C with 20 K/min in 5% O₂/He (30 ml/min) for 30 min at 400 °C, then cooled down to room temperature and flushing the sample with Ar. TPR run was carried out from room temperature to 800 °C in a 5% H₂/Ar flow (50 ml/min) with a heating rate of 10 K/min. The hydrogen consumption peaks were recorded with temperature using a TCD detector. The amount of hydrogen consumed was calculated based on the peak areas.

3.3.5. X-ray photoelectron spectroscopy (XPS)

X-ray photoelectron spectroscopy (XPS) is used to determine the oxidation state of active sites V as well as the chemical interaction between the active phase and the

oxide supports. XPS, also known as ESCA (electron spectroscopy for chemical analysis) is based on Einstein's photoelectric effect which implies that irradiation of a material with high energy photons (e.g. monoenergetic soft X-rays) gives rise to the emission of electrons (photoelectrons).¹³³ Mg K α (1253.6 eV) or Al K α (1486.6 eV) X-rays are often used. The kinetic energy (E_k) of these emitted electrons from the top 1-10 nm of the material, which is characteristic of the element from which the photoelectron originated, is quantified in the experiment. The binding energy (E_b) of the electron in a particular level is related to E_k by Einstein's law (Eq. 3.9)¹³³

$$E_k = h \cdot \nu - E_b - \phi_s \quad (3.9)$$

in which $h \cdot \nu$ is the energy of the incident radiation, ϕ_s is the spectrometer work function.

E_b increases with an increase in atomic number and oxidation state. Each element has its set of the characteristic E_b . Thus, the position and intensity of peaks in an energy spectrum enable identification and quantification of surface elements.

Experimental description: X-ray photoelectron spectra were acquired by a Thermo ESCALAB 220 iXL spectrometer (ThermoFisher Scientific) operating at room temperature with monochromatic Al K α radiation. The spectra were corrected concerning the C 1s binding energy value of 284.8 eV. Signal intensities were normalised using the sensitivity factors of Scofield and the transmission function of the spectrometer. For pseudo-*in-situ* measurements, catalysts were pretreated at 200 °C in a reaction chamber attached to the spectrometer under a flow of NH₃-SCR feed (0.4% NH₃, 0.4% NO and 10% O₂/He, total flow rate 25 ml/min) for 30 min, cooled to room temperature and subsequently transferred to the analysis chamber without intermediate contact to ambient atmosphere.

3.3.6. Electron paramagnetic resonance (EPR) spectroscopy

Electron paramagnetic resonance (EPR) spectroscopy has been extensively applied in heterogeneous catalysis to investigate the nature of species containing unpaired electrons and their environment, for examples, symmetry, number and nature of ligands, etc. The high sensitivity of the technique allows the study of low concentrations of active sites. Moreover, it also has another advantage since many highly reactive paramagnetic intermediates can be detected during the reaction by *in-situ*-EPR spectroscopy without any spectroscopic interference. Therefore, in this thesis, this powerful technique is crucial to derive the behaviour of V sites and also the coordination geometry of the paramagnetic V⁴⁺ species in the supported vanadia catalysts under real catalytic conditions. V⁴⁺ has one unpaired electron, an

electron spin of $S = \frac{1}{2}$ and a nuclear spin of $I = 7/2$. In the following, the principle of EPR is explained for V^{4+} as a particular example.

In EPR spectroscopy, the sample is placed in an external magnetic field which removes the spin degeneracy. In this external field, the electron spin of a species with $S = \frac{1}{2}$ (such as V^{4+}) is aligned more or less parallel or antiparallel to the direction z of the external field. This leads to levels of different energy (Figure 3.4) which can be derived by solving the Schrödinger equation using, in the simplest case of a free electron, the following spin Hamiltonian

$$H = g_e \beta S_z B_0 \quad (3.10)$$

in which $g_e = 2.0023$ is the g factor for the free electron, S_z is the component of the electron spin along the direction of the external magnetic field and $\mu_B = 9.274 \cdot 10^{-24} \text{ J T}^{-1}$ is the Bohr magneton. The corresponding energy of the two spin levels (Figure 3.4) is described by the Eq. 3.11

$$E = \vec{\mu}_e \bullet \vec{B} = g_e \mu_B \vec{S} \bullet \vec{B} = \pm \frac{1}{2} g_e \mu_B B_0 \quad (3.11)$$

in which \bullet describes a scalar product and μ_B is the magnetic moment of the electron. Irradiation of the sample with microwave energy excites spin transitions by absorption of electromagnetic radiation when the energetic distance between the spin levels is equal to the microwave energy. This effect is called Zeeman interaction.¹³⁴ The resonance condition is then given by Eq. 3.12

$$\Delta E = g_e \mu_B B_0 = h \cdot \nu \quad (3.12)$$

in which ΔE is the energy difference between the spin levels, B_0 is the strength of the external magnetic field and ν is the microwave frequency.

There are two methods to record EPR spectra. The first one is called the continuous wave (cw), in which the applied frequency is held constant. In this case, the magnetic field is varied until the resonance condition is fulfilled and the microwave energy matches the energy difference for the allowed spin transitions. At the same time, peak absorption of the energy occurs, and an EPR signal is measured which, for experimental reasons, appears as the first derivative of energy absorption of the radiation (Figure 3.4C).¹³⁴

The resonance energy is in the range of microwaves, for example, 9-10 GHz in X-band frequency. The second method is called pulsed EPR, in which short pulses of high power microwave are sent to the sample, and the response is recorded in the absence of radiation. In this thesis exclusively the cw method has been applied.

Since an electron is always moving in an atomic orbital, beside the intrinsic spin angular momentum, some orbital angular momentum is also present, leading to spin-orbit coupling. Spin-orbit coupling comes into play for electrons contained in orbitals with non-zero orbital angular momentum. This is, e. g., the case for V^{4+} , the single electron of which is in a d orbital. In this case the spin Hamiltonian takes the form:

$$H = \beta \cdot \vec{B} \cdot g \cdot \hat{S} + \hat{S} \cdot D \cdot \hat{S} + \hat{S} \cdot A \cdot \hat{I} \quad (3.13)$$

in which L is the orbital angular momentum vector and λ is the spin-orbit coupling constant. The g value may then deviate considerably from g_e . For a VO^{2+} vanadyl ion being the major paramagnetic species in the catalysts studied in this work, $g < g_e$.

The structure of a VO^{2+} species is usually an octahedron or a square pyramid with V in the center and oxygen atoms at the corners, one of which is bound by a short $V=O$ bond. This leads to an axial distortion. This anisotropy gives rise to an anisotropic spin distribution. In this case, the g value is no longer a scalar but a tensor with three principal components:

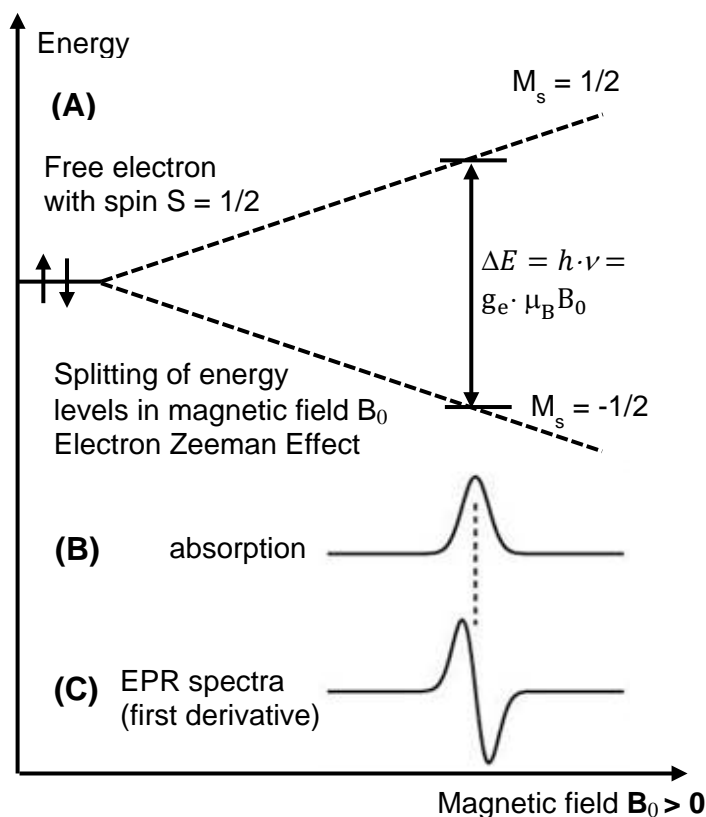


Figure 3.4: (A) Illustration of the Zeeman splitting for a $S = 1/2$ system with one unpaired electron in an external magnetic field B_0 ; (B) absorption/emission of microwave energy because of the field of resonance; (C) EPR spectrum as first derivative of the energy.

$$g = \begin{pmatrix} g_{xx} & 0 & 0 \\ 0 & g_{yy} & 0 \\ 0 & 0 & g_{zz} \end{pmatrix} \quad (3.14)$$

For VO^{2+} species in axial geometry, the g -tensor has two components, $g_{\perp} = g_{xx} = g_{yy}$ (orientation of the external magnetic field is perpendicular to the magnetic z -axis of the VO_6 octahedron) and $(g_{\parallel} = g_{zz})$ (orientation of the external magnetic field is parallel to the magnetic z -axis) (Figure 3.5).

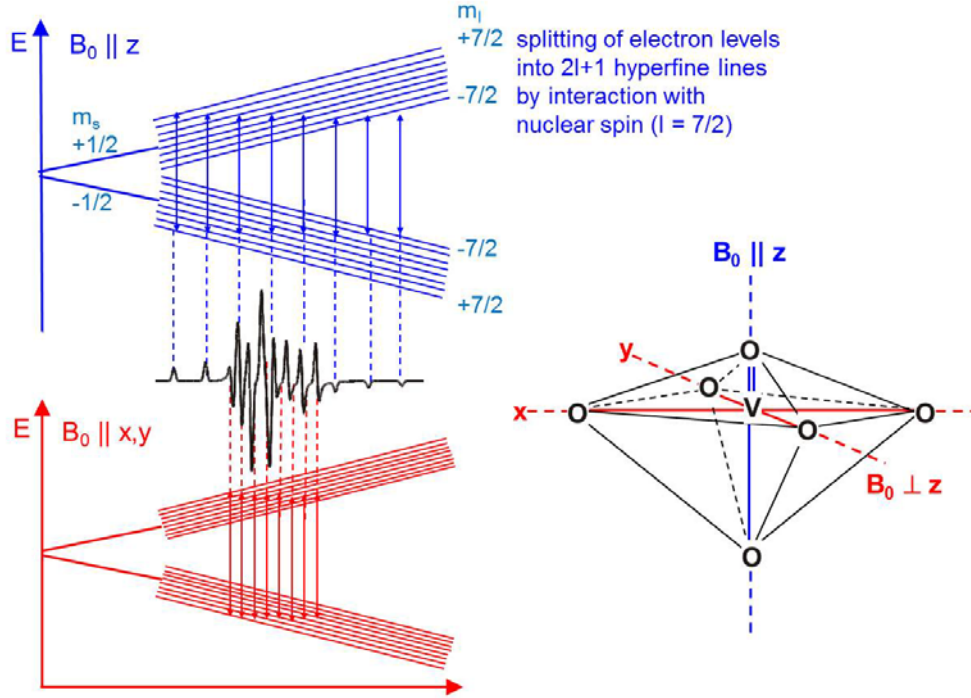


Figure 3.5: Schematic energy level splitting and the resulting EPR spectra of VO^{2+} species. Reproduced from ref. A. Brückner.¹³⁵

In a V^{4+} species, the single electron spin can couple with the nuclear spin of the ^{51}V nucleus ($I = 7/2$, 100% natural abundance). This leads to so-called hyperfine interaction which splits the two electron spin levels into $2I + 1$, namely eight, sublevels. Since the VO^{2+} site has axial geometry, this hyperfine interaction is a tensor similar to the g tensor, with principal component A_{\parallel} and A_{\perp} . Thus, each of the two g components splits into eight sublines, which superimpose in the powder spectrum of VO^{2+} as shown exemplarily in Figure 3.5 & 3.6C.

When VO^{2+} species are not isolated but connected via oxygen bridges to form clusters, anisotropic g and A splittings are averaged out and collapse into more or less isotropic signals, the line width of which depends on the strength of the dipolar interaction (Figure 3.6 A and B). These individual lines become more narrow and intense when the force of this dipolar interaction increases. Thus, crystalline $(\text{VO})_2\text{P}_2\text{O}_7$, in which the VO^{2+} sites are coupled by strong spin-spin exchange along ladder-like double chains, shows a very narrow EPR singlet (Figure 3.6A).¹

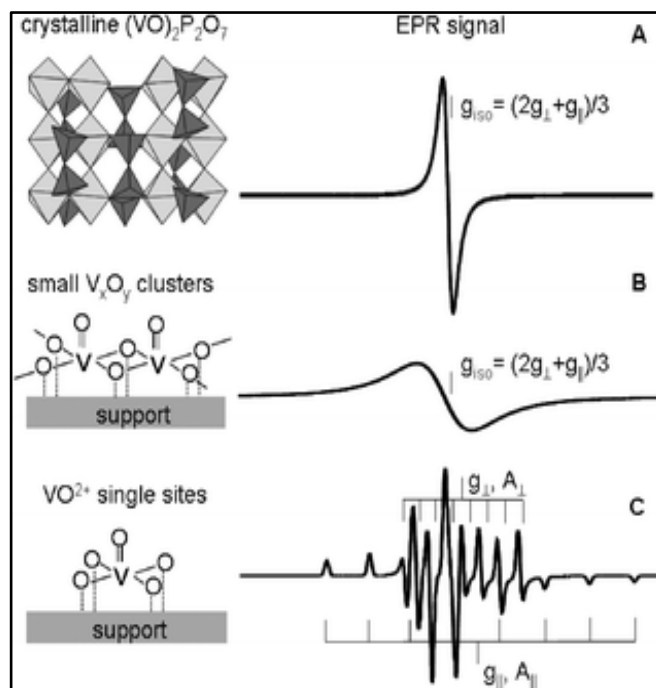


Figure 3.6: Influence of the efficiency of spin-spin exchange between neighbouring VO^{2+} sites on the shape of the EPR signal. Reproduced from ref. A. Brückner.¹

Experimental description: EPR spectra were recorded in X-band by a cw-spectrometer ELEXSYS 500-10/12 (Bruker) using a microwave power of 6.3 mW, a modulation frequency and amplitude of 100 kHz and 0.5 mT, respectively. *Operando*-EPR measurements were performed in a home-made quartz plug-flow reactor at 200 °C under the reduction of 0.2% NH_3/He flow and reoxidation of a flow of 0.2% NO , 5% O_2/He followed by the reduction of NH_3 -SCR feed (0.2% NH_3 , 0.2% NO , 5% O_2/He , total flow rate 50 ml/min). This reactor was connected to a gas-dosing device with mass flow controllers (Bronkhorst) at the inlet and a quadrupole mass spectrometer (Omnistar, Pfeiffer Vacuum GmbH) at the outlet for on-line product analysis.

3.3.7. UV-Vis diffuse reflectance spectroscopy (UV-Vis-DRS)

UV-Vis spectroscopy is suitable for the analysis VO_x sites with different types of coordination geometries and different oxidation states since intense charge-transfer transitions are observed for V^{5+} which is not accessible by EPR. In contrast to EPR, reduced V^{4+} and/or V^{3+} species cannot be characterised by UV-Vis spectroscopy in much detail, since the d-d transitions of reduced vanadium ions are usually very weak and broad. Thus, the combination of EPR and UV-Vis spectroscopy is good opportunity to widen the scope of accessible information, since both methods are to

a certain extent complementary. The UV-Vis spectroscopy is based on the excitation of electrons which is observed when the light with wavelengths in the UV or visible region (200-800 nm) passes through the sample. There are several types of the electronic transitions in organic and inorganic compounds namely $d \rightarrow d$ transitions, charge transfer, $\pi \rightarrow \pi^*$ transitions, and $n \rightarrow \pi^*$ transitions. Charge transfer occurs when an electron transfers from an occupied orbital localised on a donor to an unoccupied orbital of an acceptor.¹³⁶ These transitions in inorganic systems consist of:

- Ligand to metal (LMCT) and metal to ligand (MLTC) charge transfers
- Metal to metal charge transfers

In solid catalysts, UV-Vis spectroscopy is usually used in its diffuse reflection mode since most of the light is reflected and not transmitted. The reflected radiation from a powdered surface consists of two components: specular reflection without any interaction with the sample and diffuse reflection which penetrates into the sample and is reflected after multiple scattering at sample particles by which electron transitions are excited.

The reflectance is given by $R_\infty = I/I_0$, where I and I_0 are the intensities of the incident and reflected light, respectively. Since reflectance of the sample is compared to that of the standard compound, the relative quantity $R'_\infty = R_\infty(\text{sample})/R_\infty(\text{standard})$ is used. This reflectance is related to both the absorption coefficient (K) and the scattering coefficient (S) in the Kubelka-Munk $F(R'_\infty)$ function as follow:¹³⁷

$$F(R'_\infty) = \frac{(1 - R'_\infty)^2}{2R'_\infty} = \frac{K}{S} \quad (3.15)$$

The band gap energy can be derived from the Tauc plot as follow:¹³⁸

$$(h\nu K)^{\frac{1}{n}} \propto (h\nu F(R))^{\frac{1}{n}} = A(h\nu - E_g) \quad (3.16)$$

in which A is a proportional constant, n depends on the type of optical transitions.

CeO_2 is reported as a semiconductor with indirect band gap.¹³⁹⁻¹⁴⁰ Therefore, $n = 2$ (for indirect transitions) is used, plotting of $h\nu$ versus $[h\nu F(R)]^{\frac{1}{2}}$ forms a straight line. Hence, the value of E_g is measured by extrapolating the straight line to $F(R) = 0$.

Experimental description: UV-Vis diffuse reflectance spectra were measured using a Cary 5000 spectrometer (Varian) equipped with a diffuse reflectance accessory (praying mantis, Harrick). In normal experiments, BaSO_4 is used as reference white standard. For $\text{V/Ce}_{1-x}\text{Zr}_x\text{O}_2$ system, baselines were acquired using the bare $\text{Ce}_x\text{Zr}_{1-x}\text{O}_2$ supports to determine the structure of VO_x species only.

For *in-situ* experiments, a heatable reaction chamber (Harrick) equipped with a temperature programmer (Eurotherm) and a gas-dosing system containing mass-flow controllers (Bronkhorst) was used. For each measurement, 145 mg of catalyst particles (250-350 μm) were pretreated for 1 h at 275 $^{\circ}\text{C}$ in air, then cooled to 200 $^{\circ}\text{C}$ in He and subsequently exposed to a flow of 0.1% NH_3/He and 5% O_2/He (25 ml/min). Since the UV-Vis spectra of CeO_2 supports remained nearly stable under the NH_3 -SCR conditions, pure ceria supports were used as reference white standard instead of BaSO_4 . During this time, the absorbance at 700 nm which is in the range of d-d-transitions of reduced V-species was monitored to determine kinetic studies of reduction and reoxidation of V sites.

3.3.8. Diffuse reflectance infrared Fourier transform spectroscopy (DRIFTS)

Infrared (IR) spectroscopy is a technique based on the vibrations of the atoms of a molecule. An infrared spectrum is obtained when IR radiation passes through a sample leading to the absorption of a fraction of the incident radiation at a particular wavelength. IR radiation is divided into three main regions: the far-IR ($< 400\text{ cm}^{-1}$), the mid-IR ($4000 - 400\text{ cm}^{-1}$), and the near-IR ($13000 - 4000\text{ cm}^{-1}$). The mid-IR region is the most attractive for adsorbate studies in heterogeneous catalysts since most molecular vibrations are excited with radiation of this region. Absorption of radiation with a frequency in the mid-IR promotes the transition between molecular vibrational levels. However, only vibrations leading to a change in the electric dipole moment of the molecule can be observed in IR spectroscopy due to the selection rules. The intensity of the IR band is proportional to the change in dipole moment and is related to the quantity of the substance present in the sample. FTIR which is based on a mathematical method of Fourier-transformation (FT) to convert the raw wavelength data collected by a detector to the spectra into the computer is now predominantly used.¹⁴¹ In practical IR spectroscopy, the independent variable is usually measured as wave numbers, as opposed to wavelength.

Diffuse reflectance infrared Fourier transform spectrometry (DRIFTS) is commonly used for powder and solid samples. When these samples are penetrated with an IR beam, two types of reflectance can occur, i.e. specular and diffuse reflectance. Specular reflectance occurs when the reflected angle of radiation equals the angle of incidence and has no absorptive interaction with the sample. On the other hand, diffuse reflectance results from penetration into the sample interacting with the sample particles. Therefore, the wavelength and intensity distribution of the reflected light will contain structural information on the substrate. The DRIFTS accessory optimises the collection of the diffuse reflected light while minimising the specular component.¹⁴²

Experimental description: *In-situ*-DRIFTS was performed on a Nicolet 6700 FTIR spectrometer using a similar high-temperature reaction cell (Harrick) as for *in-situ*-

UV-Vis experiments equipped with a temperature programmer (Eurotherm) and connected to a gas-dosing device with mass flow controllers (Bronkhorst) at the inlet. However, instead of quartz windows, CaF_2 was used as a window material. 145 mg of catalyst particles (250-350 μm) were pretreated for 1 h at 300 $^\circ\text{C}$ in air and subsequently exposed at 200 $^\circ\text{C}$ to a flow of different gases (30 ml/min). Background spectra were recorded in a flow of He and subtracted from the sample spectra for each measurement at the experiment temperature. The background spectrum is obtained from pure, ground KBr.

3.3.9. Raman spectroscopy

As XRD is limited in its sensitivity towards detection of crystalline V_2O_5 species, Raman spectroscopy was used as an additional method for structure characterization. This method is based on the inelastic scattering of photons, which release energy by exciting vibrations in the sample. The scattering process occurs when monochromatic light (e.g. laser light) is radiated onto the sample. There are three kinds of frequencies that can be observed in the light detector. The Rayleigh scattering is observed when the molecule is excited to an unstable virtual state above the ground state, from which it decays back to the ground state without energy exchange. The frequencies of the incident and scattered beams are equal. This comprises the majority of reflected light and is removed by a filter to protect the detector. The second scattering is called the Stokes effect, which occurs when the excited molecule returns to the first vibrational state. In this case, the frequency of the emitted radiation is smaller than that of the incident radiation. In contrast, in the anti-Stokes process, a molecule being already in its first excited vibrational level is excited to the virtual state and emits anti-Stokes radiation upon return to its ground state.¹⁴³ In this case, the frequency of the emitted light is higher than that of the Rayleigh radiation. In most cases, the Stokes radiation is detected, due to its higher intensity. In a Raman spectrum, the frequency shift between the incident and the scattered light (corresponding to the frequency of the excited molecular vibration) is plotted in wavenumbers (cm^{-1}). Although both Raman and IR spectroscopy is vibrational methods, they differ in their selection rules. In Raman spectroscopy, a molecular vibration must result in a change in polarizability of the molecule while in IR spectroscopy the dipole moment must change.

Experimental description: Raman spectra were recorded at room temperature using a Renishaw inVia Raman microscope via 20x objective of a Leica microscope. For the measurements, a 633 nm laser with a power of 0.17 mW was used.

4. V₂O₅/Ce_{1-x}Zr_xO₂ catalysts

As mentioned in section 2.3., replacement of Ce⁴⁺ in the lattice of CeO₂ by other tetravalent ions with a smaller diameter, such as Zr⁴⁺, can strongly enhance its oxygen mobility and storage capacity. Ceria is a well-known component of three-way catalysts, and its modification by incorporation of zirconia is frequently applied to improve the stability, mechanical strength and redox properties of three-way catalysts.^{17, 85, 87, 144} However, the use of this mixed oxide as support for vanadium based catalysts in NH₃-SCR has received less attention. For the first time, V/Ce_{1-x}Zr_xO₂ catalysts have been synthesised and successfully applied for the low-temperature NH₃-SCR in this study.¹⁴⁵ Thus, in this chapter, at first, the effect of the Zr content on the deNO_x catalytic performance of these catalysts is presented (section 4.1). The following section focuses on the structural, surface, and redox properties of the bare mixed oxide supports as well as of catalysts containing supported vanadia to find the reason for catalytic performance differences (section 4.2). In the subsequent part, the behaviour of VO_x species in the presence of reactants is studied by applying different *in-situ* spectroscopy techniques (section 4.3). Conclusions are drawn in section 4.4.

4.1. Effect of Zr content on the DeNO_x catalytic performance of V/Ce_{1-x}Zr_xO₂ catalysts

The influence of the temperature on the NO and NH₃ conversion over 5% V₂O₅/Ce_{1-x}Zr_xO₂ (x=0, 0.1, 0.2, 0.3, 0.5, 0.7 and 1) catalysts for NH₃-SCR is illustrated in Figure 4.1. The content of supported vanadia was maintained at 5% in all catalysts of the study. The performance of catalysts with vanadia contents other than 5% is not included, as their activities were in all cases lower. Among all the prepared catalysts, V/CeO₂ was the least active one, reaching a maximum NO conversion of 90% at 275 °C. Even worse, the NO conversion dropped slightly at a higher temperature (300 °C). This fall is probably due to the undesired oxidation of NH₃ since the conversion of NH₃ is higher than that of NO at a higher temperature (Figure 4.1). In comparison, V/ZrO₂ was only slightly more active than V/CeO₂, yet a negligible decline in NO conversion was observed at high temperatures. In contrast, the incorporation of Zr into CeO₂ gave rise to remarkably higher catalytic performance. The activity improved markedly with only a small amount of Zr, however, then remained almost constant with a slight increase of the Zr content (compare Ce_{0.9}Zr_{0.1}O₂ and Ce_{0.7}Zr_{0.3}O₂) and decreased at higher Zr contents.

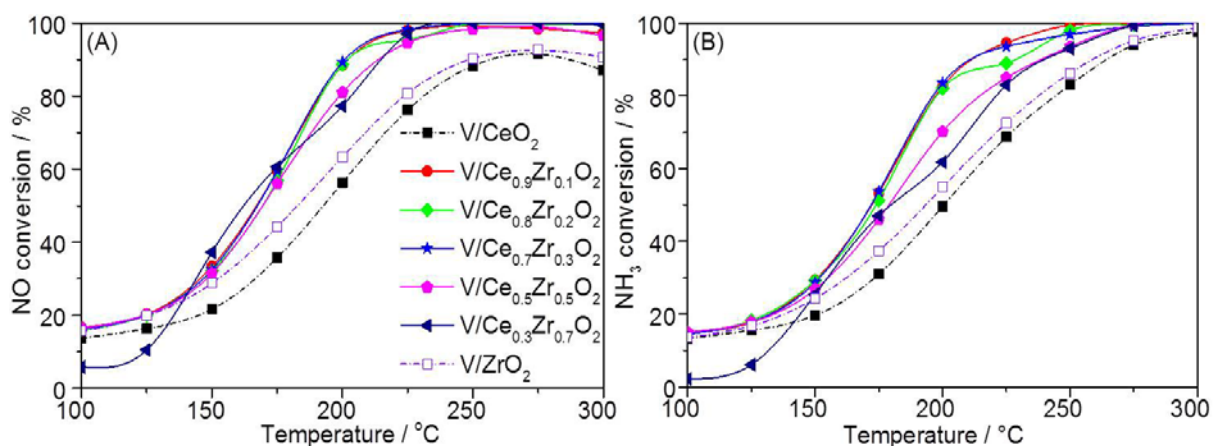


Figure 4.1: NO (A) and NH₃ (B) conversion over V/Ce_{1-x}Zr_xO₂ catalysts as a function of temperature. Feed composition: 0.1% NO, 0.1% NH₃, 5% O₂/He, GHSV = 70,000 h⁻¹.

In the case of V/CeO₂ catalysts, deactivation has been reported due to formation of crystalline CeVO₄.^{12, 108} Therefore, in order to see if this also occurs in the catalysts used in this work, a long-term catalytic test of the best catalyst V/Ce_{0.7}Zr_{0.3}O₂ lasting for 190 hours was performed at 250 °C under the same conditions as those in Figure 4.1. Fortunately, no decline of the catalytic performance has been observed during this time (Figure A.1). Moreover, no bands of CeVO₄ were detected by Raman measurements of the used V/Ce_{0.7}Zr_{0.3}O₂ catalyst (Figure A.2).

In the next parts of this chapter, the structure of the catalysts is characterised, and the results are described to gain more insight into the influence of added Zr into ceria on the catalytic performance.

4.2. Phase composition, the structural and surface properties

The XRD analysis reveals that the pristine CeO₂ support adopts cubic fluorite structure, while a mixture of monoclinic and tetragonal phases is observed for pure ZrO₂ (Figure 4.2A). Incorporation of Zr into ceria with small ratio $x = 0.1-0.3$ maintained the structure of CeO₂ without any reflections of ZrO₂. However, compared to XRD pattern of ceria, all reflections of these mixed oxides were gradually shifted to higher 2θ angles with rising Zr content, indicating a decrease in the lattice parameter due to the replacement of Ce⁴⁺ by smaller Zr⁴⁺ ions. This points to the formation of homogeneous solid solutions.^{87, 146} The XRD patterns of supported vanadium catalysts (Figure 4.2B) did not show any reflections apart from those of the corresponding supports. This result points to highly dispersed and/or amorphous vanadium oxide species on the surface of the supports. Since XRD is limited in its sensitivity towards detection of small amounts of crystalline surface VO_x species, additional characterization of these catalysts by Raman was

performed, which shows some weak bands at 145, 282, 702 and 995 cm^{-1} of V_2O_5 nanocrystallites (Figure 4.3B below). These were most pronounced for V/CeO_2 , followed by V/ZrO_2 and weakest for $\text{V}/\text{Ce}_{0.7}\text{Zr}_{0.3}\text{O}_2$.

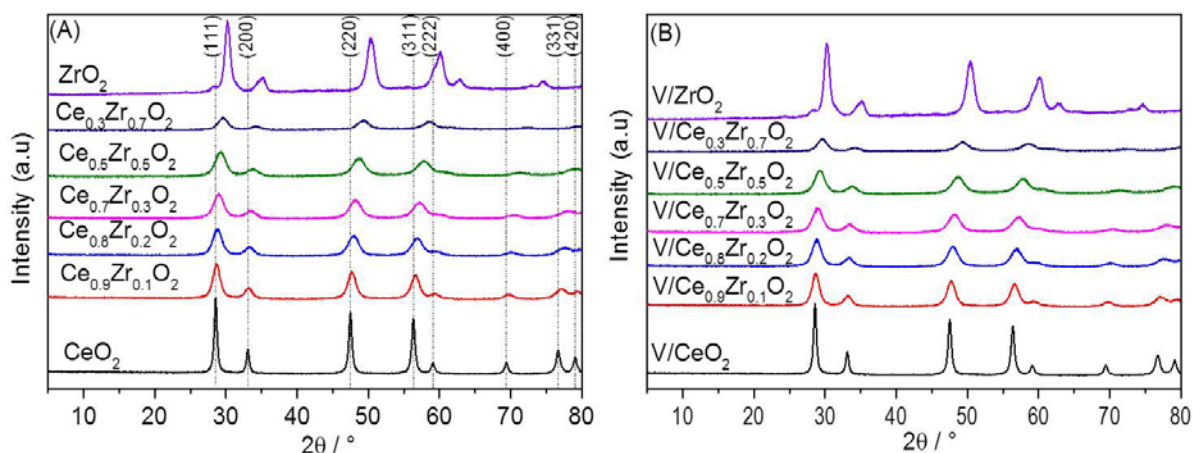


Figure 4.2: X-ray diffraction patterns of pure supports $\text{Ce}_{1-x}\text{Zr}_x\text{O}_2$ (A) and 5% $\text{V}_2\text{O}_5/\text{Ce}_{1-x}\text{Zr}_x\text{O}_2$ catalysts (B).

Incorporation of Zr into CeO_2 enhanced the BET surface area and pore volume of pure oxide reaching a maximum for the composition $\text{Ce}_{0.7}\text{Zr}_{0.3}\text{O}_2$ (Table 4.1). On the other hand, only a slight loss in the surface area of all supports was observed upon deposition of vanadium oxide, which leads to negligible pore blockage. The bulk $\text{V}/(\text{Ce}+\text{Zr})$ atomic ratios were confirmed by ICP-OES measurement (Table 4.1). All samples displayed values similar to the theoretical ones, indicating the successful preparation of vanadium based catalysts by wet impregnation method. The results above show that the incorporation of a certain amount of Zr into ceria can increase the support surface area leading to the higher dispersion of surface vanadium oxide species, which is beneficial for enhancing the catalytic performance of these catalysts as shown in section 4.1.

Applying XPS measurements, further information about the oxidation states of each component in the samples are derived. Table 4.2 presents the electron binding energies (E_B) of O 1s, Zr 3d_{5/2} and V 2p_{3/2} signals as well as atomic ratios of Ce/Zr and $\text{V}/(\text{Ce}+\text{Zr})$ determined from XPS, and Figure A.3 to A.5 illustrate the corresponding spectra. The O1s E_B value in all fresh and used catalysts were somewhat similar and between the typical values of the corresponding CeO_2 and ZrO_2 at 528.6 and 530.6 eV, respectively.^{85, 147}

The oxidation state of Zr is confirmed as IV, since the Zr 3d_{5/2} E_B values at 182-182.3 eV in fresh and used V/ZrO_2 and $\text{V}/\text{Ce}_{0.7}\text{Zr}_{0.3}\text{O}_2$ catalysts were in typical range for Zr^{4+} species,^{85, 148} while a higher E_B was observed for $\text{V}/\text{Ce}_{0.9}\text{Zr}_{0.1}\text{O}_2$ catalyst. This shift can be explained by the small amount of substitutional Zr ions in this

sample leading to the highest dispersion of Zr in the CeO₂ matrix.^{85, 147} As shown in Figure A.5, the Ce 3d spectra of all samples contain pronounced peak at 917 eV corresponding to the presence of Ce⁴⁺ state. Any peaks between 880 and 881 eV typical for Ce³⁺ were not found which excludes the presence of Ce³⁺.^{85, 144, 149-150} Unfortunately, the low signal-to-noise ratio and/or the influence of the nearby O 1s peak did not allow for determining the V valence state. Nevertheless, some trends can be deduced from the increase in the electron binding energy of the V 2p_{3/2} peak with rising Zr amount. The lowest E_B values (516.3-516.5 eV) characteristic for V⁴⁺ were observed for V/CeO₂,¹⁵¹ while the highest E_B value of 517.2 eV was found for V/ZrO₂ indicating the presence of V⁵⁺. On the other hand, the values for V on the mixed supports were in between, pointing to a mixture of tetra- and pentavalent V on these samples.

Table 4.1: Chemical composition, specific surface area and pore volume of supports and catalysts

Sample	Ce/Zr ratio ^[a]	V/(Ce+Zr) ratio ^[a]	V/(Ce+Zr) ratio ^[b]	coverage V/nm ²	S _{BET} / m ² g ⁻¹	Pore volume / cm ³ g ⁻¹
CeO ₂					12.7	0.026
Ce _{0.9} Zr _{0.1} O ₂					27.3	0.036
Ce _{0.7} Zr _{0.3} O ₂					49.0	0.038
ZrO ₂					25.7	0.032
V/CeO ₂		0.100	0.100	27.4	11.5	0.043
V/Ce _{0.9} Zr _{0.1} O ₂	8.611	0.092	0.097	9.7	31.3	0.046
V/Ce _{0.7} Zr _{0.3} O ₂	2.356	0.091	0.091	9.8	32.9	0.030
V/ZrO ₂		0.071	0.071	12.6	25.0	0.031

^[a] results from ICP, ^[b] theoretical values

Since only slight differences in the binding energies between the fresh and used samples were detected from these *ex-situ* XPS data, pseudo-*in-situ*-XPS studies were carried out at some selected samples (see section 4.3 below) to check whether this could be due to possible reoxidation in the ambient atmosphere after removing used catalysts from the reactor.

The surface V/(Ce+Zr) ratios (Table 4.2) are in all cases significantly higher than the corresponding bulk ratios obtained by ICP-OES (Table 4.1) which might be due to

the fact that the catalysts have been prepared by impregnation. However, remarkable differences are observed depending on the support. The surface V/(Ce+Zr) ratio was highest for V/CeO₂, dropping with rising Zr content in the support, approaching the lowest value for V/ZrO₂. This trend indicates that V easily inserts into the bulk of the support with increasing Zr content, which agrees with previous investigations confirming the formation of solid solutions between VO₂ and ZrO₂.¹⁵²⁻¹⁵³ This assumption is supported below by EPR, too, in which the V⁴⁺ EPR signal of V/ZrO₂ has much higher intensity compared to that of the other catalysts. The explanation is that the ion radius of V⁴⁺ (72 pm) is smaller and closer to that of Zr⁴⁺ (84 pm) compared to that of Ce⁴⁺ (97 pm),¹⁵⁴ which facilitates the substitution of V⁴⁺ for Zr⁴⁺ in bulk sites.

Table 4.2: XPS Binding Energies (eV) and Atomic Ratios of fresh and used V/Ce_{1-x}Zr_xO₂ catalysts.

Sample	Binding energy (eV)			Atomic ratio	
	O 1s	Zr 3d _{5/2}	V 2p _{3/2}	Ce/Zr	V/(Ce+Zr)
V/CeO ₂ fresh	529.2		516.5		0.78
V/CeO ₂ used	529.3		516.3		0.70
V/Ce _{0.9} Zr _{0.1} O ₂ fresh	529.2	184.6	516.4	2.66	0.49
V/Ce _{0.9} Zr _{0.1} O ₂ used	529.3	183.6	516.7	5.48	0.30
V/Ce _{0.7} Zr _{0.3} O ₂ fresh	529.7	182.2	516.8	0.68	0.41
V/Ce _{0.7} Zr _{0.3} O ₂ used	530.8	182.2	516.9	0.94	0.52
V/ZrO ₂ fresh	530.2	182.2	517.2		0.30
V/ZrO ₂ used	530.2	182.3	517.2		0.31

XPS provides insights into oxidation states and chemical environment of atoms within a few surface layers and is limited by the measurement conditions in the high vacuum environment. Therefore, EPR and UV-Vis-DRS were also used as complementary methods to provide similar information on V⁴⁺ and V⁵⁺ species but in the whole bulk of samples. It is noted that the UV-Vis-DR spectra of the bare CeO₂, ZrO₂, and mixed oxide supports have an absorbance band centred in the UV region below 350 nm, the spectra of the catalysts were recorded using the bare supports as white reference standards to obtain the coordination of only vanadium species. Thus, UV-Vis-DR spectra of the calcined catalysts in Figure 4.3A originate exclusively from vanadium.

As illustrated in Figure 4.3A, the spectra are governed by charge-transfer (CT) bands of pentavalent V species in a rather broad wavelength range extending up to

550 nm. Frequently, to distinguish different coexisting V_xO_y moieties in the broad experimental UV-Vis spectra of supported vanadia catalysts, a deconvolution of these spectra into individual superimposed sub-bands is applied. Usually, the following band assignments can be found: < 300 nm – VO_4 single sites; 300-400 nm – polymerised VO_4 species; 400-420 nm – VO_{4+x} single sites with $x=1$ or 2; ≥ 450 nm – polymerised VO_{4+x} species.¹⁵⁵⁻¹⁵⁸ However, in this case, the spectra of all three catalysts were rather similar and consisted of a variety of V_xO_y species ranging from single VO_{4+x} sites to more or less extended V_xO_y clusters. Therefore, a deconvolution would not give any useful information. Nevertheless, the spectra in Figure 4.3A are all governed by significant absorbance in the range above 400 nm, relating to the widespread presence of more or less polymerised VO_{4+x} species, whereby the extent of polymerization seems to be slightly higher for the binary mixed oxide support compared to the pure oxides. This is in good agreement with the vanadium coverage of these samples (Table 4.1), which are above the theoretical value for monolayer coverage (about 8 V/nm^2)¹⁵⁹ and increases in the order $V/Ce_{0.7}Zr_{0.3}O_2 < V/ZrO_2 \ll V/CeO_2$. The high V coverage indicates the formation of V_2O_5 nanocrystallites on the surface of these catalysts, which is supported below by Raman results (Figure 4.3B). In contrast to the Ce-containing catalysts, the spectra of the V/ZrO_2 sample show significant absorbance below 350 nm indicating the presence of VO_{4+x} sites. These species might be preferentially formed by replacement of Zr^{4+} lattice sites,^{153, 157} as supported, too, by XPS data discussed above and EPR data presented below (signal of V/ZrO_2 described below).

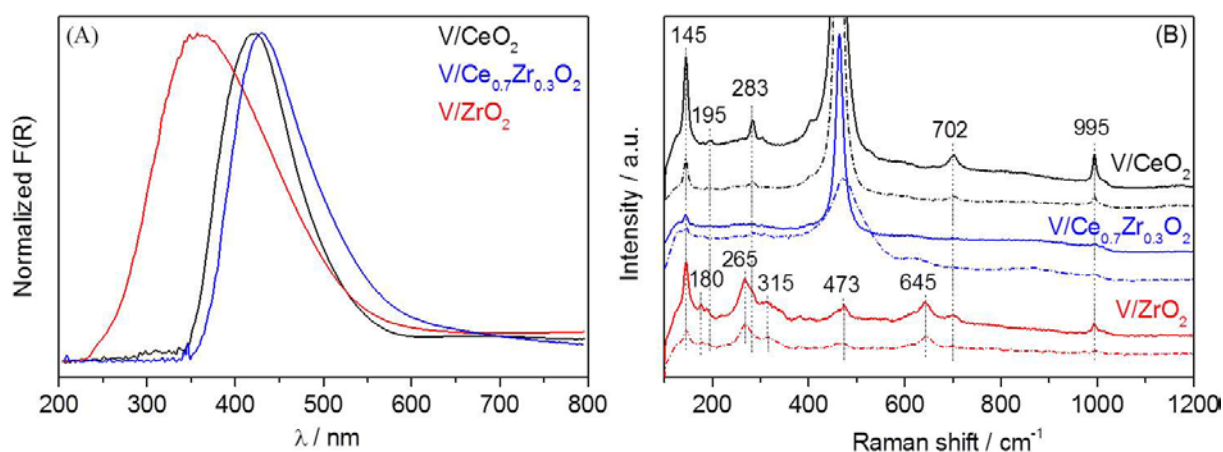


Figure 4.3: (A) *In-situ*-UV-Vis-DR spectra of the V/CeO_2 , V/ZrO_2 , and $V/Ce_{0.7}Zr_{0.3}O_2$ catalysts recorded after pretreatment in synthetic air at 275 °C and 10 min in He flow at 200 °C, with CeO_2 , ZrO_2 , and $Ce_{0.7}Zr_{0.3}O_2$ as reference white standards, respectively; (B) Raman spectra of the same samples before (solid lines) and after 18 h under NH_3 -SCR conditions (dashed lines).

Raman spectra in Figure 4.3B exhibit some small peaks at 145, 195, 283, 702 and 995 cm^{-1} characteristic for V_2O_5 nanocrystallites besides the primary F_{2g} vibration of the fluorite lattice at 463 cm^{-1} .^{144,160} The intensity of these peaks on $\text{V/Ce}_{0.7}\text{Zr}_{0.3}\text{O}_2$ is significantly lower than that on V/ZrO_2 and V/CeO_2 indicating less V_2O_5 nanocrystals on the surface of this catalyst, which is beneficial to enhancing the catalytic performance.

EPR spectra of fresh catalysts together with the V-free supports are illustrated in Figure 4.4. The spectra of supports shows weak signals arising from paramagnetic oxygen defects such as O^\bullet and/or O_2^\bullet in the range of $g = 2.0$ and minor Zr^{3+} single sites ($g_\perp = 1.965$, $g_\parallel = 1.945$).¹⁶¹⁻¹⁶³

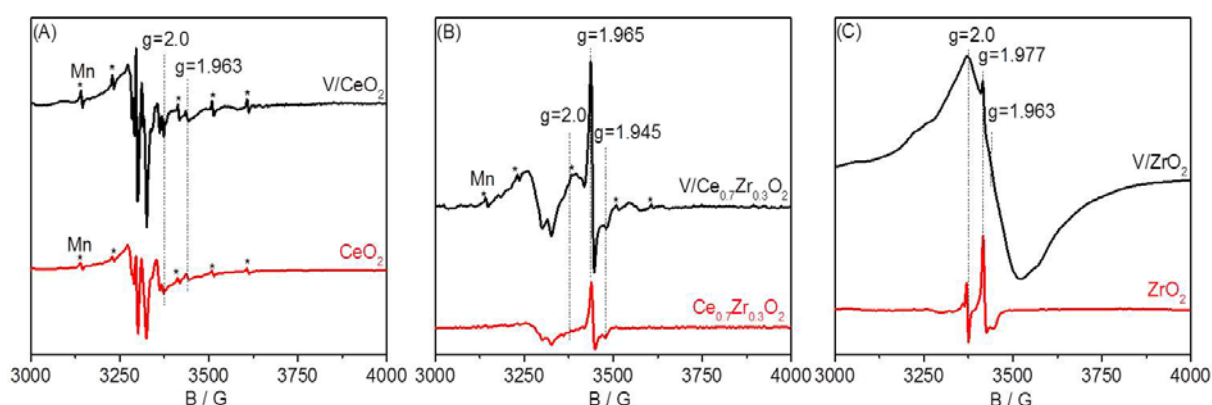


Figure 4.4: The EPR spectra of CeO_2 and V/CeO_2 (A), $\text{Ce}_{0.7}\text{Zr}_{0.3}\text{O}_2$ and $\text{V/Ce}_{0.7}\text{Zr}_{0.3}\text{O}_2$ (B) and ZrO_2 and V/ZrO_2 (C) recorded at -183°C .

Occasionally, the latter signals have been assigned to Ce^{3+} ,¹⁶⁴⁻¹⁶⁶ yet this is very unlikely since Ce^{3+} as a 4f1 ion is characterised by strong spin-orbit coupling leading to significant deviations of the g tensor components from the Landé factor ($g_e = 2.0023$). Thus, tetragonally distorted Ce^{3+} centres with $g_\parallel = 3.038$ and $g_\perp = 1.396$ and/or $g_\parallel = 0.725$ and $g_\perp = 2.402$ have been detected in crystalline solids with fluorite structure.¹⁶⁷⁻¹⁶⁸ Moreover, Ce^{3+} is detectable usually only at temperatures well below -196°C because of short relaxation time. Besides, CeO_2 contained also a Mn^{2+} impurity evidenced by the small hyperfine structure (hfs) sextet (marked with stars in Figure 4.4). The EPR spectrum of the V/ZrO_2 catalyst exhibits a broad signal of polymerised VO^{2+} species around $g = 1.963$ (Figure 4.4C). As mentioned above, this is explained by the stabilization of V^{4+} in Zr^{4+} bulk positions, which leads to a depletion of V on the surface as indicated by XPS (compare Tables 4.1 to 4.2). Surprisingly, although XPS data of catalysts V/CeO_2 and $\text{V/Ce}_{0.7}\text{Zr}_{0.3}\text{O}_2$ point to the presence of V^{4+} on the surface (Table 4.2), no significant VO^{2+} signal is seen in the EPR spectra of these catalysts (Figure 4.4A & 4.4B). Furthermore, for these two catalysts, vanadium was much more enriched on the surface compared to V/ZrO_2 . It is possibly attributed to significant differences

in the local environment between the surface VO^{2+} species and those located in deeper layers. These differences may lead to short relaxation times which would require measurement temperatures below $-183\text{ }^{\circ}\text{C}$ to detect those V^{4+} species as it is known, for example, for tetrahedral V^{4+} .¹⁶⁹⁻¹⁷⁰ On the other hand, it cannot be excluded that some surface V is reduced under the UHV conditions of the XPS measurements.

4.3. Behaviour of VO_x species in the presence of reactants

Although there is still much debate about the mechanism of the NH_3 -SCR over supported vanadia catalysts,¹⁷¹ there seems to be agreement on one important issue, namely the fact that V sites participate in reversible reduction/reoxidation cycles.¹⁷¹⁻¹⁷³ Thus, the catalyst activity should depend on the redox efficiency of the involved V sites. To further explore this behaviour and reasons for their different catalytic performance, samples V/CeO_2 , V/ZrO_2 and $\text{V/Ce}_{0.7}\text{Zr}_{0.3}\text{O}_2$ have been studied by *in-situ*-UV-Vis-DRS, *in-situ*-EPR and pseudo-*in-situ*-XPS.

In-situ-UV-Vis-DR spectra of catalyst $\text{V/Ce}_{0.7}\text{Zr}_{0.3}\text{O}_2$ at $200\text{ }^{\circ}\text{C}$ in air and after reaching a steady state in the SCR feed flow are displayed in Figure 4.5A. Switching from air to the SCR feed led to a decrease in the intensity of the CT bands of V^{5+} in the region of 400-450 nm, and an increase of UV-Vis absorbance above 550 nm characteristic for d-d transitions of reduced $\text{V}^{4+}/\text{V}^{3+}$ cations. Interestingly, this V reduction was reversible when NH_3 was removed from the feed leaving behind only NO/O_2 , indicating that an average V valence state below +5 is established under reaction conditions. A similar behaviour was also observed for V/CeO_2 and V/ZrO_2 (Figure A.6).

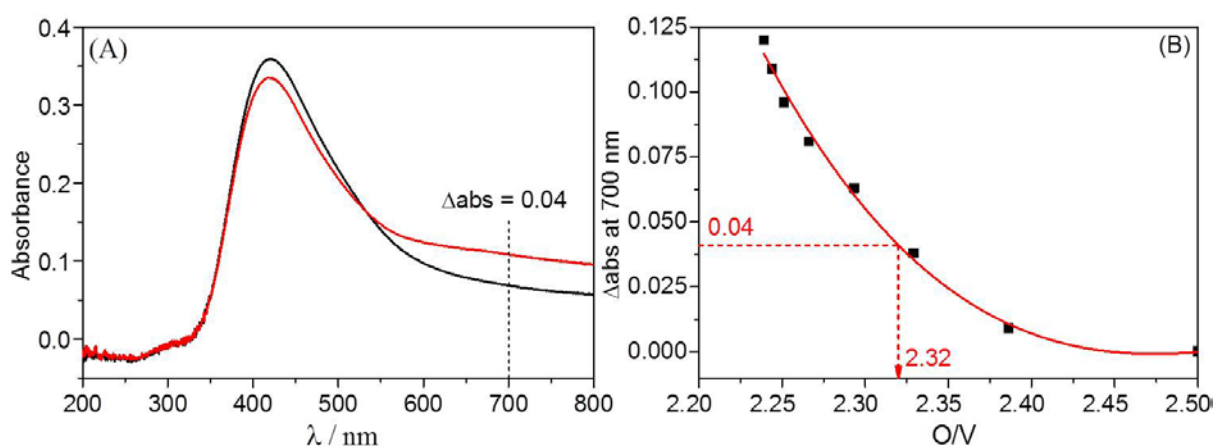


Figure 4.5: (A) *In-situ*-UV-Vis-DR spectra of $\text{V/Ce}_{0.7}\text{Zr}_{0.3}\text{O}_2$ at $200\text{ }^{\circ}\text{C}$ in air (black) and under NH_3 -SCR feed flow (red); (B) Difference of absorbance at 700 nm as a function of the O/V molar ratio derived from H_2 consumption in a simultaneous TPR/UV-Vis experiment.

The $\Delta\text{abs}(700 \text{ nm})$ values in the *in-situ*-UV-Vis-DRS experiments (Figure 4.5A) have been compared with those obtained during a H_2 -TPR experiment in which the reactor has been simultaneously coupled to a fiber optical UV-Vis spectrometer (Figure 4.5B). From these results, the average V valence state established in the catalysts under SCR conditions is derived. From the O/V ratio (Figure 4.5B, derived from the H_2 consumption), corresponding to the $\Delta\text{abs}(700 \text{ nm})$ value in the *in-situ*-UV-Vis experiment under SCR-conditions (Figure 4.5A), average V valences of +4.64, +4.62 and +4.90 were estimated for catalysts $\text{V/Ce}_{0.7}\text{Zr}_{0.3}\text{O}_2$, V/ZrO_2 , and V/CeO_2 , respectively. Although the mean V valence states under working conditions were almost equal for V/ZrO_2 and $\text{V/Ce}_{0.7}\text{Zr}_{0.3}\text{O}_2$, it must be considered that the surface V concentration on ZrO_2 was lower than on $\text{Ce}_{0.7}\text{Zr}_{0.3}\text{O}_2$ (Table 4.2). This may be one though not the main reason for its lower activity since the total amount of active $\text{V}^{5+}/\text{V}^{4+}$ redox couples is lower on V/ZrO_2 . Due to their higher redox potential, the latter species are assumed to be more active than $\text{V}^{4+}/\text{V}^{3+}$ redox couples.^{155, 174-176} However, the rather high mean V valence of +4.90 for V/CeO_2 would hardly fit with this explanation since this catalyst was the least active. This suggests that apart from the average steady state V valence and the amount of V sites that can undergo reversible redox cycles, the rate of V reduction and reoxidation may be essential for the catalytic activity.

Therefore, this property has been analysed by *in-situ*-UV-Vis-DRS, too. For this purpose, $\Delta\text{abs}(700 \text{ nm})$ in catalysts $\text{V/Ce}_{0.7}\text{Zr}_{0.3}\text{O}_2$, V/ZrO_2 and V/CeO_2 pretreated for 1 h at 275 °C in air flow has been monitored as a function of time after switching to a flow of 0.1% NH_3/He (reduction) and back to a 5% O_2/He flow (reoxidation) (Figure 4.6). Experimental data have been fitted using first-order rate laws (E.q. 4.1 and 4.2), in which C_{red} and C_{reox} denote the concentration of reduced and reoxidised V sites, C^0 values correspond to the respective concentrations of the starting V species, and k are the rate constants. It should be noted that concentrations are related to the individual $\Delta\text{abs}(700 \text{ nm})$ values, yet absolute concentration values cannot be given since this would require the knowledge of absorption coefficients. Two different V reduction and reoxidation processes, a fast and a slow one, had to be assumed to obtain satisfactory fits (Table 4.3).

$$C_{\text{red}} = C_{\text{ox1}}^0 [1 - \exp(-k_{\text{red1}} \cdot t)] + C_{\text{ox2}}^0 [1 - \exp(-k_{\text{red2}} \cdot t)] \quad (4.1)$$

$$C_{\text{reox}} = C_{\text{red1}}^0 [\exp(-k_{\text{reox1}} \cdot t)] + C_{\text{red2}}^0 [\exp(-k_{\text{reox2}} \cdot t)] \quad (4.2)$$

It is anticipated that the fast processes (reflected by $k_{\text{red}2}$ and $k_{\text{reox}2}$) are associated with V sites which are exposed on the outermost surface and readily accessible to reactants while slow processes (reflected by $k_{\text{red}1}$ and $k_{\text{reox}1}$) may reflect V sites in deeper layers beneath the surface (Table 4.3). From Table 4.3, it is readily evident

that reduction is much faster than reoxidation for all catalysts. This probably explains why a steady state mean V valence state below +5 is established in all catalysts under SCR conditions.

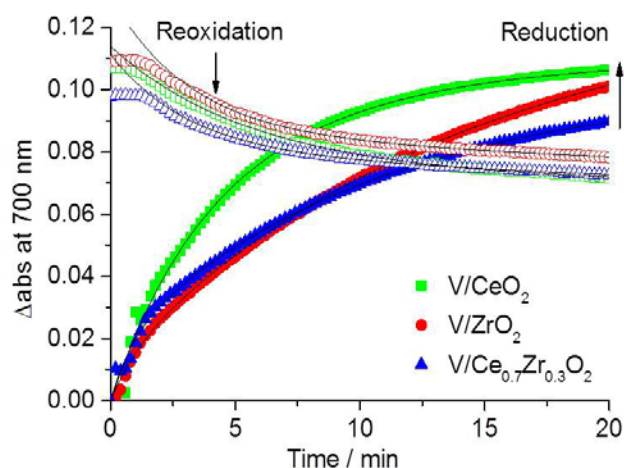


Figure 4.6: Difference of absorbance at 700 nm as a function of time for catalysts pretreated at 275 °C in air during reduction in 0,1% NH₃/He and during reoxidation in 5% O₂/He. Experimental data – coloured symbols, black solid lines – kinetic fits using first order rate laws (Eq. 4.1 and 4.2).

Table 4.3: Rate constants of V reduction and reoxidation (k/min^{-1} , E.q. 4.1 and 4.2) and mean V valence derived after 20 min under SCR feed flow at 200 °C using simultaneous TPR/UV-Vis calibration curves (see Figure 4.5, Figure 4.6 and Figure A.6).

Sample	V/CeO ₂	V/ZrO ₂	V/Ce _{0.7} Zr _{0.3} O ₂
$k_{\text{red}1}$	0.104	0.070	0.095
$k_{\text{red}2}$	0.271	0.960	1.174
$k_{\text{reox}1}$	0.003	0.004	0.005
$k_{\text{reox}2}$	0.181	0.310	0.319
$k_{\text{red}2}-k_{\text{reox}2}$	0.090	0.650	0.855
Mean V valence	4.90	4.62	4.64

However, while the reduction and reoxidation constants k_1 for the slow subsurface processes are rather similar for all three catalysts, significant differences exist for the constants k_2 reflecting the faster surface processes which might be more relevant for catalysis. The difference in reduction and reoxidation rates $k_{\text{red}2}-k_{\text{reox}2}$ is almost one order of magnitude smaller for catalyst V/CeO₂ which may account for the high steady state V valence of +4.90. Remarkably, the absolute values of both $k_{\text{red}2}$ and $k_{\text{reox}2}$ are also the smallest among all three catalysts, which points to slow surface V redox cycles. This may be another reason for the low catalytic activity.

Ex-situ XPS data did not provide any evidences for the presence of Ce^{3+} in the catalysts (*vide supra*). Therefore, the pseudo-*in-situ*-XPS experiments were performed to confirm the formation of Ce^{3+} under reaction conditions which was not detected by *ex-situ* XPS due to subsequent reoxidation in ambient atmosphere. In these experiments, catalysts $\text{V/Ce}_x\text{Zr}_{1-x}\text{O}_2$ and V/CeO_2 were pretreated at 200 °C in a flow of NH_3 -SCR feed (0.4% NO , 0.4% NH_3 , 10% O_2/He) and were then transferred to the analysis chamber without air contact.

The Ce^{4+} and Zr^{4+} signals of catalyst $\text{V/Ce}_{0.7}\text{Zr}_{0.3}\text{O}_2$ (Figure 4.7) remained unchanged, which clearly indicates that neither Ce^{4+} nor Zr^{4+} is reduced under reaction conditions. After pretreatment in air, the V $2p_{3/2}$ peak was detected at $E_B = 516.8$ eV being characteristic for a mixture of V^{5+} and V^{4+} as described above. However, a minor shift to $E_B = 516.5$ eV was observed for this peak after the reaction hinting to the formation of a slightly higher amount of V^{4+} . This agrees pretty well with *in-situ*-UV-Vis-DRS data discussed above in comparison with the presence of a hfs signal of VO^{2+} detected by *in-situ*-EPR below (Figure 4.8C). The Ce 3d spectrum of sample V/CeO_2 remained, apart from a slight peak narrowing, also almost unchanged, which clearly indicates the presence of only tetravalent Ce.

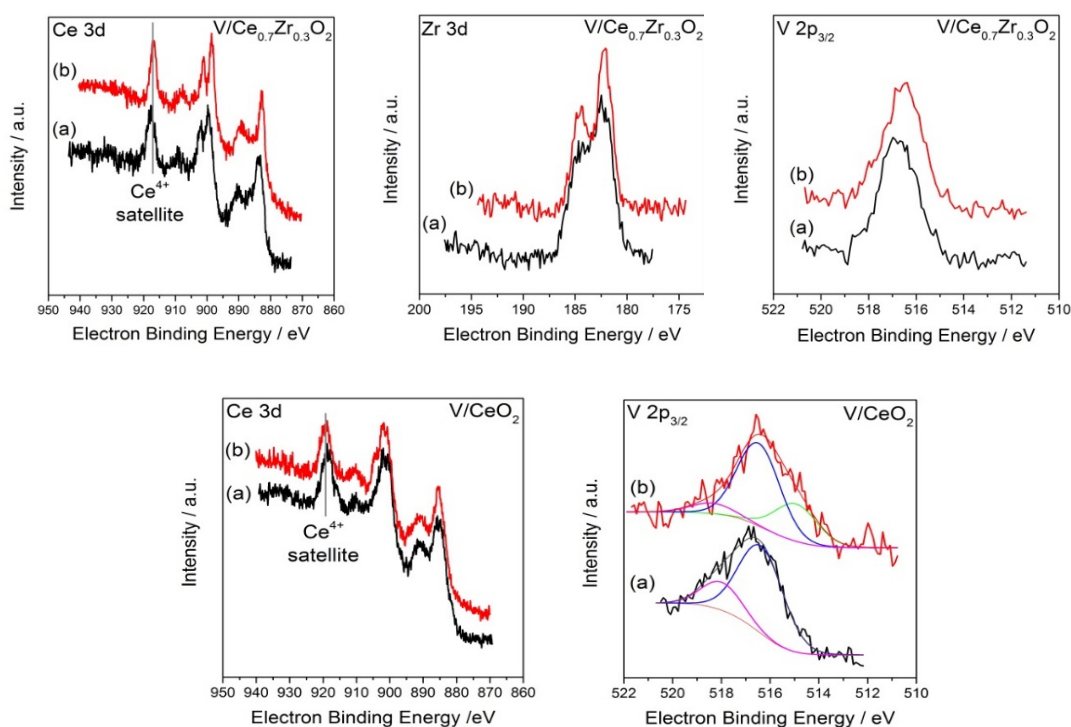


Figure 4.7: Pseudo-*in-situ*-XP spectra in the region of the Ce 3d, Zr 3d and V $2p_{3/2}$ peaks of catalysts $\text{V/Ce}_{0.7}\text{Zr}_{0.3}\text{O}_2$ (above) and V/CeO_2 (below) measured at room temperature before (a) and after treatment in a flow of 0.4% NO , 0.4% NH_3 , 10% O_2/He and transfer to the analysis chamber without contact with the ambient atmosphere (b).

Interestingly, the V 2p_{3/2} spectra of V/CeO₂, before and after treatment in the reactant feed, are more complex than that of V/Ce_{0.7}Zr_{0.3}O₂. Next to the main peak at 516.6 eV a small shoulder at higher binding energy appeared at the sample before the treatment. This shoulder around 518 eV can be assigned to V⁵⁺ probably highly dispersed and in close contact with CeO₂. This shoulder almost disappeared after the treatment, but a new shoulder at 515 eV arose instead, correlating with trivalent V.¹⁵¹ This is markedly lower than in catalyst V/Ce_{0.7}Zr_{0.3}O₂ and suggests the partial formation of V³⁺ under SCR conditions on pure CeO₂. This may be another reason for the low activity of catalyst V/CeO₂. In summary, these XPS results suggest that the valence states of Ce and Zr are not affected by the SCR in contrast to V which shows some changes after the reactive treatment.

Additional information about the structure and behaviour of V sites in the catalysts has been obtained by *in-situ*-EPR spectroscopy. In Figure 4.8, EPR spectra are exemplarily shown for the most active catalyst V/Ce_{0.7}Zr_{0.3}O₂ (for spectra of the other catalysts see Figure A.8). After pretreatment in O₂ and NO/O₂, no V⁴⁺ species were exhibited. The signals in spectra (A) and (B) originate from species already present in the support and have been discussed above (compared to Figure 4.4). However, upon switching to the total SCR feed flow, the characteristic hfs signal of VO²⁺ appeared (Figure 4.8C). Spin-Hamiltonian parameters of this signal obtained by simulation of spectrum c are summarised in Table 4.4. To get excellent fits, a broad background signal with g_{iso} = 1.963 had to be superimposed in each fit which represents interacting VO²⁺ species but is not listed in Table 4.4.

It has to be recalled that EPR spectroscopy detects only VO²⁺ species with tetravalent V. However, these species can serve as monitors for structural differences of the corresponding VO³⁺ species from which they are formed by reduction. The parameters in Table 4.4 can be used to derive information on support-dependent structural differences of the V sites in the three catalysts.^{162, 177}

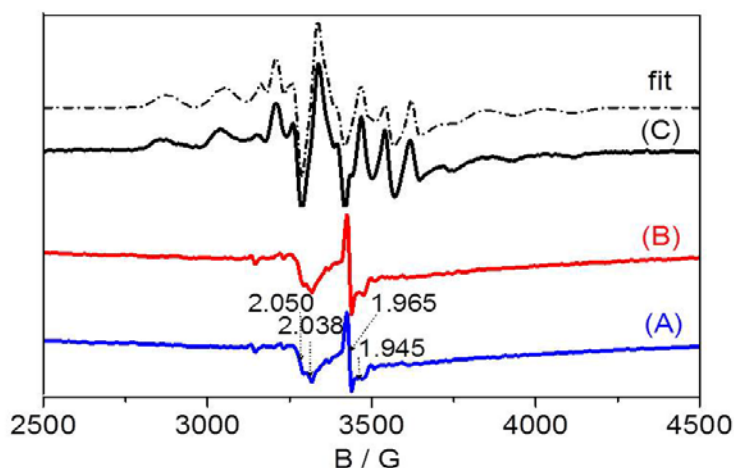


Figure 4.8: *In-situ* EPR spectra of sample V/Ce_{0.7}Zr_{0.3}O₂ recorded at room temperature after A) 1 h pretreatment in O₂ flow at 400 °C, B) 30 min exposure to 0.1% NO, 5% O₂/He and C) 30 min exposure to total SCR feed flow (spectrum B subtracted). The dashed line shows the spectrum fitted with spin Hamiltonian parameters in Table 4.4.

Thus, the parallel component of the hyperfine coupling tensor $A_{||}$ is a measure of the strength of the V=O bond. The higher this value, the shorter is this bond. The ratio $\Delta g_{||}/\Delta g_{\perp}$ with $\Delta g_{||} = g_{||} - g_e$ and $\Delta g_{\perp} = g_{\perp} - g_e$ ($g_e = 2.0023$) characterizes the total axial distortion. The higher this ratio, the shorter is the V=O bond and the longer are the V-O bonds in the equatorial plane of the VO^{2+} site.¹⁷⁷ The so-called in-plane delocalisation coefficient β_2^{*2} (E.q. 4.3, with $P = 184.5$ G being the strength of the electron-nuclear dipole-dipole interaction for the free V^{4+} ion¹⁷⁸) reflects the delocalisation of the unpaired electron of V^{4+} towards the ligands in the equatorial plane of the VO^{2+} species. It is a measure of the degree of covalence of the V-O bonds. For a purely ionic VO^{2+} species, this coefficient is equal to one. Increasing electron delocalisation towards the equatorial O ligands lowers β_2^{*2} and reflects the rising covalent character of the basal V-ligand bonds.^{177, 179}

Table 4.4: Spin-Hamiltonian parameters derived by simulation of difference spectra (NO/NH₃/O₂)-(NO/O₂) (Figure 4.8 and A.8).

Sample	$g_{ }$	g_{\perp}	$A_{ }$ (G)	A_{\perp} (G)	$\Delta g_{ }/\Delta g_{\perp}$	β_2^{*2}
V/CeO ₂	1.922	1.978	182.5	64.0	3.30	0.83
V/ZrO ₂	1.922	1.979	189.5	65.5	3.30	0.87
V/Ce _{0.7} Zr _{0.3} O ₂	A) 1.930	1.970	175.0	59.0	2.24	0.80
	B)* 1.924	1.978	185.5	64.0	3.23	0.85

* amounts to $\approx 20\%$ of all single V^{4+} species

$$\beta_2^{*2} = \left(\frac{7}{6}\right)\Delta g_{||} - \left(\frac{5}{12}\right)\Delta g_{\perp} - \left(\frac{7}{6}\right)\left[\frac{A_{||} - A_{\perp}}{P}\right] \quad (4.3)$$

As can be seen from Table 4.4, the hfs spectrum of catalysts V/ZrO₂ and V/CeO₂ could be fitted with one single VO^{2+} site while two different VO^{2+} species A and B had to be assumed for V/Ce_{0.7}Zr_{0.3}O₂. The spin Hamiltonian parameters of the single VO^{2+} sites supported on the pure ZrO₂ and CeO₂ oxides are rather similar to each other and to site B on the mixed oxide. In contrast, VO^{2+} site A on Ce_{0.7}Zr_{0.3}O₂ differs significantly in its structure. The smaller $A_{||}$ and $\Delta g_{||}/\Delta g_{\perp}$ values suggest that this species is less distorted. Its in-plane delocalisation coefficient β_2^{*2} is slightly lower compared to values of the other VO^{2+} species which may indicate a somewhat more covalent and more efficient bonding to the support via V-O-M bridges (M = Zr, Ce). Since V sites A were exclusively observed in the mixed oxide support, we tentatively assign them to V sites incorporated in –O–Ce–O–V(=O)–O–Zr–O– surface moieties. Presumably, this attachment is responsible for the fast redox behaviour evidenced by UV-Vis-DRS (Figure 4.6, Table 4.3).

4.4. Conclusions

Supported V/Ce_{1-x}Zr_xO₂ catalysts with x = 0.1-0.3 and a vanadia loading of 5 wt.% revealed to be promising catalysts for low-temperature NH₃-SCR of NO, reaching almost 100% of both, NO conversion and N₂ selectivity at 220 °C with substantially no deactivation during at least 190 hours and under a space velocity of 70,000 h⁻¹, which is markedly higher than the state of the art. No undesired formation of N₂O was observed. In contrast, when the pure oxides CeO₂ or ZrO₂ were used as supports instead of the binary Ce_{1-x}Zr_xO₂ phases, the resulting catalysts were markedly less active. This may be explained by significant differences in the nature of the VO_x species which have been shown to participate as active sites in reversible redox cycles under reaction conditions, in which they shuttled between V⁵⁺ and V⁴⁺ (detected by *in-situ*-EPR) while Ce⁴⁺ and Zr⁴⁺ did obviously not change their valence states (confirmed by pseudo-*in-situ*-XPS). All catalysts were dominated by more or less polymerised VO_{4+x} species, whereby the extent of polymerization seems to be slightly higher on the binary mixed oxide supports and pure CeO₂ compared to pure ZrO₂. In the latter case, significant amounts of VO²⁺ species were incorporated into the bulk of the support, most probably on Zr⁴⁺ lattice positions, where they might not be accessible by reactants. This is regarded as a primary reason for the lower activity of V/ZrO₂ catalysts, which contain fewer V sites on the surface than catalysts based on pure CeO₂ and Ce_{1-x}Zr_xO₂. In contrast to V/ZrO₂, the even lower activity of V/CeO₂ is supposed to have other reasons since the surface V/Ce ratio was by a factor of 2 higher than the surface V/Zr ratio. In this catalyst, the rates of reduction and reoxidation of VO_x surface sites were by far the lowest compared to the other catalysts. Since efficient and reversible reduction/reoxidation cycles are essential for catalysts working via a Mars-van Krevelen mechanism (which has been shown to be the case for ceria supported VO_x),¹⁸⁰⁻¹⁸¹ such slow periods may be a primary reason for the low activity of V/CeO₂. Moreover, pseudo-*in-situ*-XPS data suggest that a significant part of the surface V sites may be reduced to inactive V³⁺ species under SCR conditions. For the most active catalyst V/Ce_{0.7}Zr_{0.3}O₂, reduction and reoxidation of surface VO_x sites were fastest. Moreover, EPR data suggest an efficient attachment of these VO_x sites to the support surface, probably within –O–Ce–O–V(=O)–O–Zr–O– surface moieties, which themselves may support the redox behaviour of the V sites.

5. V₂O₅/Ce_{1-x}Ti_xO₂ catalysts

The previous chapter showed that incorporation of Zr into ceria creates efficient supports for V-based NH₃-SCR catalysts with improved redox behaviour of vanadium active sites due to the formation of special–O–Ce–O–V(=O)–O–Zr–O– surface moieties. Motivated by these results, mixed oxide supports containing ceria in junction with a more redox-active co-component such as titania are expected to be even more active catalysts for low-temperature SCR of NO.¹⁸² Indeed, such systems have been recognised as being promising in a few recent papers. Lian⁷¹ prepared a 3% V₂O₅/CeTiO₂ catalyst for deNO_x and achieved 90% of NO_x conversion at 200 °C, yet only at a GHSV of 50,000 h⁻¹. At higher GHSV values of 128,000 h⁻¹ and 100,000 h⁻¹, a higher temperature of 250-300 °C is required to obtain almost full NO_x conversion over 1% V₂O₅ – 5% CeO₂/TiO₂ and 7% V₂O₅ – 20% CeO₂/TiO₂ catalysts.^{29, 183} Thus, a series of V₂O₅/Ce_{1-x}Ti_xO₂ catalysts with different Ce/Ti ratios has been prepared and analysed in NH₃-SCR at low temperature with respect to the catalytic behaviour (section 5.1) and the influence of titania on structure, surface and redox properties of supports and catalysts as well as on structure-performance relationships (section 5.2).

5.1. Catalytic performance of V₂O₅/Ce_{1-x}Ti_xO₂

Figure 5.1 illustrates the impact of temperature on NO_x, NH₃ conversion, and N₂ selectivity for all catalysts in comparison to the corresponding bare supports. It can be clearly seen that, apart from pure CeO₂ and TiO₂, even the Ce_xTi_{1-x}O₂ supports exhibited significant activity which raised upon replacement of about one third of the Ce sites by Ti and did not change much upon further increasing the Ti content (compared Ce_{0.7}Ti_{0.3}O₂ and Ce_{0.5}Ti_{0.5}O₂), reaching complete NO and NH₃ conversion in the range between 225 °C to 300 °C. The performance of the corresponding supported vanadia catalysts was significantly higher than that of the pure supports. The best V/Ce_{0.7}Ti_{0.3}O₂ and V/Ce_{0.5}Ti_{0.5}O₂ catalysts already reached full conversion slightly below 200 °C.

To optimise the V loading, apart from catalysts with 5% V₂O₅, samples with 3 and 7% V₂O₅ deposited on the most active support Ce_{0.5}Ti_{0.5}O₂ have also prepared. Moreover, a commercial 2% V₂O₅/8% WO₃-TiO₂ catalyst has been tested for comparison. In all cases, the catalytic performance was lower than that of the best 5% V₂O₅/Ce_{0.5}Ti_{0.5}O₂ catalyst (Figure A.9A). Therefore, these samples are not included in further studies described below. It should be mentioned that an optimum loading of 5% V₂O₅ has been identified, too, in chapter 4 for V₂O₅/Ce_{1-x}Zr_xO₂ catalysts, which is also in agreement with the observations of Li *et al.*¹²

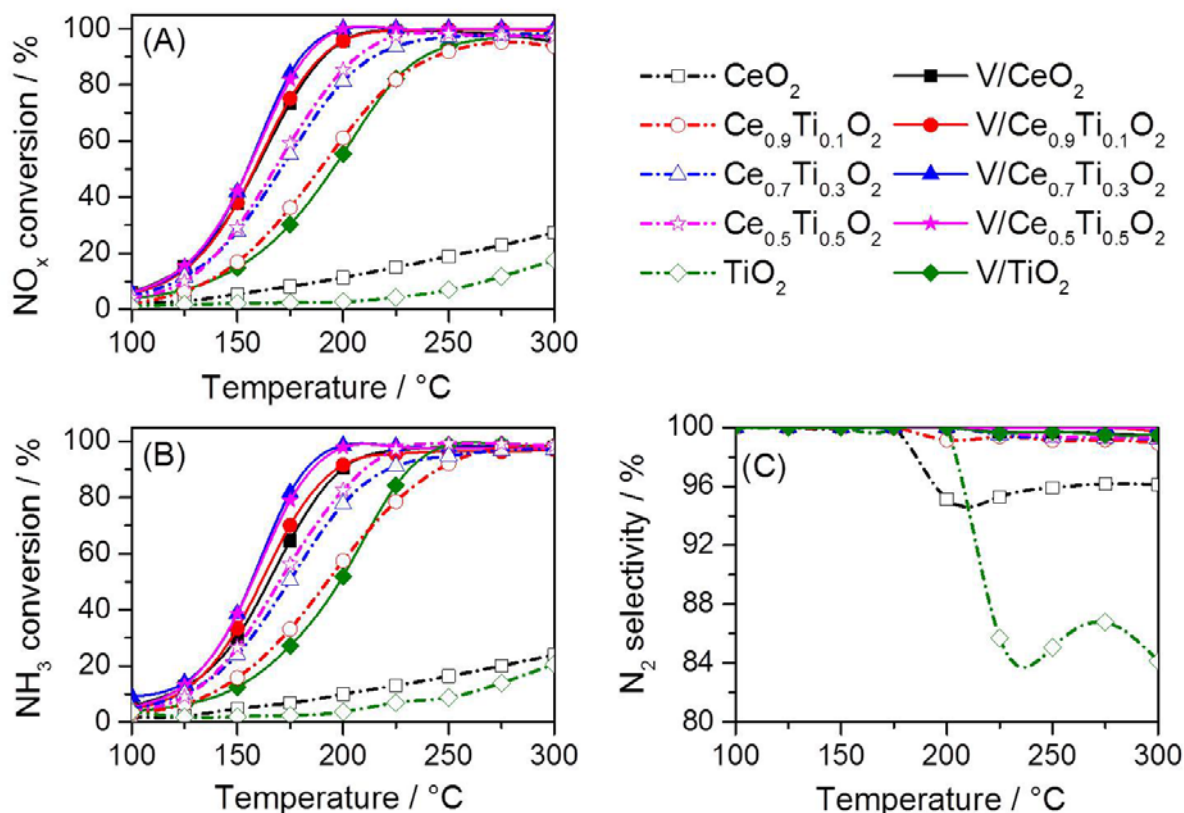


Figure 5.1: NO (A), NH₃ (B) conversion, and N₂ selectivity (C) over pure Ce_{1-x}Ti_xO₂ supports (open symbols, dashed lines) and respective V/Ce_{1-x}Ti_xO₂ catalysts (filled symbols, solid lines) as a function of temperature. Feed composition: 0.1% NO, 0.1% NH₃, 5% O₂/He, GHSV = 70,000 h⁻¹.

Interestingly, the gain in catalytic activity upon vanadia deposition increases in the same order as activity improvement of V-free supports: TiO₂ < CeO₂ << Ce_{0.9}Ti_{0.1}O₂ < Ce_{0.7}Ti_{0.3}O₂ ≈ Ce_{0.5}Ti_{0.5}O₂. This result indicates that the activity of supported vanadia catalysts strongly depends on the properties of supports. On the first glance, one could assume that this behaviour is related to an increase of the specific surface area since the S_{BET} values followed the same trend (see Table 5.1 below). However, surface areas are most probably not a major factor governing catalytic activity. This is obvious from comparing NO conversions of two 5% V/TiO₂ catalysts prepared by the same synthesis procedure but with TiO₂ supports of very different surface area ($S_{\text{BET}} = 18.6 \text{ m}^2\text{g}^{-1}$ and $S_{\text{BET}} = 350 \text{ m}^2\text{g}^{-1}$, Figure A.9B). The two catalysts exhibited almost the same activity despite the huge difference in surface area. A similar observation was also made by Wachs *et al.*¹⁸⁴ in the investigation of NH₃-SCR over a series of supported vanadia catalysts. In this work, the catalytic performance decreased in the order V/TiO₂ > V/Al₂O₃ > V/SiO₂ although the BET surface area of the supports increased in the reverse order TiO₂ (50 m²/g) < Al₂O₃ (180 m²/g) < SiO₂ (300 m²/g). Wachs *et al.* anticipated that it is the interface between the deposited vanadia and the support rather than the BET surface area of

the latter which is crucial for catalytic activity since this might govern the redox behaviour of the catalysts. Obviously, the same is true for the catalysts studied in this thesis.

As expected from the almost equal slope of the NO and NH₃ conversion curves, N₂ selectivity was close to 100% for all catalysts, except for the bare CeO₂ and TiO₂. In the case of latter, N₂ selectivity was slightly lower due to the formation of some N₂O, which did not occur regarding V-containing catalysts.

For practical applications in diesel or lean-burn engines, the volume of the catalysts should be as small as possible since catalytic converters have a limited volume only.^{12, 185} This requires that the catalysts must enable high conversions even at short contact times. Therefore, further efforts were conducted to investigate the effect of GHSV on the catalytic behaviour of the V/Ce_{1-x}Ti_xO₂ catalysts. As illustrated in Figure 5.2, the NO conversion over all catalysts decreased significantly when the GHSV is raised from 70,000 to 300,000 h⁻¹ and further to 750,000 h⁻¹ in the whole temperature range (compared Figure 5.1A to Figure 5.2A). However, the best catalyst (V/Ce_{0.5}Ti_{0.5}O₂) was still remarkably active below 300 °C with X(NO) ≈ 70% at GHSV = 300,000 h⁻¹ and X(NO) ≈ 50% at 750,000 h⁻¹.

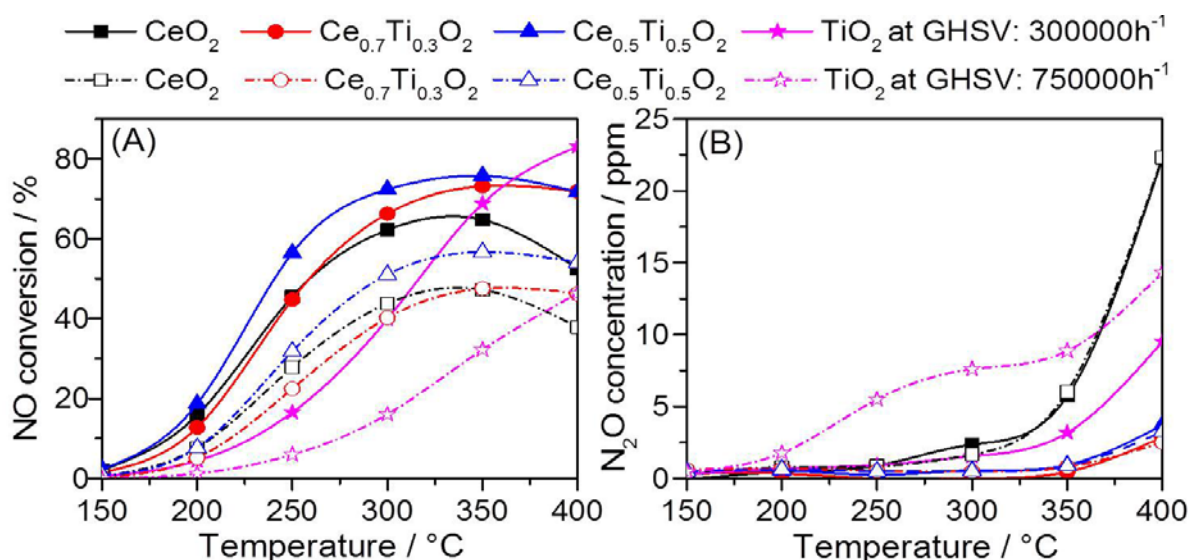


Figure 5.2: NO conversion (A) and N₂O concentration (B) over V/Ce_{1-x}Ti_xO₂ catalysts (x = 0, 0.3, 0.5 and 1) at a GHSV of 300,000 h⁻¹ (filled symbols, solid lines) and 750,000 h⁻¹ (open symbols, dashed lines) as a function of temperature. Feed composition: 0.1% NO, 0.1% NH₃, 5% O₂/He.

Moreover, the undesired formation of N₂O remained negligible over the whole temperature range with the best mixed oxide catalysts V/Ce_{0.7}Ti_{0.3}O₂ and V/Ce_{0.5}Ti_{0.5}O₂, while that became significant in the case of V/TiO₂ and V/CeO₂ particularly at higher temperatures (Figure 5.2B). This demonstrates that incorporation of titanium into ceria does not only help to retain high activity but also

high N₂ selectivity, which is impressed as a promising basis for further catalyst optimisation.

5.2. Effect of Ti on the structure and redox properties of V₂O₅/Ce_{1-x}Ti_xO₂ catalysts

In order to clarify the beneficial role of Ti for the performance of V/Ce_{1-x}Ti_xO₂ catalysts in NH₃-SCR, a comprehensive characterization study has been conducted. The following description of results in this section is, however, mainly restricted to the best VO_x/Ce_{0.5}Ti_{0.5}O₂ catalyst in comparison to V/CeO₂ and V/TiO₂.

5.2.1. Physicochemical properties of V₂O₅/Ce_{1-x}Ti_xO₂ catalysts

The XRD powder patterns in Figure 5.3A indicate that pristine TiO₂ exclusively exhibited anatase phase while CeO₂ obeyed the cubic fluorite structure. The latter also persisted upon incorporation of Ti, yet all reflections became broader with rising Ti content (Figure 5.3A). These effects indicate a decrease in crystallite size (Table 5.1) and/or higher lattice disorder and confirm the formation of solid solutions Ce_{1-x}Ti_xO₂.^{87, 146} These results are explained by the replacement of Ce⁴⁺ (97 pm) in the fluorite structure by smaller Ti⁴⁺ ions (74 pm). The XRD patterns of the corresponding V-containing mixed oxide catalysts (Figure 5.3B) did not contain any additional reflections, pointing to highly dispersed and/or amorphous vanadium oxide species on the surface of the supports.

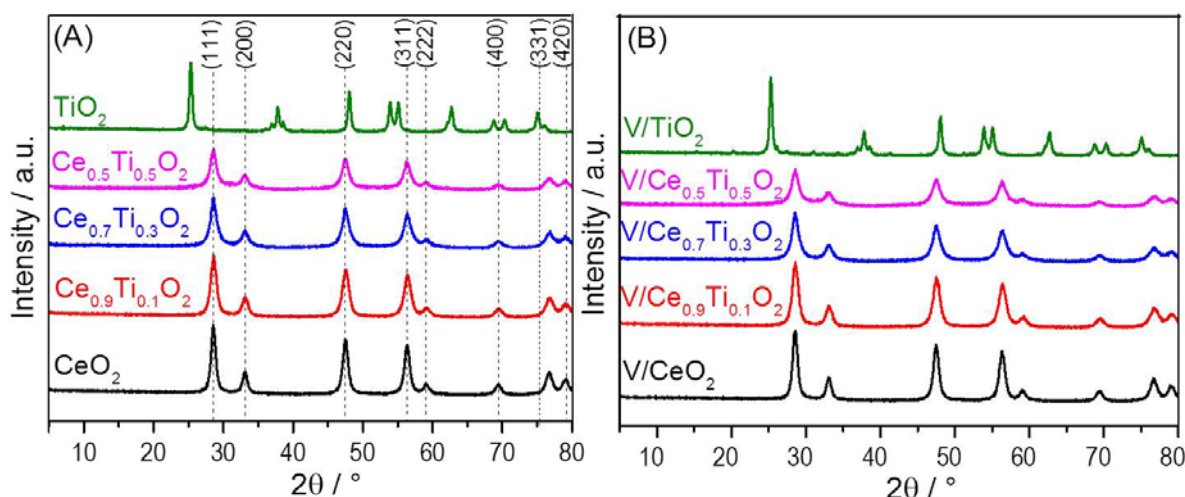


Figure 5.3: X-ray diffraction patterns of pure supports Ce_{1-x}Ti_xO₂ (A) and 5% V₂O₅/Ce_{1-x}Ti_xO₂ catalysts (B).

As summarised in Table 5.1, BET surface areas and pore volumes were significantly enhanced upon incorporation of Ti into CeO₂. The highest BET of 113.5 m²g⁻¹ was observed for Ce_{0.5}Ti_{0.5}O₂. These values did not change much upon

deposition of vanadia, indicating that pore blockage is negligible. The pore size distribution of all supports and catalysts did not differ much and was in the range of 3 to 7 nm in good accordance with previous reports.¹⁸⁶

Table 5.1: Crystallite size, specific surface area and pore volume, band gap energy of supports and catalysts.

Sample	Mean crystallite size (nm) ^[a]	Surface area (m ² g ⁻¹)	Pore volume (cm ³ g ⁻¹)	Average pore size (nm)	Band gap energy (eV) ^[b]
CeO ₂	10.8	61.2	0.060	3.16	2.72
Ce _{0.9} Ti _{0.1} O ₂	10.0	94.9	0.188	6.54	2.86
Ce _{0.7} Ti _{0.3} O ₂	8.7	91.1	0.134	4.74	2.66
Ce _{0.5} Ti _{0.5} O ₂	8.3	113.5	0.169	4.44	2.70
TiO ₂	24.0	20.1	0.025	3.06	2.90
V/ CeO ₂	10.8	45.4	0.053	3.63	2.25
V/Ce _{0.9} Ti _{0.1} O ₂	10.5	73.2	0.162	7.05	2.65
V/Ce _{0.7} Ti _{0.3} O ₂	8.6	77.2	0.128	5.10	2.60
V/Ce _{0.5} Ti _{0.5} O ₂	6.2	119.0	0.157	4.10	2.57
V/TiO ₂	23.0	18.6	0.025	3.64	2.11

^a derived by the Scherrer E.q. from XRD data, ^b results from UV-Vis -DRS

Table 5.2 summarises the surface composition and valence states derived from XPS measurements. The corresponding spectra are shown in the appendix (Figure A.10). The Ti 2p E_B values of both catalysts V/TiO₂ and V/Ce_{0.5}Ti_{0.5}O₂ after oxidative pretreatment correspond to Ti⁴⁺ states (459.1 – 458.8 eV).¹⁸⁶⁻¹⁸⁷ Moreover, samples V/CeO₂ and V/Ce_{0.5}Ti_{0.5}O₂ consisted of exclusively Ce⁴⁺, indicated by main peaks at 919 eV and 901 eV. Any peaks between 880 and 881 eV characteristic for Ce³⁺ was not found.^{20, 85, 150} The binding energies (E_B) of the O 1s peaks were very similar with that known for CeO₂, TiO₂, and their solid solutions.^{150, 186, 188-189} Sample V/TiO₂ exhibited a V 2p_{3/2} peak at about E_B = 517.2 eV being characteristic for V⁵⁺,^{148, 151, 155} together with a shoulder at E_B = 518.4 eV. The latter may be ascribed to highly dispersed VO_x species while the main peak around E_B ≈ 517 eV might arise from larger V₂O₅ nanocrystals.¹⁵¹

The presence of V₂O₅ nanocrystals has been evidenced in this sample by Raman spectra discussed below. In both samples V/CeO₂ and V/Ce_{0.5}Ti_{0.5}O₂, only one peak at 517.0-516.9 eV was observed, though in the V/Ce_{0.5}Ti_{0.5}O₂ catalyst, VO_x dispersion was highest and no V₂O₅ nanocrystals were found (*vide infra*). Possibly, the peak at 518.4 eV in V/TiO₂ originates from few V single sites persisting besides

the dominating tridimensional V_2O_5 clusters and nanoparticles, while the shift to lower E_B in $V/Ce_{0.5}Ti_{0.5}O_2$ resulted from abundant small V_xO_y clusters. In summary, all surface metal ions were in their highest valence state after oxidative pretreatment.

Table 5.2: XPS binding energies (eV) and surface atomic ratios obtained after treatment in air and SCR feed without contact to the ambient atmosphere.

Sample		Binding energy (eV)				Atomic ratio	
		O 1s	Ti 2p	V 2p _{3/2}	Ce 3d	Ce/Ti	V/(Ce+Ti)
V/CeO ₂	air	528.9	-	517.0	885.5	-	0.52
	SCR	529.0	-	516.2	885.5 882.5	-	0.44
V/Ce _{0.5} Ti _{0.5} O ₂	air	529.4	458.8	516.9	884.8	1.18	0.27
	SCR	529.4	458.9	516.9	884.8	1.51	0.20
V/TiO ₂	air	530.2	459.1	517.2 518.4	-	-	0.53
	SCR	530.1	458.4	517.2	-	-	0.41

The surface V/(Ce + Ti) ratios were equal to V supported on TiO₂ and CeO₂, being almost twice as high as on the mixed oxide support (Table 5.2). A possible explanation may be the much higher BET surface area of Ce_{0.5}Ti_{0.5}O₂ which could lead to a lower V surface concentration at the same total V₂O₅ content of 5 wt.%, despite a greater dispersion of the VO_x sites.

EPR spectra of fresh catalysts were almost alike with those of the bare supports, exhibiting only weak signals of paramagnetic oxygen defects such as O[•] and/or O₂[•] species.¹⁹⁰ An exception was V/TiO₂, in which a broad signal of magnetically interacting VO²⁺ species was observed around $g = 1.963$ (Figure A.11). Since VO_x clusters might dominate in V/TiO₂, probably this signal resulted from partially reduced V sites in subsurface regions of these agglomerates, since, according to XPS results (Table 5.2), the surface of this catalyst exposed V⁵⁺ only.

As mentioned in chapter 4, UV-Vis-DRS is another useful method to provide information on the structure of VO_x species in the catalysts. However, in this case, the wavelength range below 400 nm was superimposed by LMCT transitions of Ce⁴⁺ and Ti⁴⁺ (Figure 5.4A), it is not possible to derive reliable conclusions about the coordination of V⁵⁺ single sites since the LMCT transitions of which fell into this range, too. Nevertheless, from the position of the absorption edge above 400 nm, at least qualitative information can be obtained about the extent of VO_x agglomeration, since it has been demonstrated that the edge energy derived from UV-Vis-DRS

(Table 5.1, Figure A.12) is related to the number of V-O-V bridges.¹⁹¹ For both samples V/TiO₂ and V/CeO₂, the lowest band gap energies $E_g = 2.11$ and 2.25 eV were observed, consistent with a rather low VO_x dispersion. In contrast, higher and similar E_g values of 2.57-2.65 eV have been derived for V/Ce_{1-x}Ti_xO₂ catalysts, suggesting the prevalence of highly dispersed VO_x sites on the surfaces of the mixed oxide supports. This is in accordance with Raman data discussed below and with EPR results described above.

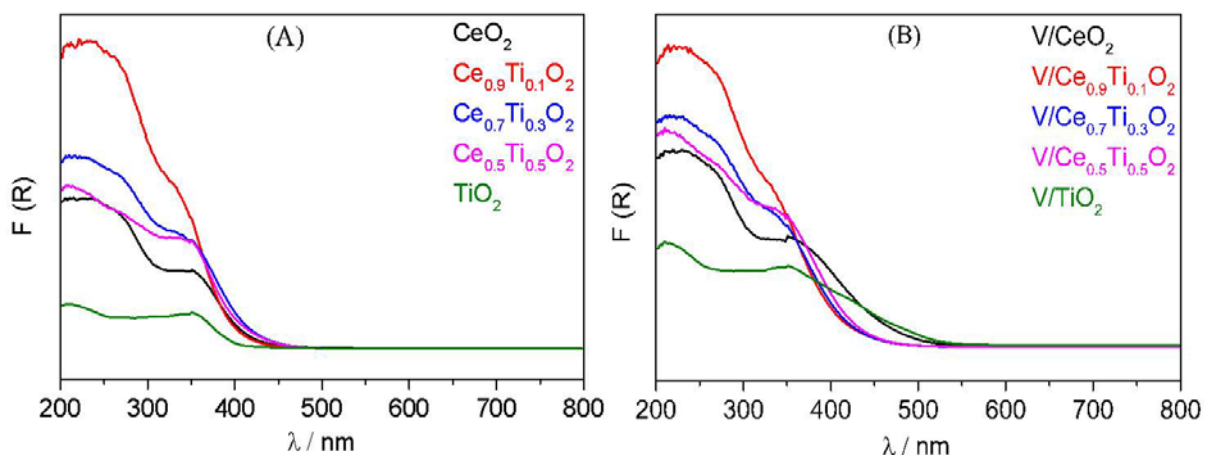


Figure 5.4: UV-Vis-DR spectra of (A) bare supports and (B) 5% V₂O₅/Ce_{1-x}Ti_xO₂ (V/Ce_{1-x}Ti_xO₂) catalysts.

These results are also supported by Raman spectra in Figure 5.5, in which some weak bands of (XRD-silent) nanocrystalline V₂O₅ at 145, 195, 282, 702, 864, and 994 cm⁻¹,^{187, 192} besides the typical bands of ceria at 463 cm⁻¹,¹⁸⁷⁻¹⁸⁸ and of anatase at 144, 395, 515, and 614 cm⁻¹, respectively were observed over catalysts V/CeO₂ and V/TiO₂.^{187, 193} The V/Ce_{1-x}Ti_xO₂ catalysts exhibited only the band of cubic ceria at 463 cm⁻¹, yet with lower intensity compared to that of V/CeO₂ due to

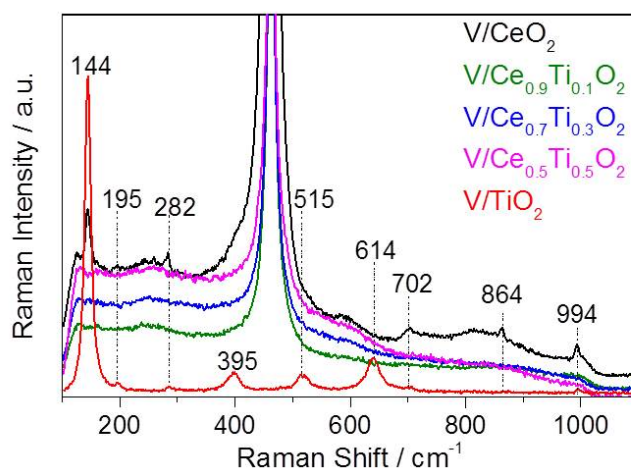


Figure 5.5: Raman spectra of the catalysts V/Ce_{1-x}Ti_xO₂ (x = 0-1).

decreasing crystallite size and/or increasing structural disorder with rising Ti content (Table 5.1). No Raman bands of V₂O₅ nanocrystals were detected in these catalysts, indicating that the incorporation of titanium into ceria enhanced the dispersion of deposited VO_x surface sites.

Pyridine adsorption studied by FTIR spectroscopy has been conducted for further investigation of the acidity of supports and catalysts at a temperature of 200 °C being relevant for catalytic activity (Figure 5.6). All samples showed bands at 1608-1599 and 1445-1442 cm^{-1} which can be assigned to pyridine coordinated to Lewis acid sites (L-Py).¹⁹⁴⁻¹⁹⁵ It has been proposed that the position of the $\nu(8a)$ vibration in the range between 1590 and 1630 cm^{-1} depends on the strength of Lewis sites.¹¹⁶ The more these bands are shifted to higher wavenumbers, the stronger are the corresponding Lewis sites. Inspection of Figure 5.6A and 5.6B shows that the Lewis sites of bare TiO_2 and V/TiO_2 give rise to bands at almost the same position (1605 and 1607 cm^{-1}), suggesting similar Lewis strength of Ti^{4+} and V^{5+} sites. In comparison, Ce^{4+} might be a weaker Lewis site as supported by the shift to lower wavenumbers in the bare CeO_2 support (1600 cm^{-1}) and the V/CeO_2 catalyst (1601 cm^{-1}).¹⁹⁶ In the case of mixed oxide support $\text{Ce}_{0.5}\text{Ti}_{0.5}\text{O}_2$ and the corresponding V-catalyst, this band is located at an intermediate position, probably due to the superposition of Lewis sites related to Ce^{4+} , Ti^{4+} , and V^{5+} .

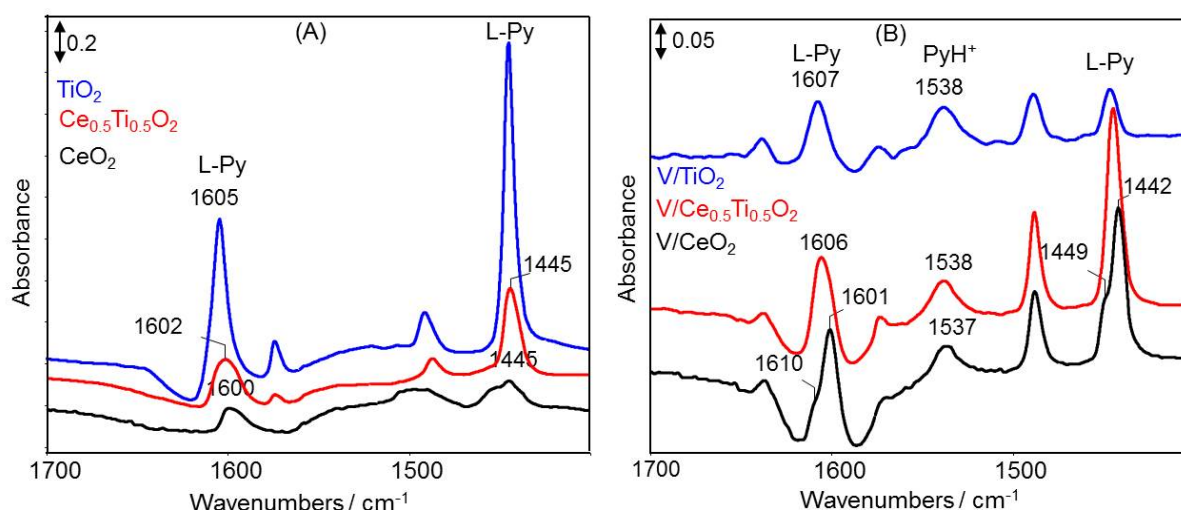


Figure 5.6: FTIR spectra of adsorbed pyridine on bare supports $\text{Ce}_{1-x}\text{Ti}_x\text{O}_2$ ($x = 0; 0.5; 1$) (A) and supported vanadium catalysts $\text{V/Ce}_{1-x}\text{Ti}_x\text{O}_2$ (B) recorded after evacuation at 200 °C.

Furthermore, the relative amount of Lewis sites reflected by the intensity of the L-Py band at 1445 cm^{-1} (Figure 5.6, I_{Lewis} in Table A.1) increased in the order $\text{CeO}_2 < \text{Ce}_{0.5}\text{Ti}_{0.5}\text{O}_2 \ll \text{TiO}_2$, indicating that incorporation of Ti into ceria resulted in a higher concentration of Lewis sites over $\text{Ce}_{1-x}\text{Ti}_x\text{O}_2$ supports. In the V-containing catalysts, the amount of Lewis sites decreased in the order $\text{V/Ce}_{0.5}\text{Ti}_{0.5}\text{O}_2 > \text{V/CeO}_2 > \text{V/TiO}_2$. The same trend was observed for the catalytic activity of the V-containing catalysts as well as for the pure Ce-containing supports (Figure 5.1). Thus, Lewis acidity may be beneficial for the SCR reaction, though it is not the primary factor since pure TiO_2 with the highest Lewis acidity exhibited the lowest catalytic activity. Interestingly, normalisation of the band area of the Lewis sites at 1445 cm^{-1} led to a

different order for the V-catalysts, which is not correlated with the trend in catalytic activity: $\text{V/CeO}_2 > \text{V/Ce}_{0.5}\text{Ti}_{0.5}\text{O}_2 \approx \text{V/TiO}_2$. This assumption again supports the conclusion proposed above that surface areas are most probably not a major factor governing catalytic activity.

It has been reported that bands at 1537 and 1635 cm^{-1} are related to PyH^+ ions, i. e. to pyridine adsorbed on Brønsted sites.^{116, 197} As illustrated in Figure 5.6, these weak bands were only observed in V-containing catalysts, probably, originated from V-OH groups. These bands were of almost equal intensity for all catalysts and were not consistent with observed differences in the catalytic behaviour, suggesting that Brønsted sites might not play a significant role in NH_3 -SCR of NO_x over these catalysts.

As explained in Section 2.4.3, reducibility may be an important catalyst property anticipating that NH_3 -SCR involves a Mars-van-Krevelen redox cycle.^{6, 118} Therefore, selected catalysts and the corresponding bare supports were also analysed by H_2 -TPR. However, as evident from Figure A.13, these results might be of rather limited relevance since measurable reduction under TPR conditions started only above 350 °C while the catalysts showed high activity already well below 200 °C. Therefore, the results obtained from *in-situ* spectroscopy, particularly those of *operando* EPR and *in-situ*-XPS described below, are certainly more relevant for assessing the redox properties of the catalysts during NH_3 -SCR, since they have been obtained under conditions very close or even identical to that of the catalytic reaction. Nevertheless, the TPR findings seem to be somehow in line with the observed trend in catalytic activity. The least active bare TiO_2 support showed negligible reducibility, followed by bare CeO_2 . In the case of CeO_2 , a weak broad signal with a maximum at 490 °C was seen, which can be assigned to the consumption of the surface capping oxygen of CeO_2 , while above 600 °C, reduction of bulk started.¹⁸⁶

Incorporation of Ti into ceria enhanced reducibility of $\text{Ce}_{0.5}\text{Ti}_{0.5}\text{O}_2$ reflected by higher H_2 uptake (Table A.2) and a shift of the peak maximum to lower temperature. Interestingly, a weak peak appeared already at about 225 °C in this sample, which can be assigned to the reduction of Ce tightly bound to Ti species.⁷¹ This could explain why the bare $\text{Ce}_{0.5}\text{Ti}_{0.5}\text{O}_2$ support was markedly more active than bare CeO_2 and TiO_2 (Figure 5.1). The peak maximum of the least active V/TiO_2 catalyst fell at significantly lower temperature compared to the more active samples V/CeO_2 and $\text{V/Ce}_{0.5}\text{Ti}_{0.5}\text{O}_2$, and this catalyst also showed the highest percentage of reduced V species under NH_3 -SCR conditions, as evident from *operando* EPR results described below. EPR and XPS results indicate that V/CeO_2 is markedly more reduced than $\text{V/Ce}_{0.5}\text{Ti}_{0.5}\text{O}_2$ under NH_3 -SCR conditions. This effect, which is discussed regarding its relevance for catalytic activity below, is hardly reflected by

TPR results, illustrating the limited usefulness of this method for the present catalytic system again.

5.2.2. Structure and redox behaviour of VO_x species visualised by *operando* EPR and pseudo-*in-situ*-XPS

Operando EPR spectra after subsequent treatment in different gas flows are exemplarily illustrated for the most active catalyst V/Ce_{0.5}Ti_{0.5}O₂ in Figure 5.7 (for the spectra of the others and results of the simultaneous mass spectrometric analysis of the effluent gas stream see Figure A.14 and A.15). After oxidative pretreatment, only weak signals tentatively attributed to paramagnetic oxygen defects in the support were observed (compare Figure A.11). Treatment in NH₃/He flow gave rise to the characteristic signal of VO²⁺ with hyperfine structure (hfs) from the coupling of the single electron spin of V⁴⁺ (d¹, S = ½) with the nuclear spin of V (I = 7/2, 100% natural abundance), indicating that V⁵⁺ is partially reduced in the presence of NH₃. This signal completely disappeared when the catalyst was subsequently exposed to a flow of 0.1% NO, 5% O₂/He (Figure 5.7C), pointing to reoxidation of reduced vanadyl species. Afterwards, upon switching to the total SCR feed flow, the hfs signal of VO²⁺ reappeared, yet with lower intensity, suggesting that an equilibrium V valence state is established under reaction conditions. Interestingly, the total EPR intensity of the most active V/Ce_{0.5}Ti_{0.5}O₂ catalyst under SCR conditions was significantly lower compared to that of the less active V/CeO₂ and V/TiO₂ catalysts (Figure 5.7, right). This result indicates the highest equilibrium concentration of V⁵⁺ in the active state for the most active catalyst.

As shown previously for the V/Ce_{1-x}Zr_xO₂ system in chapter 4,¹⁴⁵ spin Hamiltonian parameters of the EPR spectra under SCR feed provide valuable information about the location and structure of single V⁴⁺=O sites, being also considered as emblematic of corresponding EPR-silent V⁵⁺ species from which they have been formed by reduction.^{177, 198} Thus, A_{||} increases when the V=O bond shortens, Δg_{||}/Δg_⊥ (with Δg_{||} = g_{||} - g_e, Δg_⊥ = g_⊥ - g_e, g_e = 2.0023) increases with rising axial distortion, and the calculated coefficient β₂^{*}² (E.q. 4.3, with P = 184.5 G being the strength of the electron-nuclear dipole-dipole interaction for the free V⁴⁺ ion)¹⁹⁹ is an indication of the degree of covalence of the V-O bonds. This coefficient is unity for a pure VO²⁺ cation and decreases with increasing covalent character.^{177, 179}

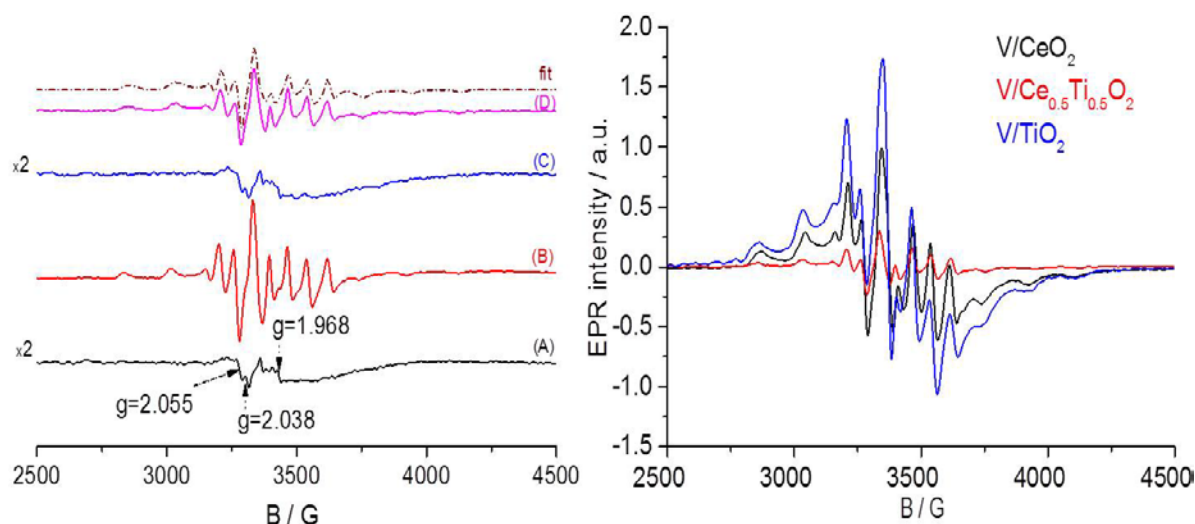


Figure 5.7: Left: *Operando* EPR spectra of sample V/Ce_{0.5}Ti_{0.5}O₂ recorded at 20 °C after (A) 1 h pretreatment in O₂ flow at 300 °C, (B) 30 min exposure to 0.1% NH₃/Ar (C) 30 min exposure to 0.1% NO, 5% O₂/Ar and (D) 30 min exposure to total SCR feed flow (spectrum c subtracted, dashed line shows spectrum fitted with spin Hamiltonian parameters in Table 5.3); Right: Comparison of spectra (D) for V/CeO₂, V/Ce_{0.5}Ti_{0.5}O₂ and V/TiO₂.

For all catalysts, two hfs signals A and B for different single VO²⁺ species and a broad isotropic singlet C for magnetically interacting VO²⁺ species were required to obtain satisfactory fits of the experimental spectra (Table 5.3, Figure 5.7 and A.14). First of all, it can be clearly seen that the contribution of the broad singlet C decreased in the order V/TiO₂ > V/CeO₂ > V/Ce_{0.5}Ti_{0.5}O₂, which agrees well with the dispersion of VO_x sites being highest for the catalyst with the mixed oxide support. Moreover, the similarity of the parameters of the single VO²⁺ sites A suggests that these species might have a similar environment in all three catalysts. Possibly, they are located more in subsurface regions of the V₂O₅ agglomerates without direct contact to the surface of support, while sites B may be rather sited on the support interface. Remarkably, the in-plane delocalisation coefficient β_2^{*2} of VO²⁺ sites B on the mixed oxide support Ce_{0.5}Ti_{0.5}O₂ was significantly lower than the respective values of those on pure CeO₂ and TiO₂, indicating that the former are more covalent and, thus more effectively bound to the support.

A similar though the less significant effect was also found for the best catalyst V/Ce_{0.7}Zr_{0.3}O₂ from the V/Ce_{1-x}Zr_xO₂ series in the previous chapter.^{145 145} In analogy to these results, it can be proposed that the V sites B in catalyst V/Ce_{0.5}Ti_{0.5}O₂ may be part of –O–Ce–O–V(=O)–O–Ti–O– surface moieties. This confinement could facilitate electron transfer between the Vⁿ⁺=O site and the support and, thus, promote redox activity of these sites. It should be mentioned that the best catalyst for the V/Ce_{1-x}Ti_xO₂ series is more active than the corresponding catalyst from the V/Ce_{1-x}Zr_xO₂ series might be due to the higher redox potential of Ti compared to Zr.²⁰⁰

Table 5.3: Spin-Hamiltonian parameters derived by simulation of the difference EPR spectrum (NO/NH₃/O₂)-(NO/O₂) of V/Ce_{1-x}Ti_xO₂ catalysts.

	V species	$g_{ }$	g_{\perp}	$A_{ } / G$	A_{\perp} / G	$\Delta g_{ }/\Delta g_{\perp}$	β_2^{*2}	$I_{rel} / \%$
V/CeO ₂	a	1.922	1.976	185.4	62.6	3.05	0.859	19
	b	1.933	1.967	175.7	55.8	1.96	0.824	24
	c	1.963		-	-	-	-	57
V/Ce _{0.5} Ti _{0.5} O ₂	a	1.924	1.977	180.0	63.5	3.14	0.818	35
	b	1.933	1.964	182.5	77.3	1.81	0.730	38
	c	1.963		-	-	-	-	27
V/TiO ₂	a	1.927	1.979	179.9	63.4	3.16	0.814	10
	b	1.938	1.971	178.3	52.5	2.05	0.857	11
	c	1.963		-	-	-	-	79

Since EPR can only detect V⁴⁺ at temperatures ≥ 20 °C, pseudo-*in-situ*-XPS experiments have been carried out after treatment of the catalysts in a reaction chamber attached to the spectrometer to further analyse the behaviour of Ceⁿ⁺ and Tiⁿ⁺ in addition to Vⁿ⁺.

As discussed above, all surface metal ions were in their highest valence state after oxidative pretreatment (Section 5.2.1, Table 5.2). After treatment in SCR feed, the V 2p_{3/2} signal of the most active catalyst V/Ce_{0.5}Ti_{0.5}O₂ remained almost at the same position (516.9 eV) indicating that the majority of the surface V species stays pentavalent. In contrast, this peak shifted to lower binding energy after SCR in sample V/CeO₂, and in catalyst V/TiO₂ the shoulder at 518.4 eV vanished. This points, in agreement with *operando* EPR data, to a partial reduction of V⁵⁺ to V⁴⁺ (Table 5.3). This effect is hardly detectable for the most active catalyst V/Ce_{0.5}Ti_{0.5}O₂ which is also in accordance with the much smaller VO²⁺ EPR signal intensity of this catalyst after SCR treatment in comparison to that of V/TiO₂ and V/CeO₂ (Figure 5.7, right).

The Ti 2p binding energies were between 458.4 and 459.1 eV in both Ti-containing catalysts and did not change after SCR treatment, indicating that Ti remains essentially tetravalent.¹⁸⁶⁻¹⁸⁷ Similar behaviour was observed for cerium in the mixed oxide support of V/Ce_{0.5}Ti_{0.5}O₂. In contrast, a partial reduction of Ce⁴⁺ to Ce³⁺ under SCR conditions was seen for V/CeO₂ from the presence of a shoulder at 882.5 eV. This assumption is particularly interesting since such reduction has not been observed under SCR feed in the previous study of V/Ce_{1-x}Zr_xO₂ catalysts in chapter 4, in which, however, the CeO₂ support was prepared by a citrate method. It

demonstrates that the synthesis procedure might have a critical impact on the redox properties and, thus the catalytic activity of V/CeO₂ materials.

The V/(Ce + Ti) surface ratio decreased slightly for all catalysts after SCR, suggesting diffusion of a minor amount of V into subsurface layers and/or an agglomeration of dispersed VO_x sites. However, these effects were almost negligible. More significant was the increase of the Ce/Ti ratio in the V/Ce_{0.5}Ti_{0.5}O₂ catalyst which points to an enrichment of Ce on the surface.

5.3. Mechanism of NH₃-SCR over Ce_{1-x}Ti_xO₂ and V₂O₅/Ce_{1-x}Ti_xO₂ catalysts

Results of *operando* EPR and pseudo-*in-situ*-XPS have been previously described in the section 5.2.2 allowing to conclude reaction-dependent valence changes of V, Ce, and Ti. On the other hand, *in-situ*-DRIFTS can provide insights on the nature of adsorbed intermediates formed upon interaction of feed components with surface sites, which is, then, conclusive proof for the accurate determination of the reaction mechanism. Moreover, it has been proposed previously for V₂O₅/TiO₂ catalysts that the SCR of NO by NH₃ comprises reaction steps catalysed by both acid and redox sites, though the interpretation of these results differs. While a direct correlation between NO conversion and the concentration of Brønsted sites (responsible for NH₃ adsorption as NH₄⁺) was postulated by Topsoe,³³ such a relationship was proposed between NO conversion and number of V⁵⁺=O redox sites but not the amount of adsorbed NH₄⁺ elsewhere.²⁰¹ In any case, these results show that it is of utmost importance to study the behaviour of V/Ce_{1-x}Ti_xO₂ catalysts under reaction conditions to derive reliable conclusions about mechanistic details. Therefore, *in-situ*-DRIFTS have been applied, the results of which are presented in this section.

In-situ-DRIFT spectra of the bare supports and the V-containing catalysts in flowing 0.1% NH₃/He consisted of bands at 3376-3150 cm⁻¹ arising from ν(N-H) stretching vibrations of NH₃ adsorbed on Lewis sites (see Figure A.16).^{30, 33} The corresponding bending vibrations were observed at 1225-1156 and 1603 cm⁻¹ (Figure 5.8).^{30, 33, 202} Among the catalysts, the intensities of these bands were highest for V/Ce_{0.5}Ti_{0.5}O₂ indicating the maximum amount of Lewis acid sites on this catalyst. Besides, additional bands at 1520-1510 cm⁻¹ of NH₂⁻ species,¹³⁶ were only

observed on pure CeO_2 and $\text{Ce}_{0.5}\text{Ti}_{0.5}\text{O}_2$, pointing to dissociative NH_3 adsorption on the support surface. The characteristic bands for NH_4^+ formed by the interaction of NH_3 with Brønsted sites around 1420 cm^{-1} were observed only for the V-containing catalysts and might originate from V-OH moieties.^{30, 33, 202} This is also supported by the negative band at $3646\text{--}3640\text{ cm}^{-1}$ in Figure A.16 which indicates the consumption of the latter. These results are in good agreement with pyridine adsorption data illustrated above in Section 5.2.1. Another negative band at 2043 cm^{-1} can be assigned to the 2ν overtone vibration of $\text{V}^{5+}=\text{O}$ groups which were partly reduced to $\text{V}^{4+}=\text{O}$ and/or covered by NH_3 .³³ This reduction was also evident from *in-situ*-XPS and *in-situ*-EPR data discussed in Section 5.2.2.

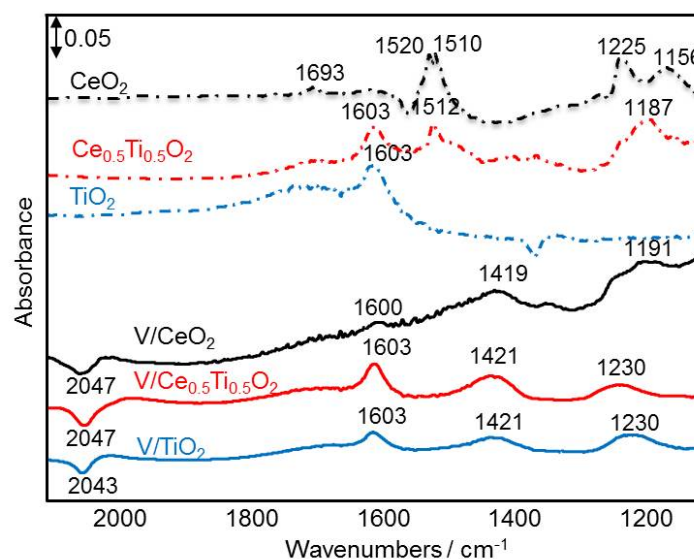


Figure 5.8: Difference DRIFT spectra of bare supports and supported vanadium catalysts recorded at $200\text{ }^{\circ}\text{C}$ after 45 min in $0.1\%\text{ NH}_3/\text{He}$ flow.

As the bare supports with preadsorbed NH_3 were subsequently treated at $200\text{ }^{\circ}\text{C}$ in a flow of $0.1\%\text{ NO}$, $5\%\text{ O}_2/\text{He}$, a similar behaviour was observed for CeO_2 and $\text{Ce}_{0.5}\text{Ti}_{0.5}\text{O}_2$, in which $\nu(\text{N-H})$ and $\delta(\text{N-H})$ bands of NH_3 adsorbed on Lewis sites above 3150 cm^{-1} (Figure A.17A) and between 1150 and 1603 cm^{-1} (Figure 5.9A) disappeared gradually, while new bands arose. Those below 1600 cm^{-1} are assigned to monodentate (1533 and $1258\text{--}1253\text{ cm}^{-1}$), bridged ($1600\text{--}1591$ and 1205 cm^{-1}) and bidentate nitrate species ($1570\text{--}1565$ and $1218\text{--}1200\text{ cm}^{-1}$).^{136, 203–204} The weak features located between 2200 and 1900 cm^{-1} may stem from combination bands of adsorbed NO_x species.^{205–206} Additionally, bands at $1995\text{--}1935\text{ cm}^{-1}$ of M-NO mononitrosyl species (M= Ce, Ti), adsorbed NO_2 (1689 cm^{-1}) and N_2O_4 ($1728\text{--}1726\text{ cm}^{-1}$) were also observed.¹³⁶ A broad band at 2220 cm^{-1} can be assigned to adsorbed NO^+ cations.^{136,207} In contrast, for pure TiO_2 , the spectra nearly did not change after switching from NH_3 to $\text{NO}+\text{O}_2$, indicating that adsorbed NH_3 is very stable and poorly reactive on this support surface. Note that this support also achieved negligible catalytic activity at $200\text{ }^{\circ}\text{C}$ (Figure 5.1).

Interestingly, on supported vanadium catalysts, the bands of preadsorbed NH_3 disappeared in the flow of $0.1\%\text{ NO}$, $5\%\text{ O}_2/\text{He}$, too. This happened much slower on the least active catalyst V/TiO_2 , pointing again to the high stability and poor

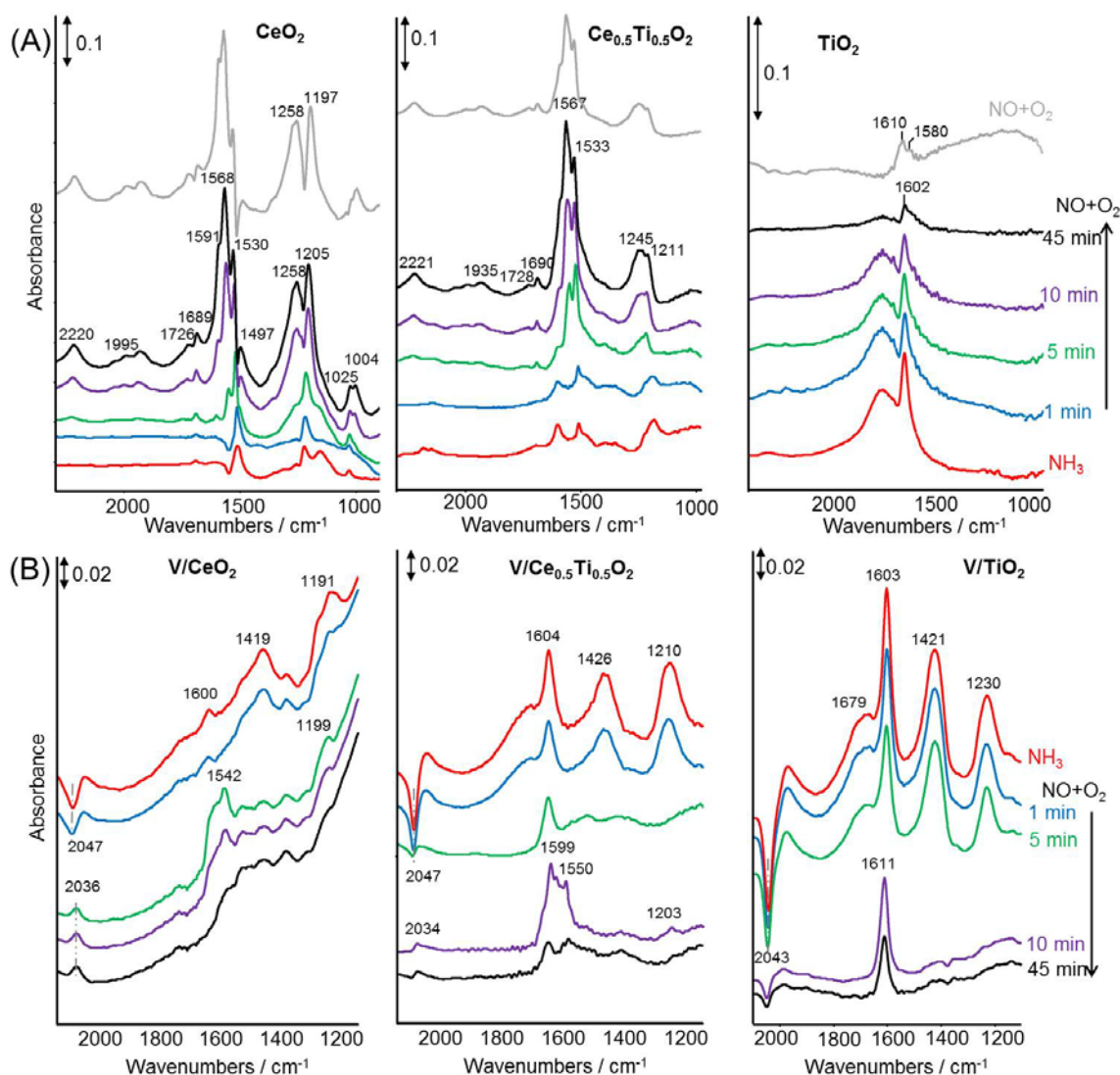


Figure 5.9: Difference DRIFT spectra recorded at 200 °C of bare supports (A) and V-containing catalysts (B) after 45 min exposure at 200 °C to 0.1% NH_3/He flow and subsequent switch to 0.1% NO , 5% O_2/He flow. Top traces in plot A depict spectra recorded after 45 min exclusive exposure to 0.1% NO , 5% O_2/He flow without pretreatment in NH_3/He . For plots of the range 2500-4000 cm^{-1} see Figure A.17.

reactivity of adsorbed NH_3 . Remarkably, no stable adsorbed nitrate, nitrosyl, and NO^+ ions were created (Figure 5.9B). Moreover, on both catalysts, V/CeO_2 and $\text{V/Ce}_{0.5}\text{Ti}_{0.5}\text{O}_2$, the negative intensities of the $2\nu(\text{V}=\text{O})$ and the $\nu(\text{V}-\text{O}-\text{H})$ bands at 2047-2043 cm^{-1} (Figure 5.9B) and 3646-3640 cm^{-1} (Figure A.17B), respectively, turned into positive features. This is probably due to the reoxidation of V^{4+} to $\text{V}^{5+}=\text{O}$ and $\text{V}^{5+}-\text{OH}$ surface sites, which is also supported by the decreasing EPR signal of VO^{2+} species under these conditions (Section 5.2.2, page 58). In contrast, for the least active catalyst V/TiO_2 , the $2\nu(\text{V}=\text{O})$ band remained negative, indicating that reoxidation of V^{4+} on this sample is much slower and more difficult, possibly due to coverage of these sites by adsorbed NH_3 . These results clearly demonstrate that

both V-OH Brønsted as well as V=O redox sites participate in the NH_3 -SCR mechanism. This assumption has been found previously for $\text{V}_2\text{O}_5/\text{TiO}_2$ and is here confirmed for $\text{V}/\text{Ce}_{1-x}\text{Ti}_x\text{O}_2$ catalysts, too.³³ In our case, however, the impact of V=O redox sites might be more important since the differences in Brønsted acidity between the V-containing catalysts were marginal (Figure 5.6 and 5.8).

In separate experiments, bare supports and catalysts were first exposed to NO/O_2 and subsequently to NH_3/He flow (Figure 5.10). After exposure to NO/O_2 , the same bands appeared as observed after first exposing to NH_3/He and afterwards to NO/O_2 flow (compare grey and black spectra in Figure 5.9A), confirming the formation of differently bound nitrate, M-NO (M= Ce, Ti) and NO^+ species on CeO_2 and $\text{Ce}_{0.5}\text{Ti}_{0.5}\text{O}_2$. On TiO_2 , the amount of adsorbed nitrates was much lower compared to that on CeO_2 and $\text{Ce}_{0.5}\text{Ti}_{0.5}\text{O}_2$, and no Ti-NO and NO^+ species were detected. This result suggests that nitrate formation from NO/O_2 might be promoted by the higher oxygen mobility and oxidation activity of Ce-containing supports. Moreover, the amount of these adsorbates is somewhat higher on CeO_2 , despite the lower BET surface area compared to $\text{Ce}_{0.5}\text{Ti}_{0.5}\text{O}_2$. Possibly, oxygen in the vicinity of Ce participates preferentially in nitrate formation (Table 5.1).

Interestingly, no bands at all were formed upon exposure of the V-containing catalysts to NO/O_2 flow at 200 °C (Figure A.18). Therefore, the corresponding reference spectra are not shown in Figure 5.9B. This evidences clearly that NO does not interact directly with the vanadium catalyst surface reacts from the gas phase with adsorbed NH_3 and NH_4^+ species whereby, however, no surface nitrates were created in the latter case (compare Figure 5.9B).

Upon subsequent exposure of the NO/O_2 -pretreated supports to a flow of 0.1% NH_3/He (Figure 5.10), on $\text{Ce}_{0.5}\text{Ti}_{0.5}\text{O}_2$, the bands of nitrates, M-NO (M = Ce, Ti) and NO^+ species decreased and bands already attributed for adsorbed NH_3 arose, indicating the reaction of adsorbed NO_x with (adsorbed) NH_3 most probably to N_2 and H_2O (compare red spectrum in Figure 5.9A with black line in Figure 5.10). In contrast, on pristine CeO_2 , the bands of all pre-adsorbed NO_x species did not change under NH_3/He flow at 200 °C (Figure 5.10), which clearly evidences that these species are stable against NH_3 attack. This might be one reason for the much lower catalytic activity of bare CeO_2 in comparison to $\text{Ce}_{0.5}\text{Ti}_{0.5}\text{O}_2$ (Figure 5.1). On TiO_2 , only weak bands of adsorbed NO_x species were formed during pretreatment in NO/O_2 which under NH_3/He flow were replaced immediately by adsorbed NH_3 (band at 1603 cm^{-1}). On V-containing catalysts (not shown in Figure 5.10), only rising bands of adsorbed NH_3 were observed (Figure A.18).

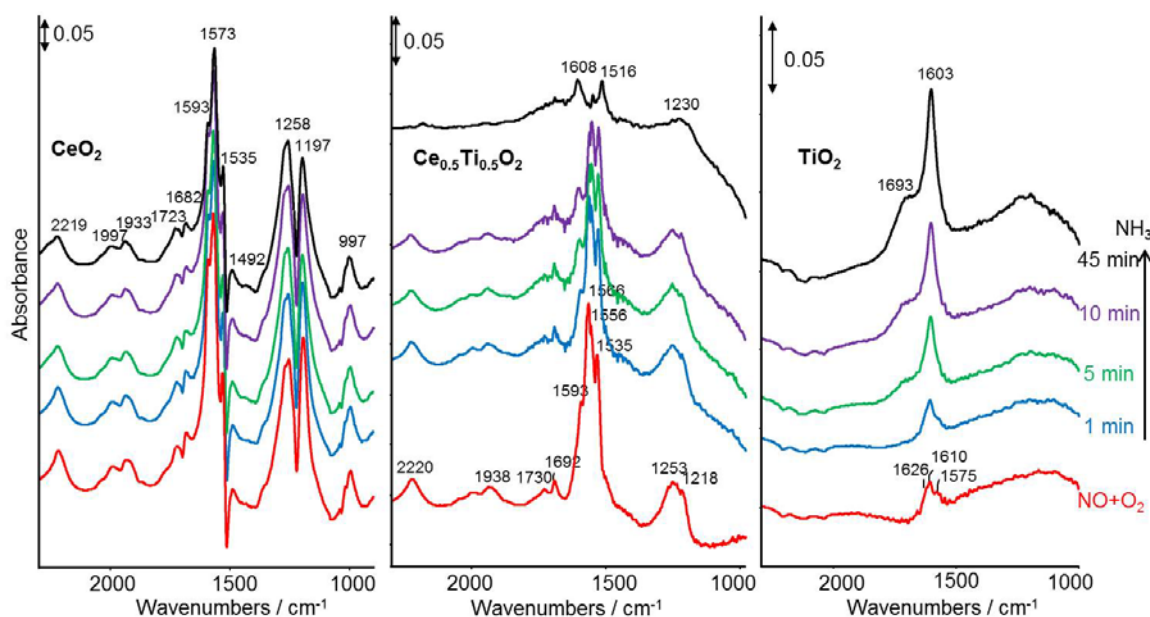


Figure 5.10: Difference DRIFT spectra recorded at 200 °C of bare supports under flowing of 0.1% NH₃/He after pretreatment at 200°C for 45 min in 0.1% NO, 5% O₂/He flow.

Comparison of all these *in-situ*-DRIFTS results points to interesting mechanistic differences in the NH₃-SCR over bare CeO₂, TiO₂ and Ce_{1-x}Ti_xO₂ supports and the corresponding V-containing catalysts. While NH₃ can be adsorbed and activated on all surfaces, NO_x species are only adsorbed on the bare supports but not on the catalysts. A possible explanation may be that Ce-O moieties responsible for oxidation and fixation of NO/O₂ as surface nitrates are covered by VO_x. This assumption suggests that NH₃-SCR proceeds after a Langmuir-Hinshelwood (L-H) mechanism over the bare supports, in which both NO and NH₃ are first adsorbed to give activated surface species that further react to produce N₂ and H₂O. To further confirm this experimentally, an additional DRIFTS experiment has been performed, in which NH₃ and NO/O₂ was subsequently adsorbed on Ce_{0.5}Ti_{0.5}O₂ at room temperature. Upon heating, the bands of adsorbed NH₃ and nitrate disappeared, and simultaneously, N₂ was detected by on-line mass spectrometry (Figure A.19). In the case of pure CeO₂ and TiO₂, the adsorbed NO_x and NH₃ species were much more stable than on the mixed Ce_{0.5}Ti_{0.5}O₂ oxide. Thus, their catalytic conversion as hindered, which explains the low activity of these solids. In contrast, an E-R mechanism might be operative in the case of the V-containing catalysts, since only NH₃ but no NO_x is adsorbed on the surface. This phenomenon means that gas-phase NO/O₂ must react with adsorbed NH₃ and NH₄⁺. This assumption is in accordance with proposals made for NH₃-SCR over pure V₂O₅,²⁴ V₂O₅/TiO₂,³³ and V₂O₅/CeO₂,⁷¹ but contradicts other studies in which a L-H mechanism is suggested for the same reaction on V₂O₅, V₂O₅/alumina,³² and V₂O₅/TiO₂.²⁰⁸

5.4. Conclusions

Incorporation of Ti into CeO_2 led to solid $\text{Ce}_{1-x}\text{Ti}_x\text{O}_2$ solutions with higher surface area, smaller crystallite size and/or higher disorder. This might improve oxygen mobility and raise catalytic activity in NH_3 -SCR already in the absence of VO_x surface species. While pure CeO_2 and TiO_2 were poorly active even at 300 °C, $\text{Ce}_{1-x}\text{Ti}_x\text{O}_2$ with $x \geq 0.3$ achieved NO and NH_3 conversions around 80% at 200 °C. Deposition of vanadia on the surface of these supports boosted SCR activity tremendously. With the best 5wt.% $\text{V}_2\text{O}_5/\text{Ce}_{1-x}\text{Ti}_x\text{O}_2$ catalysts ($x = 0.3-0.5$), NO conversion and N_2 selectivity of 100% were reached already below 200 °C at a space velocity of 70,000 h^{-1} and the performance was still appreciable at a tenfold higher space velocity of 750,000 h^{-1} . Remarkably, no undesired product N_2O was formed during NH_3 -SCR over these catalysts.

Comprehensive studies of structure-reactivity relationships using *in-situ* and *operando* spectroscopy revealed significant mechanistic differences. While on bare supports NH_3 -SCR proceeds after a L-H mechanism implying the reaction between adsorbed NH_3 and nitrate species (formed on the surface by reaction of NO/O_2), an E-R mechanism is operating in the case of V-containing catalysts, in which adsorbed NH_3 and NH_4^+ react with NO/O_2 from the gas phase.

The switch in reaction mechanism has its roots in structural differences of catalysts and supports. While NH_3 adsorbs on both Lewis and Brønsted sites present in all samples (though to a different extent), nitrate is preferentially formed from NO/O_2 by the participation of Ce-O moieties. Within the bare supports, the observed maximum catalytic activity of $\text{Ce}_{1-x}\text{Ti}_x\text{O}_2$ ($x = 0.3-0.5$) can be explained by the high reactivity of surface nitrates. On the Ti-free CeO_2 support, nitrates, despite being abundant, are poorly reactive. In $\text{V}/\text{Ce}_{1-x}\text{Ti}_x\text{O}_2$ catalysts, Ce-O sites are obviously effectively covered by VO_x species which hinders the formation of surface nitrates and causes the switch in the reaction mechanism.

Without a doubt, both Lewis and Brønsted surface sites support NH_3 adsorption, yet the difference in their concentration does not correlate with the observed activity differences. This suggests that it is the redox properties of the materials that mostly govern catalytic activity, i. e. the intrinsic oxygen mobility of the supports is boosted by replacing Ce by redox-active Ti cations. Moreover, the nature of the VO_x species in the $\text{V}/\text{Ce}_{1-x}\text{Ti}_x\text{O}_2$ catalysts differs as well. V/TiO_2 and, to a lesser extent, also V/CeO_2 contain lower dispersed VO_x species up to amorphous surface aggregates and even V_2O_5 nanoparticles, not all V sites of which might be accessible by reactant molecules. In contrast, a unique property of the most active $\text{V}/\text{Ce}_{0.5}\text{Ti}_{0.5}\text{O}_2$ catalyst is the presence of highly dispersed vanadyl species connected via oxygen bridges to both Ce and Ti. These are highly redox-active. Apparently, the intimate

contact with Ce/Ti renders the V species in their highest and most active equilibrium valence state +5. In a Mars-van Krevelen mechanism, which is commonly accepted for $\text{NH}_3\text{-SCR}$,^{6, 22, 26, 118} and also supported by the results of *in-situ* spectroscopy in this work, oxygen vacancies created upon reduction of V^{5+} by NH_3 in the immediate vicinity of the resulting V^{4+} must be replenished during reoxidation of the latter. Possibly this does not happen directly by gas-phase O_2 in the very same position but by a lattice oxygen in the immediate vicinity, whereby other vacancies at higher distances are created, which are then filled by gas-phase oxygen (Figure 5.11). This assumption would mean that supply and uptake of oxygen according to Mars-van Krevelen are not restricted to the outermost surface but also comprises deeper layers of the catalyst lattice. In such a case, a high efficiency of oxygen and electron transport through the catalysts lattice, being a specialty of ceria-based oxides, might boost the reaction rate.

In previous studies of vanadium phosphate catalysts during selective oxidation of hydrocarbons which also follow a Mars-van Krevelen mechanism, it has been experimentally verified by *in-situ*-EPR that the catalyst bulk did indeed participate in oxygen transport.²⁰⁹ Therefore, these findings strongly suggest that it is the efficiency of this process which is responsible for the catalytic performance of $\text{V/Ce}_{1-x}\text{Ti}_x\text{O}_2$ ($x = 0.3\text{-}0.5$) catalysts. Apart from this, a high steady-state concentration of V^{5+} maintained under SCR conditions in the best catalysts might improve Lewis acidity and, thus, NH_3 adsorption.

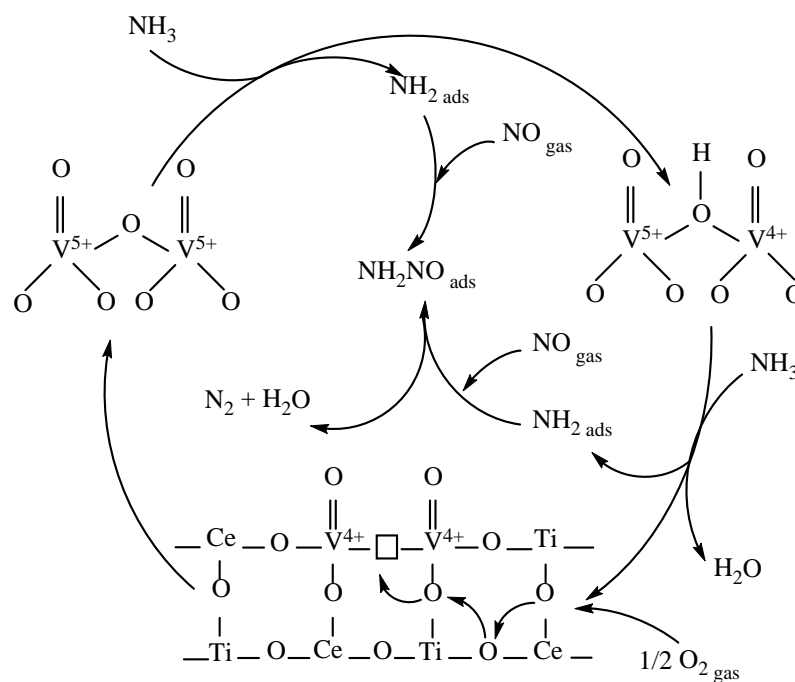


Figure 5.11: Schematic illustration of the tentative mechanism of low-temperature $\text{NH}_3\text{-SCR}$ on $\text{V/Ce}_{1-x}\text{Ti}_x\text{O}_2$ catalysts.

6. $\text{V}_2\text{O}_5/\text{Ce}_{0.5}\text{Ti}_{0.5-x}\text{Mn}_x\text{O}_{2-\delta}$ catalysts

As mentioned above, Mn-based oxides are among the most active catalysts for NH_3 -SCR at low temperatures even below 150 °C. Unfortunately, undesired N_2O formation and poor resistance to SO_2 and H_2O is a big disadvantage of these catalysts. Therefore, significant efforts have been made to solve these limitations, e. g. by mixing MnO_x with other oxides. Several binary oxides including Ce-Mn,^{210, 15} Mn-Zr,⁶⁶ Mn-Ni,⁶⁷ and ternary compositions such as Mn-Ce-Ti⁵⁷ and Sn-Mn-Ce⁵⁶ have been tested, yet with different success.

In chapter 5 it has been shown that 5% $\text{V}_2\text{O}_5/\text{Ce}_{0.5}\text{Ti}_{0.5}\text{O}_2$ belongs to the most active and selective catalysts known so far for low-temperature NH_3 -SCR of NO_x . Therefore, the aim of this chapter is to enhance even more the low-temperature activity of this catalyst while keeping its N_2 selectivity as high as possible by modifying it with manganese. Thus, the impact of different amounts of Mn on the catalytic performance and structure of $\text{Ce}_{0.5}\text{Ti}_{0.5-x}\text{Mn}_x\text{O}_{2-\delta}$ supports and the corresponding V-containing catalysts has been analysed.

6.1. Catalytic behaviour of $\text{Ce}_{0.5}\text{Ti}_{0.5-x}\text{Mn}_x\text{O}_{2-\delta}$ in the presence and absence of V

Figure 6.1 illustrates NH_3 -SCR performances of all supports without vanadium $\text{Ce}_{0.5}\text{Ti}_{0.5-x}\text{Mn}_x\text{O}_{2-\delta}$ ($x = 0-0.2$) and the respective $\text{V}/\text{Ce}_{0.5}\text{Ti}_{0.5-x}\text{Mn}_x\text{O}_{2-\delta}$ catalysts. The NO conversion of the bare supports increased with rising Mn already well below 200 °C (Figure 6.1A). Compared to the $\text{Ce}_{0.5}\text{Ti}_{0.5}\text{O}_2$ support, the sample with the smallest amount of Mn ($\text{Ce}_{0.5}\text{Ti}_{0.49}\text{Mn}_{0.01}\text{O}_{2-\delta}$) exhibited only a slight improvement. In contrast, after incorporating the maximum amount of Mn into $\text{Ce}_{0.5}\text{Ti}_{0.5}\text{O}_2$, the NO conversion increased markedly at low temperatures, however, decreased significantly in the higher temperature region. This is due to the oxidation of NH_3 to N_2 , N_2O , or NO which raised the NH_3 conversion beyond that of NO and lowered the N_2 selectivity over this sample (Figure 6.1C and 6.1E). With a lower amount of Mn in $\text{Ce}_{0.5}\text{Ti}_{0.45}\text{Mn}_{0.05}\text{O}_{2-\delta}$ and $\text{Ce}_{0.5}\text{Ti}_{0.49}\text{Mn}_{0.01}\text{O}_{2-\delta}$ samples, the catalytic performance was improved markedly in the whole range of temperature compared to $\text{Ce}_{0.5}\text{Ti}_{0.5}\text{O}_2$, and both NO and NH_3 conversion could be maintained above 85% from 175 to 300 °C, while N_2 selectivity remained 95% until 300 °C.

Compared to the bare supports, the effect of Mn addition was much weaker for the V-containing catalysts. Samples $\text{V}/\text{Ce}_{0.5}\text{Ti}_{0.49}\text{Mn}_{0.01}\text{O}_{2-\delta}$ and $\text{V}/\text{Ce}_{0.5}\text{Ti}_{0.45}\text{Mn}_{0.05}\text{O}_{2-\delta}$ did not show any improvement of the catalytic performance compared to $\text{V}/\text{Ce}_{0.5}\text{Ti}_{0.5}\text{O}_2$ (Figure 6.1B, D and E). Moreover, in comparison to the bare supports $\text{Ce}_{0.5}\text{Ti}_{0.49}\text{Mn}_{0.01}\text{O}_{2-\delta}$ and $\text{Ce}_{0.5}\text{Ti}_{0.45}\text{Mn}_{0.05}\text{O}_{2-\delta}$ the conversion even seems to drop

slightly. A weak increase in NO and NH₃ conversion below 175 °C was observed for catalysts V/Ce_{0.5}Ti_{0.4}Mn_{0.1}O_{2-δ} in comparison to V/Ce_{0.5}Ti_{0.5}O₂ while this effect was significant for catalysts V/Ce_{0.5}Ti_{0.3}Mn_{0.2}O_{2-δ} (Figure 6.1B and D). Remarkably, the N₂ selectivity of the latter still remained above 94% in the whole range of temperature while it dropped drastically above 200 °C for the bare Ce_{0.5}Ti_{0.3}Mn_{0.2}O_{2-δ} support (Figure 6.1E). These results show that deposition of vanadium leads to an enhancement of the NH₃-SCR activity and simultaneously to a higher N₂ selectivity over Ce_{0.5}Ti_{0.5-x}Mn_xO_{2-δ} supports with x = 0.1-0.2.

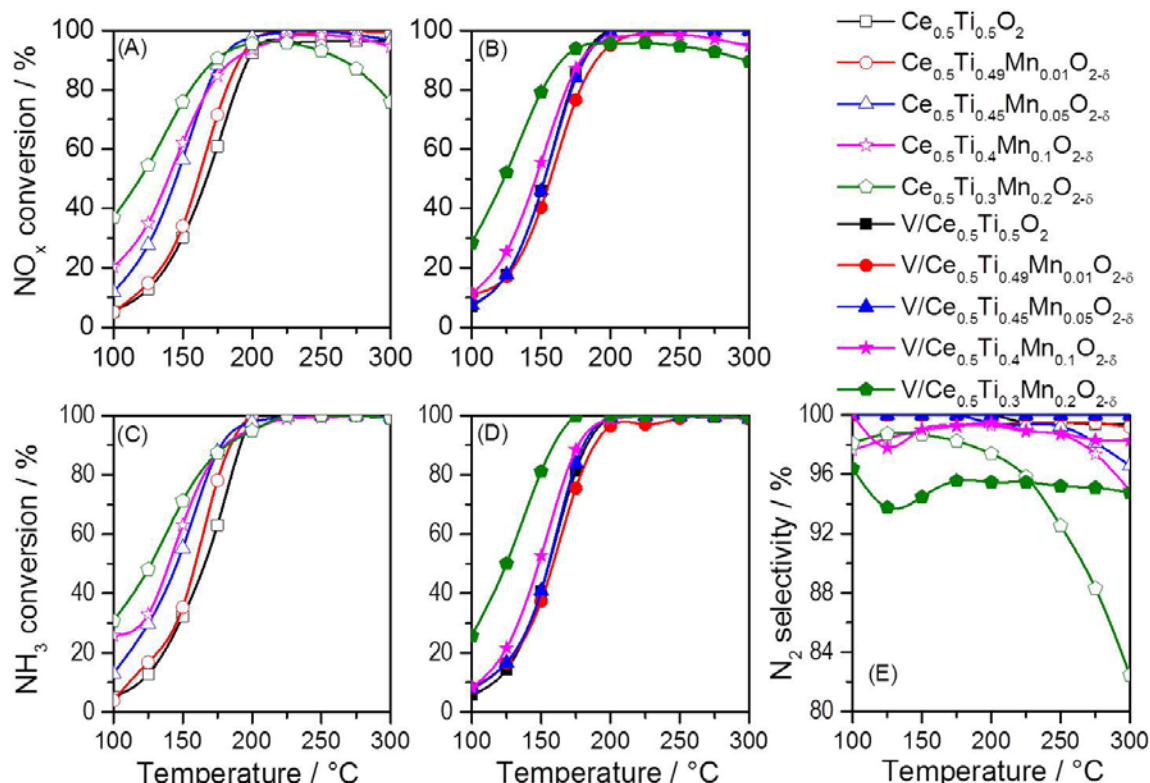


Figure 6.1: NO conversion (A and B), NH₃ conversion (C and D), and N₂O concentration (E) over pure Ce_{0.5}Ti_{0.5-x}Mn_xO_{2-δ} (x = 0-0.2) supports (open symbols) and respective V/Ce_{0.5}Ti_{0.5-x}Mn_xO_{2-δ} catalysts (filled symbols) as a function of temperature. Feed composition: 0.1% NO, 0.1% NH₃, 5% O₂/He, GHSV = 70,000 h⁻¹.

6.2. Structure-reactivity relationships and active sites

6.2.1. Catalyst characterization

XRD analysis was performed to identify the crystal structure of all prepared supports and V-based catalysts. As seen in Figure A.20A, the support Ce_{0.5}Ti_{0.5}O₂ obeyed a cubic fluorite structure of CeO₂ without any peaks of TiO₂, indicating the replacement of Ce⁴⁺ (97 pm) by smaller Ti⁴⁺ ions (74 pm) to form a homogeneous solid solution. A similar structure has been observed in the previous study of

V/Ce_{1-x}Ti_xO₂ catalysts in chapter 5, in which, however, the Ce_{0.5}Ti_{0.5}O₂ support was prepared by a co-precipitation method. This structure still remained in the Mn-containing supports, yet all reflections became broader with rising Mn content. This is due to the incorporation of smaller Mnⁿ⁺ ions (Mn²⁺ = 83 pm, Mn³⁺ = 58 pm, Mn⁴⁺ = 53 pm)²¹¹ into the CeO₂ cubic fluorite structure resulting in a decrease in the crystallite size of ternary oxide compared to binary oxide (Table 6.1). Also, besides those peaks assigned to CeO₂, some minor additional peaks of Ce₂O₃ phase (2θ = 32.9°, 45.3°) and Mn₂O₃ phase (2θ = 30.8, 34.3°, 49.4°, 55.2°, and 65.8°)²¹² were found in the sample with the highest amount of Mn (Ce_{0.5}Ti_{0.3}Mn_{0.2}O_{2-δ}), pointing to heterogeneity of this sample. After impregnation with vanadia, all XRD patterns (Figure A.20B) remained unchanged, and no crystalline phase ascribed to V₂O₅ can be found. This points to highly dispersed and/or amorphous vanadium oxide species on the surface of the supports.

As shown in Table 6.1, no big differences in specific surface area and pore volume of supports were observed. Among all the supports prepared, Ce_{0.5}Ti_{0.4}Mn_{0.1}O_{2-δ} achieved the highest surface area (182.8 m².g⁻¹) while incorporating Mn into Ce_{0.5}Ti_{0.5}O₂ led to a slight increase of pore size of supports. However, the pore size distribution suggests that all samples predominantly contain mesopores.

Table 6.1: Crystallite size, specific surface area and pore volume, band gap energy of supports and catalysts.

Sample	Mean crystallite size (nm) ^[a]	Surface area (m ² g ⁻¹)	Pore volume (cm ³ g ⁻¹)	Average pore size (nm)	Band gap energy (eV) ^[b]
Ce _{0.5} Ti _{0.5} O ₂	8.5	169.9	0.45	7.58	2.79
Ce _{0.5} Ti _{0.49} Mn _{0.01} O _{2-δ}	9.7	148.1	0.36	8.50	2.80
Ce _{0.5} Ti _{0.45} Mn _{0.05} O _{2-δ}	7.4	140.7	0.43	9.05	2.73
Ce _{0.5} Ti _{0.4} Mn _{0.1} O _{2-δ}	6.8	182.8	0.46	10.71	2.71
Ce _{0.5} Ti _{0.3} Mn _{0.2} O _{2-δ}	5.2	147.9	0.51	11.10	2.64
V/Ce _{0.5} Ti _{0.5} O ₂	9.0	143.6	0.35	7.18	2.65
V/Ce _{0.5} Ti _{0.49} Mn _{0.01} O _{2-δ}	9.7	146.8	0.33	8.00	2.66
V/Ce _{0.5} Ti _{0.45} Mn _{0.05} O _{2-δ}	7.4	126.6	0.38	8.99	2.61
V/Ce _{0.5} Ti _{0.4} Mn _{0.1} O _{2-δ}	5.7	168.9	0.43	10.45	2.60
V/Ce _{0.5} Ti _{0.3} Mn _{0.2} O _{2-δ}	4.2 ± 0.5	143.8	0.48	10.05	2.55

^a derived by the Scherrer E.q. from XRD data, ^b results from UV-Vis

The N₂ adsorption-desorption isotherms of both V-free supports and supported vanadium catalyst display typical type IV isotherms with hysteresis loops, which are associated with mesoporous materials (Figure 6.2). Depositing vanadium oxide resulted in a slight decrease of the BET surface area, but nearly no change in the pore size of respective supports, suggesting that the introduction of vanadium species did not include any significant modification of the support structure.

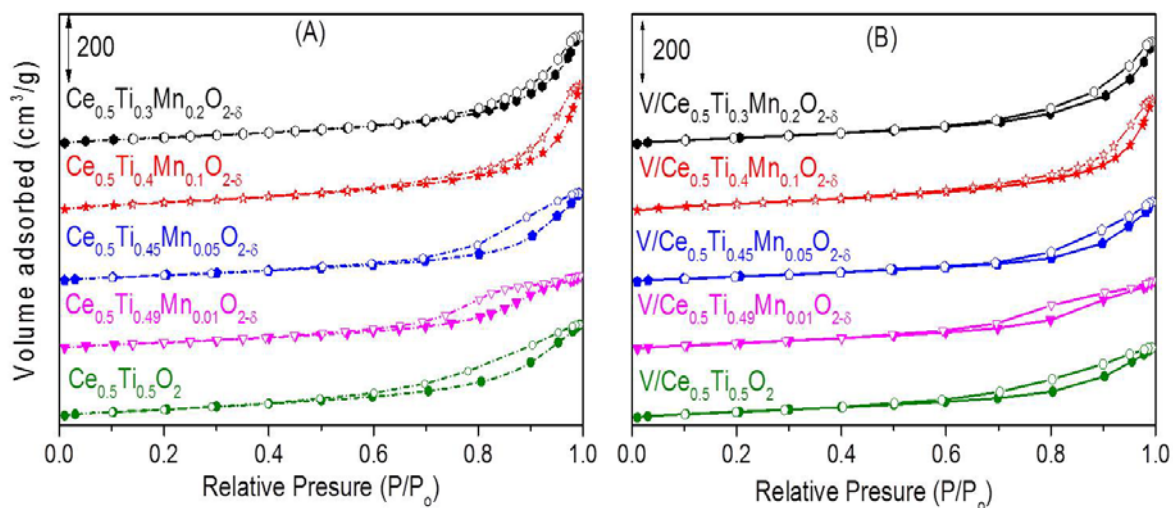


Figure 6.2: N₂ adsorption (filled symbols) and desorption isotherms (open symbols) of pure supports (A) and supported vanadium catalysts (B).

Raman spectroscopy was also employed for the structural analysis since Raman spectra are capable of identifying small amounts of crystalline and amorphous phases with higher sensitivity than XRD. As illustrated in Figure 6.3, all samples exhibited a sharp peak at 463 cm⁻¹ ascribed to the triply degenerate F_{2g} mode of cubic fluorite ceria.^{187, 213} The F_{2g} mode is very sensitive to the disorder in the oxygen sublattice. Therefore, the broadening and decreasing intensity of this band with increasing Mn content might be related to the lower crystallinity of the cubic fluorite structure and smaller crystallite size after co-incorporating Ti and Mn into this structure, or/and an increase in the number of oxygen vacancies. Beside the F_{2g} mode, a weak peak at 281 cm⁻¹ and a small shoulder at 599 cm⁻¹ are related to contributions of vacant sites in ceria lattice. The shoulder at 281 cm⁻¹ is assigned to the partial breaking of the Raman-active oscillation mode of the ceria fluorite structure. This shoulder red shifted to 255 cm⁻¹ for the sample Ce_{0.5}Ti_{0.3}Mn_{0.2}O_{2-δ} (Figure 6.3A). This shift is related to the higher lattice distortions of Ce_{0.5}Ti_{0.3}Mn_{0.2}O_{2-δ},²¹⁴ which agrees with its smallest crystallite size in Table 6.1. Moreover, a broad and weak band at 704 cm⁻¹ decreased in intensity with decreasing Ti content. This vibrational mode can be assigned to seven-coordinate Ti atoms in a fluorite structure indicating the formation of a solid solution Ce_{0.5}Ti_{0.5}O₂.²¹⁵⁻²¹⁶ The absence of this band in the sample Ce_{0.5}Ti_{0.3}Mn_{0.2}O_{2-δ} might

be due to the lowest Ti content. Although Mn_2O_3 is found in the support with the highest amount of Mn ($\text{Ce}_{0.5}\text{Ti}_{0.3}\text{Mn}_{0.2}\text{O}_{2-\delta}$) by XRD analysis (Figure A.20A), no peaks of pure MnO , Mn_2O_3 , and MnO_2 were detected by Raman spectroscopy since these oxides show only weak Raman bands. After impregnation with vanadia, all supports maintained their original structures and no Raman bands of crystalline V_2O_5 could be found. Moreover, in the case of V-based catalysts, the symmetric $\text{V}=\text{O}$ stretching vibration at $1014\text{--}1024\text{ cm}^{-1}$ was seen. The frequencies of the $\text{V}=\text{O}$ stretches at 1008 , 1015 , $1022\text{--}1030$ and 1044 cm^{-1} was assigned to monomeric, dimeric, trimeric, and polymeric VO_x , respectively.^{94, 107} Therefore, here, the $\text{V}=\text{O}$ stretches related to surface VO_4 oligomer species. These Raman results agree with the XRD and BET measurements which indicate that the incorporation of titanium and manganese into ceria maintained the cubic fluorite structure of ceria with high surface area leading to finely dispersed vanadium oxide on the surface of these supports.

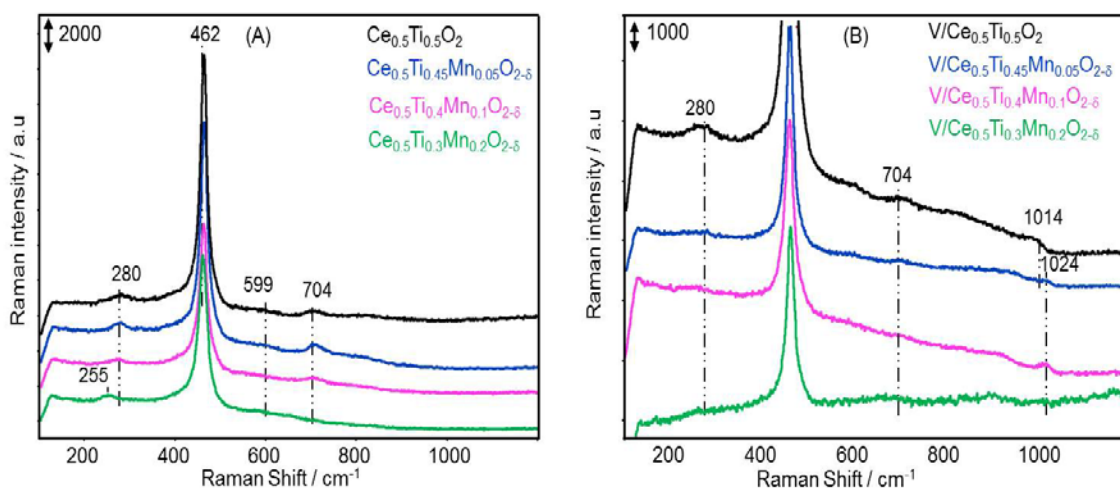


Figure 6.3: The Raman spectra of $\text{Ce}_{0.5}\text{Ti}_{0.5-x}\text{Mn}_x\text{O}_{2-\delta}$ ($x = 0\text{--}0.2$) supports (A) and $\text{V}/\text{Ce}_{0.5}\text{Ti}_{0.5-x}\text{Mn}_x\text{O}_{2-\delta}$ catalysts (B).

The UV-Vis spectra of $\text{Ce}_{0.5}\text{Ti}_{0.5-x}\text{Mn}_x\text{O}_{2-\delta}$ supports and $\text{V}/\text{Ce}_{0.5}\text{Ti}_{0.5-x}\text{Mn}_x\text{O}_{2-\delta}$ ($x = 0\text{--}0.2$) are depicted in Figure 6.4, and the band gap energies (E_g) derived from them are summarised in Table 6.1. These energies were estimated using the Kubelka-Munk formula and Tauc plot in Figure A.21.

As illustrated in Figure 6.4, the absorption band below 400 nm in the sample $\text{Ce}_{0.5}\text{Ti}_{0.5}\text{O}_2$ is superimposed by charge-transfer transitions of Ce^{4+} and Ti^{4+} . Incorporation of Mn into $\text{Ce}_{0.5}\text{Ti}_{0.5}\text{O}_2$ led to an increase in the intensity of the absorption band below 400 nm . This result indicates the presence of Mn^{2+} and Mn^{3+} in these supports since the bands at 220 , 260 and 325 nm are assigned to $\text{O}^{2-} \rightarrow \text{Mn}^{2+}$ and $\text{O}^{2-} \rightarrow \text{Mn}^{3+}$ charge transfer transitions, respectively.²¹⁷ Additional broad bands above 450 nm , which increased in intensity with the amount of Mn, may be

attributed to crystal field d-d transitions of octahedral Mn^{3+} species.²¹⁷⁻²¹⁸ The E_g values of all Mn-containing supports shifted to lower energies (red shift) compared with those of $\text{Ce}_{1-x}\text{Ti}_x\text{O}_2$. Since the absorption signal of surface vanadium species overlaps with that of the $\text{Ce}_{0.5}\text{Ti}_{0.5-x}\text{Mn}_x\text{O}_{2-\delta}$ supports, it is not possible to determine the structure of vanadium species in the V-containing catalysts. As mentioned in Chapter 5, however, the edge energy derived from UV-Vis-DRS is a measure of the degree of VO_x agglomeration. Increasing loading with vanadium led to smaller E_g values in all $\text{V}/\text{Ce}_{0.5}\text{Ti}_{0.5-x}\text{Mn}_x\text{O}_{2-\delta}$ catalysts (Table 6.1). E_g values of 2.55-2.65 eV point to highly polymerised amorphous surface vanadium oxide species on these catalysts. This assumption agrees well with Raman results with no V_2O_5 crystallite bands discussed above.

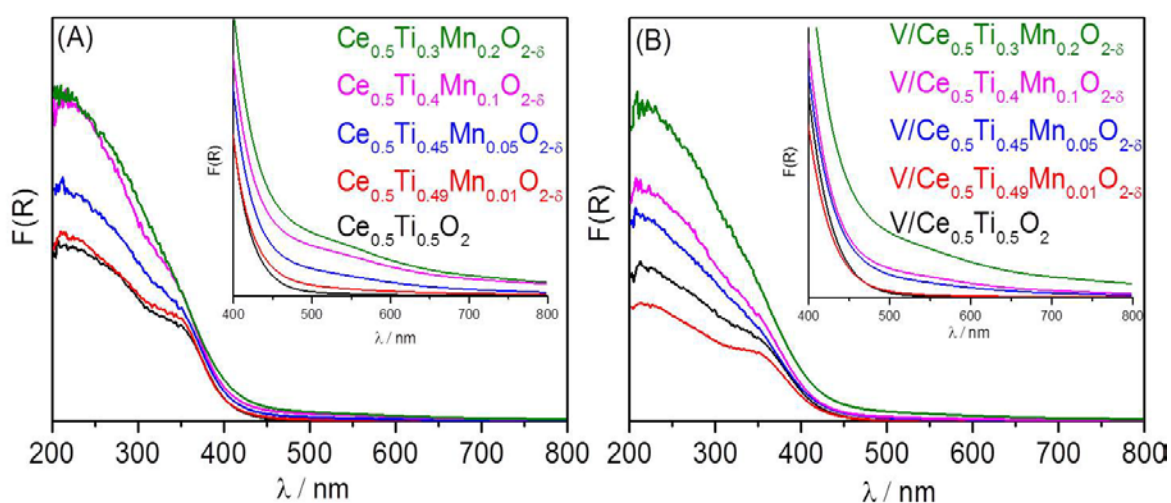


Figure 6.4: UV-Vis-DR spectra of pure supports $\text{Ce}_{0.5}\text{Ti}_{0.5-x}\text{Mn}_x\text{O}_{2-\delta}$ ($x = 0-0.2$) (A) and $\text{V}/\text{Ce}_{0.5}\text{Ti}_{0.5-x}\text{Mn}_x\text{O}_{2-\delta}$ catalysts (B) recorded at room temperature using BaSO_4 as baseline.

Figure 6.5 depicts EPR spectra of $\text{V}/\text{Ce}_{0.5}\text{Ti}_{0.5-x}\text{Mn}_x\text{O}_{2-\delta}$ catalysts together with those of the vanadium-free support. For the samples without manganese, the weak signal from oxygen species such as O^\bullet and/or O_2^\bullet was observed in the range of $g = 2.058-1.997$.^{190, 219} Besides oxygen species, the rhombic signal at $g_x = 1.976$; $g_y = 1.963$; $g_z = 1.942$ can be assigned to Ti^{3+} in the support lattice. This line lost intensity and changed to axial symmetry ($g_\perp = 1.963$, $g_\parallel = 1.942$)²²⁰ after depositing vanadium. The EPR spectra of $\text{V}/\text{Ce}_{0.5}\text{Ti}_{0.5}\text{O}_2$ contained an additional weak isotropic signal at $g = 1.993$ that may be related to Ti^{3+} on the surface of this sample.²²¹ Moreover, no VO^{2+} signal was seen in the EPR spectra of this catalyst indicating the presence of only pentavalent V^{5+} . The Mn-containing samples shown a set of six narrow lines with $g = 2.004$ and a hyperfine structure splitting (hfs) constant of $A = 90$ G, arising from Mn^{2+} single sites substituting for Ce^{4+} ions in octahedral sites in the cubic crystal lattice.²²² In addition to these resolved spectral features, the broad background signal around $g = 2$, which is superimposed on the hfs sextet, increases

in intensity with rising amount of Mn. This is due to magnetically interacting Mn^{2+} species located at the interstitial positions or at the surface and/or within clusters.²²²⁻²²⁴ The EPR signal is characteristic for Mn^{2+} only. A possible signal of Mn^{4+} would occur at lower $g = 1.994$ and with lower $A = 76\text{G}$, while Mn^{3+} ions can be detected at very low temperatures and high frequencies only.²²² Therefore, reduction and reoxidation experiments were performed by *in-situ*-EPR to prove the behaviour of Mn^{2+} ions in supports and catalysts.

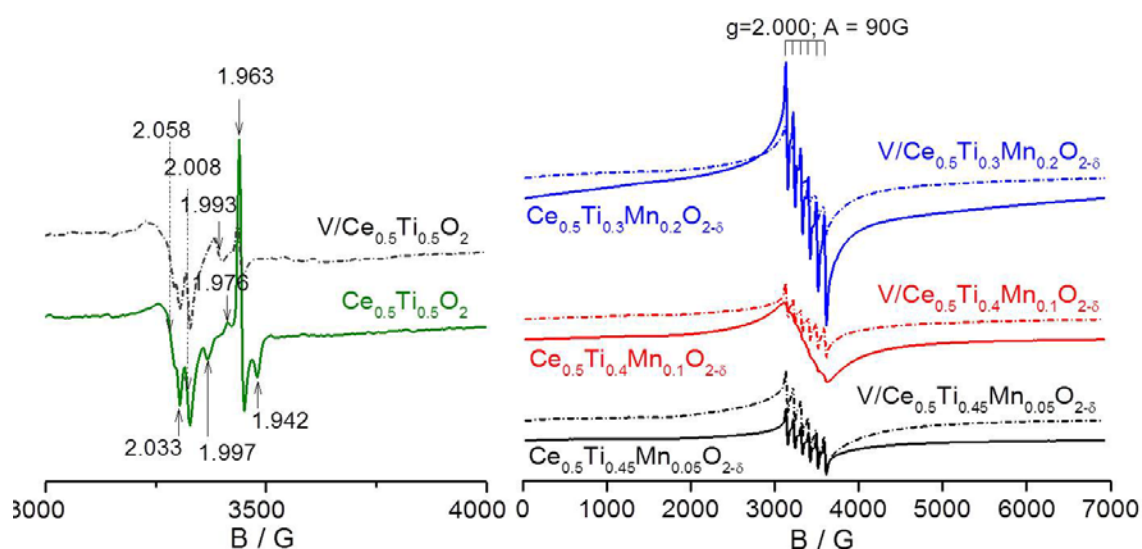


Figure 6.5: The EPR spectra of $\text{Ce}_{0.5}\text{Ti}_{0.5}\text{O}_2$ and $\text{V/Ce}_{0.5}\text{Ti}_{0.5}\text{O}_2$ recorded at 20 °C (left) and that of Mn-containing supports and V-loaded catalysts recorded at 200 °C (right).

6.2.2. *In-situ* investigation of active sites

In-situ-DRIFTS investigations

In-situ-DRIFT spectra of NH_3 adsorbed on the bare supports and the V-containing catalysts contain bands at $3376\text{--}3150\text{ cm}^{-1}$ arising from $\nu(\text{N-H})$ stretching vibrations of NH_3 coordinated to Lewis acid sites (Figure A.22).^{30, 33} The corresponding symmetric and asymmetric bending vibrations appear at $1233\text{--}1176$ and 1603 cm^{-1} (Figure 6.6).^{30, 33, 202} On Brønsted sites, NH_3 is protonated, and the symmetric and asymmetric modes of NH_4^+ are seen at $1668\text{--}1664\text{ cm}^{-1}$ and $1434\text{--}1410\text{ cm}^{-1}$, respectively. The presence of surface hydroxyl groups is also supported by the negative bands of the O-H stretching at about 3740 and 3648 cm^{-1} in Figure A.22. Compared to the bare supports, the intensities of these bands in the corresponding supported vanadia catalysts are significantly higher indicating a higher amount of Brønsted acid sites on these catalysts. This is explained by the presence of V-OH groups on the surface of V-containing catalysts. However, the activity of $\text{Ce}_{0.5}\text{Ti}_{0.4}\text{Mn}_{0.1}\text{O}_{2-\delta}$ was even slightly higher than that of the catalyst $\text{V/Ce}_{0.5}\text{Ti}_{0.4}\text{Mn}_{0.1}\text{O}_{2-\delta}$ at temperatures below 175 °C (Figure 6.1). Therefore, the

Brønsted acid sites might not play a major role in NH_3 -SCR of NO_x over these catalysts. A similar assumption was observed for Mn-free samples discussed in section 5.3, pages 63-64.

For the supported vanadia catalysts, additional negative bands at $2046\text{-}2044\text{ cm}^{-1}$ were also observed. These bands can be assigned to the 2ν overtone of the $\text{V}^{5+}=\text{O}$ stretching mode of surface vanadyl groups which are partly reduced to $\text{V}^{4+}=\text{O}$ and/or covered by NH_3 .^{33, 114}

After $\text{NO} + \text{O}_2$ had been introduced, the intensity of the bands related to coordinated NH_3 decreased and disappeared after 10 min in the case of bare supports, while new groups appeared simultaneously and increased with an increase of the exposure time in $\text{NO}+\text{O}_2$, suggesting that adsorbed NH_3 species react with $\text{NO} + \text{O}_2$. Bands below 1600 cm^{-1} are due to monodentate (1536 and $1243\text{-}1241\text{ cm}^{-1}$), bridged ($1625\text{-}1592$ and 1205 cm^{-1}) and bidentate nitrate species ($1579\text{-}1572$ and $1227\text{-}1210\text{ cm}^{-1}$), while some weak shoulders between $1516\text{-}1390\text{ cm}^{-1}$ can be assigned to chelating nitro compounds.^{136, 203-204, 225} The weak features between 2200 and 1900 cm^{-1} may stem from combination bands of adsorbed NO_x species.²⁰⁵⁻²⁰⁶ Additionally, bands at $1995\text{-}1925\text{ cm}^{-1}$ of M-NO mononitrosyl species (M= Ce, Ti, Mn), adsorbed NO_2 (1691 cm^{-1}) and N_2O_4 ($1732\text{-}1729\text{ cm}^{-1}$) were observed.^{136, 225} Besides, a broad band at 2220 cm^{-1} can be attributed to adsorbed NO^+ cations.^{136,207} The faster disappearance of coordinated NH_3 over the Mn-containing supports corresponds to better NH_3 -SCR activity of these samples compared to $\text{Ce}_{0.5}\text{Ti}_{0.5}\text{O}_2$ support. When the exposure time of $\text{NO}+\text{O}_2$ after NH_3 pretreatment reached 45 min, the DRIFT spectra were similar to those of the corresponding supports after 45 min exclusive exposure to $\text{NO}+\text{O}_2$ without pretreatment in NH_3 (top traces in Figure 6.6A). In comparison to the $\text{Ce}_{0.5}\text{Ti}_{0.5}\text{O}_2$ support, higher band intensity of nitrate species points to more of these adsorbed species on the surface of $\text{Ce}_{0.5}\text{Ti}_{0.4}\text{Mn}_{0.1}\text{O}_{2-\delta}$ and $\text{Ce}_{0.5}\text{Ti}_{0.3}\text{Mn}_{0.2}\text{O}_{2-\delta}$ supports. Moreover, in Mn-containing supports, the bands of nitrates species slightly shifted to the higher wavenumbers. This is probably due to the higher mobility of lattice oxygen nearby Mn^{n+} which supports the oxidation of NO to nitrite and subsequently to nitrate.²²⁶ It is well known that nitrate species are the most reactive species for NH_3 -SCR.²²⁷ Therefore, the higher amount of these species agrees well with the higher NH_3 -SCR activity of Mn-containing supports.

The same behaviour was observed for the supported vanadia catalysts $\text{V}/\text{Ce}_{0.5}\text{Ti}_{0.4}\text{Mn}_{0.1}\text{O}_{2-\delta}$ and $\text{V}/\text{Ce}_{0.5}\text{Ti}_{0.3}\text{Mn}_{0.2}\text{O}_{2-\delta}$, in which the intensities of both coordinated NH_3 on Lewis acid sites and NH_4^+ on Brønsted acid sites decreased and disappeared gradually after 10 min exposure to 0.1% NO , 5% O_2/He (Figure 6.6B). Meanwhile, some new bands attributed to monodentate nitrates (1549 cm^{-1}), bridged nitrates (1599 and 1205 cm^{-1}) and bidentate nitrates (1576 and

1232 cm^{-1}) appeared.^{136, 203-204, 225} Remarkably, on the Mn-free catalyst $\text{V/Ce}_{0.5}\text{Ti}_{0.5}\text{O}_2$, adsorbed NH_3 species on Lewis acid sites were more stable. Moreover, no adsorbed nitrates, nitrosyl, and NO^+ ions were formed (Figure 6.6B). These results indicate that the formation of adsorbed nitrates and NO_x species on $\text{V/Ce}_{0.5}\text{Ti}_{0.4}\text{Mn}_{0.1}\text{O}_{2-\delta}$ and $\text{V/Ce}_{0.5}\text{Ti}_{0.3}\text{Mn}_{0.2}\text{O}_{2-\delta}$ catalysts might be related to Mn species. Furthermore, the participation of the vanadium sites in NH_3 -SCR is clearly evident from the decrease of the intensities of the negative $2\nu(\text{V}=\text{O})$ and at 2046-2044 cm^{-1} (Figure 6.7B), which is related to the reoxidation of V^{4+} to $\text{V}^{5+}=\text{O}$. This phenomenon was found previously for $\text{V/Ce}_{1-x}\text{Ti}_x\text{O}_2$ catalysts in section 5.3, page 63, too.

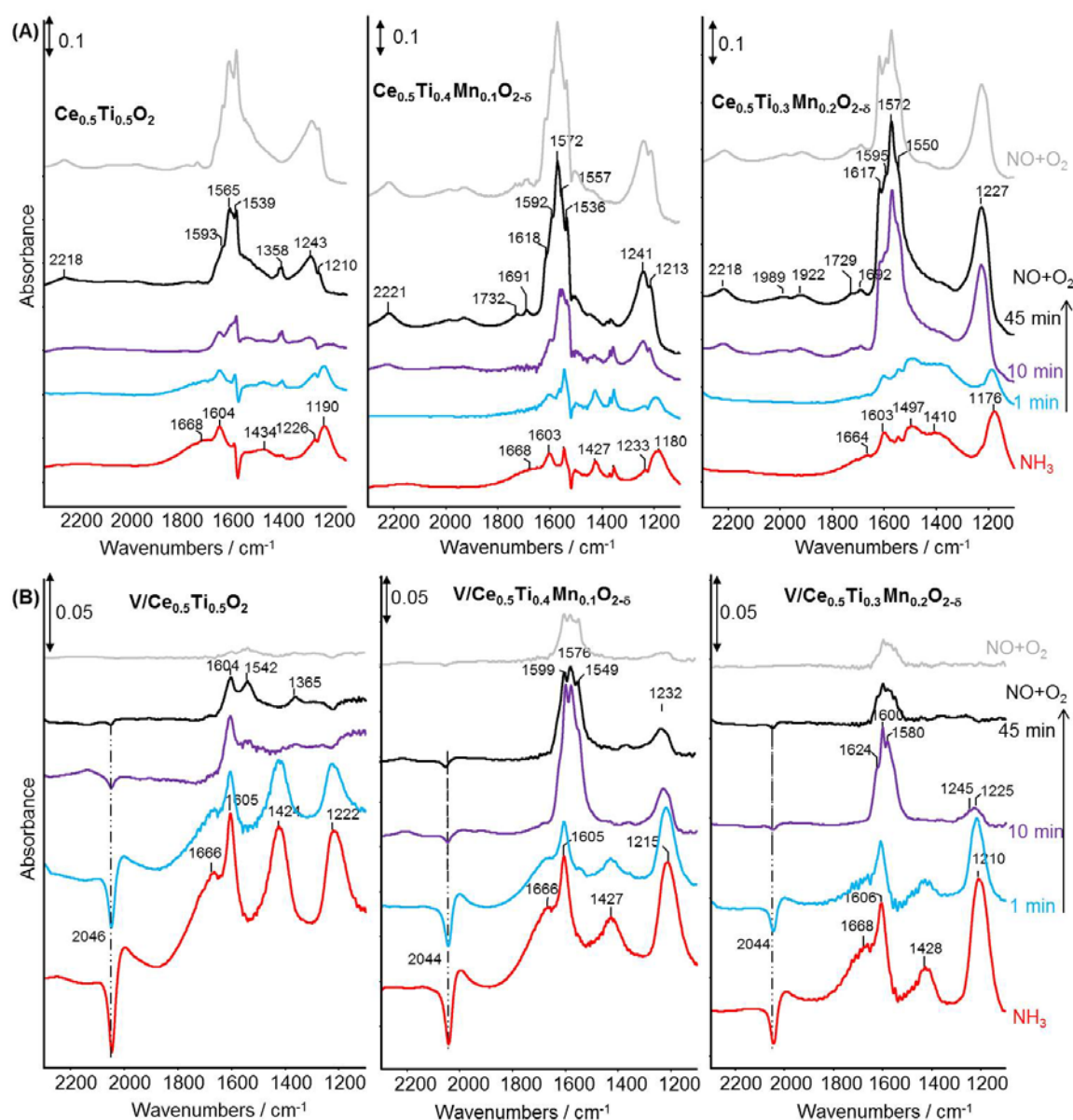


Figure 6.6: Difference DRIFT spectra recorded at 175 °C of bare supports (A) and V-containing catalysts (B) after 45 min exposure at 175 °C to 0.1% NH_3/He flow followed by purging in He for 30 min and subsequent switch to 0.1% NO , 5% O_2/He flow. Top traces depict spectra recorded after 45 min exclusive exposure to 0.1% NO , 5% O_2/He flow without pretreatment in NH_3/He .

In separate experiments, bare supports and catalysts were first exposed to 0.1% NO, 5% O₂/He flow for 45 min followed by purging in He for another 30 min and subsequently to 0.1% NH₃/He flow (Figure 6.7). After exposure to NO + O₂, on the bare supports, the same bands appeared as observed already after first exposing to NH₃/He and afterwards to NO + O₂ flow (compare grey and black spectra in Figure 6.6A), confirming the formation of differently bound nitrates, M-NO (M= Ce, Ti, Mn) and NO⁺ species on Ce_{0.5}Ti_{0.5-x}Mn_xO_{2-δ}. On Ce_{0.5}Ti_{0.5}O₂, the amount of adsorbed nitrates was slightly lower compared to Ce_{0.5}Ti_{0.4}Mn_{0.1}O_{2-δ} and Ce_{0.5}Ti_{0.3}Mn_{0.2}O_{2-δ}. This suggests that nitrate formation from NO/O₂ might be promoted by the higher oxygen mobility and oxidation activity of Mn-containing supports. Moreover, it indicates that it may be preferentially the oxygen in the vicinity of Mn that participates in bridged and bidentate nitrate formation since the amount of these adsorbates is somewhat higher on Mn-containing supports compared to Ce_{0.5}Ti_{0.5}O₂. To gain more information about the role of Mn in the formation of different kinds of nitrates, other experiments were performed, in which only NO in the absence of O₂ was adsorbed on Ce_{0.5}Ti_{0.5}O₂, Ce_{0.5}Ti_{0.4}Mn_{0.1}O_{2-δ}, and V/Ce_{0.5}Ti_{0.4}Mn_{0.1}O_{2-δ} samples (see Figure 6.8A). On Ce_{0.5}Ti_{0.5}O₂, only weak adsorption peaks of monodentate nitrate at 1535 and 1214 cm⁻¹ with significantly lower intensity compared to those after exposure to NO + O₂ flow were created (Figure 6.8A & B of the Ce_{0.5}Ti_{0.5}O₂ sample). In contrast, on Ce_{0.5}Ti_{0.4}Mn_{0.1}O_{2-δ}, both bridged and bidentate nitrates and adsorbed NO_x species were formed. The intensity of these bands is slightly lower than that formed after treatment in NO + O₂ flow (Figure 5.8A & B of the Ce_{0.5}Ti_{0.4}Mn_{0.1}O_{2-δ} sample), suggesting that Mn and surface oxygen in the vicinity of Mn play a significant role in the formation of these species. This assumption is in agreement with DFT calculations of Pintos *et al.*²²⁸ for Mn-doped CeO₂, which showed that Mn promotes the release of surface oxygen and consequently the formation of surface oxygen vacancies. It should be noted that bridged and bidentate nitrates are more active than monodentate nitrates.^{227, 229} Therefore, a higher amount of these species leads to the faster reaction between them and NH₃, which is evident by a rapid decrease in the intensity of bands at 1620-1557 cm⁻¹ on Ce_{0.5}Ti_{0.4}Mn_{0.1}O_{2-δ} and Ce_{0.5}Ti_{0.3}Mn_{0.2}O_{2-δ} supports (Figure 6.7A).

Interestingly, no bands at all are created upon exposure of the Mn-free catalyst V/Ce_{0.5}Ti_{0.5}O₂ to NO + O₂ flow at 175 °C (Figure 6.7B). This result evidences clearly that NO does not interact with the vanadium species surface but only with adsorbed NH₃ and NH₄⁺ species. A possible reason may be that Ce-O moieties responsible for oxidation and fixation of NO/O₂ as surface nitrates are covered by VO_x. The same behaviour was found for V/Ce_{1-x}Ti_xO₂ catalysts in section 5.3, page 64. In comparison, on Mn-containing catalysts V/Ce_{0.5}Ti_{0.4}Mn_{0.1}O_{2-δ} and V/Ce_{0.5}Ti_{0.3}Mn_{0.2}O_{2-δ}, bridged and bidentate nitrates are formed after treatment in

NO + O₂ flow. However, compared to the V-free supports, the corresponding IR bands are much weaker on the V-containing catalysts. This is probably due to coverage of a part of the strongly oxidizing Mnⁿ⁺ by VO_x species, thus, making the catalysts more selective (Figure 6.1E). After 5 min exposure to NH₃, these nitrates rapidly diminished and the bands of adsorbed NH₃ and NH₄⁺ species appeared on V/Ce_{0.5}Ti_{0.4}Mn_{0.1}O_{2-δ} and V/Ce_{0.5}Ti_{0.3}Mn_{0.2}O_{2-δ}. When the exposure time of NH₃ reached 45 min, the DRIFT spectra were similar to those after 45 min exclusive exposure to NH₃ without pretreatment in NO+O₂ (compare black top traces in Figure 6.7B and red bottom traces in Figure 6.6B). These results indicate that the NH₃ adsorption is dominant process in NH₃-SCR reaction over supported vanadia catalysts.

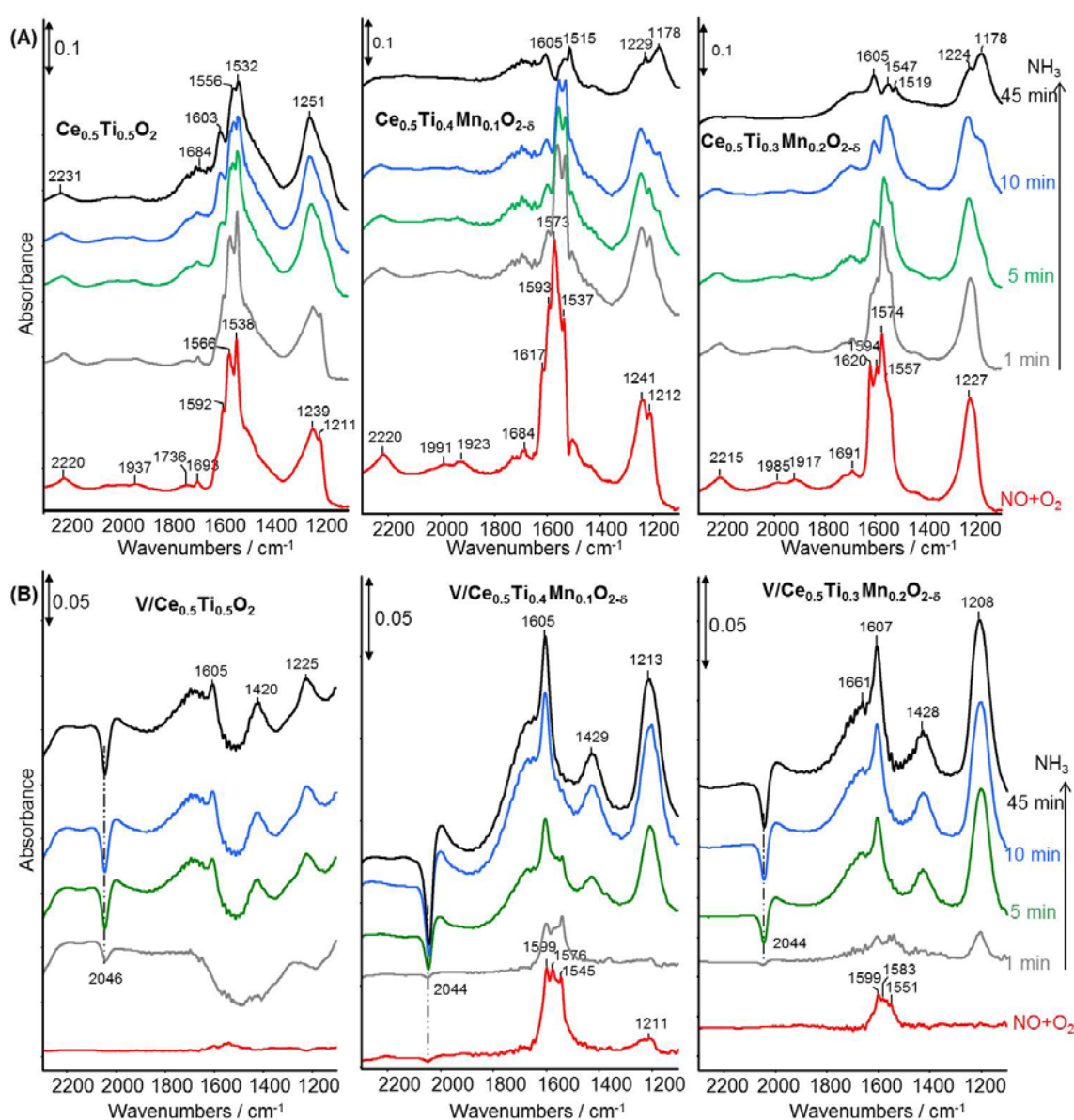


Figure 6.7: Difference DRIFT spectra recorded at 175 °C of bare supports (A) and V-containing catalysts (B) after 45 min exposure at 175 °C to 0.1% NO, 5% O₂/He flow followed by purging in He for 30 min and subsequent switch to 0.1% NH₃/He flow.

Comparison of all these *in-situ*-DRIFTS results points to interesting differences in the role of vanadium and manganese sites in NH_3 -SCR. NH_3 can be adsorbed and activated on all surface species, while NO_x species are only adsorbed on M (M= Mn, Ce, Ti) surface sites but not on vanadium species. These results suggest that NH_3 -SCR over Mn-containing bare supports proceeds after a L-H mechanism, in which both NO and NH_3 are first adsorbed to give activated surface species that further react to produce N_2 and H_2O . In the case of V-containing catalysts, an E-R mechanism is still dominating.

To further confirm this assumption, an additional DRIFTS experiment has been performed, in which total NH_3 -SCR feed was adsorbed. Figure 6.8D exhibits both coordinated NH_3 ($1607\text{-}1604\text{ cm}^{-1}$) and adsorbed nitrates ($1554\text{-}1532$ and $1250\text{-}1214\text{ cm}^{-1}$) on $\text{Ce}_{0.5}\text{Ti}_{0.5}\text{O}_2$ and $\text{Ce}_{0.5}\text{Ti}_{0.4}\text{Mn}_{0.1}\text{O}_{2-\delta}$ supports after exposing to total NH_3 -SCR feed, indicating that both NH_3 and NO_x are adsorbed in separate sites. However, the intensity of peaks attributed to adsorbed nitrates under NH_3 -SCR feed is significantly lower than under $\text{NO} + \text{O}_2$, suggesting that these species react with NH_3 adsorbed at a nearby V site to form N_2 and H_2O . This reaction is also supported by the presence of an additional peak at $1362\text{-}1358\text{ cm}^{-1}$, which can be assigned to active intermediates such as nitro or chelating nitrite species. This result is in line with literature reports obtained for other catalyst systems.²³⁰⁻²³¹

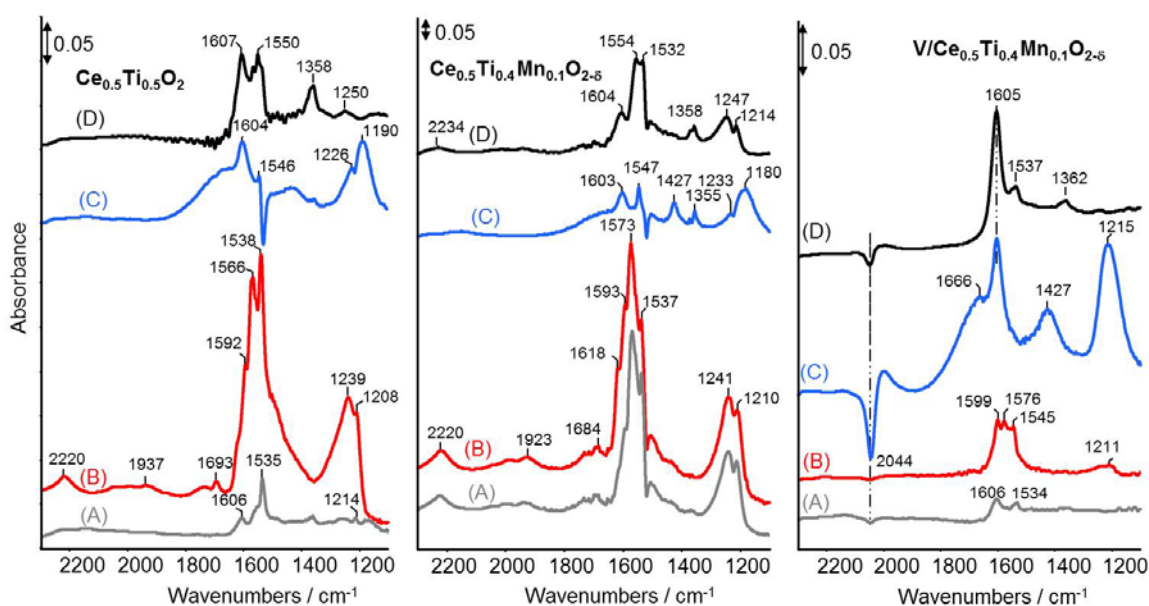


Figure 6.8: Difference DRIFT spectra recorded at 175 °C of $\text{Ce}_{1-x}\text{Ti}_x\text{O}_2$, $\text{Ce}_{0.5}\text{Ti}_{0.4}\text{Mn}_{0.1}\text{O}_{2-\delta}$ and $\text{V/Ce}_{0.5}\text{Ti}_{0.4}\text{Mn}_{0.1}\text{O}_{2-\delta}$ after 45 min exposure at 175 °C to 0.1% NO/He flow (A), 0.1% NO, 5% O_2 /He flow (B), 0.1% NH_3 /He flow (C), total NH_3 -SCR feed (D).

In contrast, on the $\text{V/Ce}_{0.5}\text{Ti}_{0.4}\text{Mn}_{0.1}\text{O}_{2-\delta}$ catalyst, dominant coordinated NH_3 species were present. This result supports again the conclusion that over supported vanadia catalysts, the NH_3 -SCR reaction proceeds according to an E-R mechanism

involving the reaction of adsorbed NH_3 species with gas-phase NO_x . Moreover, the difference DRIFT spectrum of $\text{V/Ce}_{0.5}\text{Ti}_{0.4}\text{Mn}_{0.1}\text{O}_{2-\delta}$ under total NH_3 -SCR feed shows a much lower intensity of the negative $2\nu(\text{V}=\text{O})$ band at 2044 cm^{-1} compared to that under NH_3 flow. This indicates that the equilibrium V valence state under SCR conditions is maintained close to +5, probably due to the highly redox-active of Mn-Ce-Ti support, which enhances the catalytic performance of this catalyst.

In-situ-EPR investigations

The *in-situ*-EPR spectra of the $\text{V/Ce}_{0.5}\text{Ti}_{0.5}\text{O}_2$ catalyst in NH_3 , $\text{NO}+\text{O}_2$ and NH_3 -SCR feed flow were very similar to those of the $\text{V/Ce}_{0.5}\text{Ti}_{0.5}\text{O}_2$ catalyst prepared by co-precipitation (see Figure 5.7 in chapter 5). Therefore, they are not shown in this section.

Operando EPR spectra of the Mn-containing samples $\text{Ce}_{0.5}\text{Ti}_{0.3}\text{Mn}_{0.2}\text{O}_{2-\delta}$ and $\text{V/Ce}_{0.5}\text{Ti}_{0.3}\text{Mn}_{0.2}\text{O}_{2-\delta}$ after treatment in different gases are shown in Figure 6.9. The line sextet of Mn^{2+} single sites ($g = 2.004$ and $A = 90\text{G}$) in the $\text{Ce}_{0.5}\text{Ti}_{0.3}\text{Mn}_{0.2}\text{O}_{2-\delta}$ support nearly did not change under different treatments suggesting that these species might be hidden in the bulk lattice and not active for the NH_3 -SCR reaction. The intensity of the broad background EPR signals of $\text{Ce}_{0.5}\text{Ti}_{0.3}\text{Mn}_{0.2}\text{O}_{2-\delta}$ of interacting Mn^{2+} species slightly increased and broadened upon switching from Ar to NH_3/He flow. This is seen more clearly from the normalized intensity I/I_{Ar} plotted in Figure 6.10A. It points to the formation of more Mn^{2+} , probably due to the reduction of EPR-silent Mn^{3+} species present as Mn_2O_3 in the as-prepared sample (evident from the XRD pattern of $\text{Ce}_{0.5}\text{Ti}_{0.3}\text{Mn}_{0.2}\text{O}_{2-\delta}$, Figure A.20A). In contrast, as mentioned above, the intensity of the hfs sextet of single Mn^{2+} does not change, suggesting that these species are indeed hidden in the supporting bulk and not accessible to reactants. Upon switching to $\text{NO} + \text{O}_2$ flow, the intensity of the Mn^{2+} cluster signal decreased again, confirming their reversible reoxidation to Mn^{3+} (Figure 6.9A and Figure 6.10A). Upon switching to the total SCR feed flow, the Mn^{2+} cluster signal became slightly broader and increased again, indicating that Mn^{3+} ions are again partly reduced. This confirms clearly the reversible redox behaviour of Mn ions within Mn_xO_y clusters in different conditions and several cycles. This facile redox behaviour might be the reason for catalytic activity of this support for low-temperature NH_3 -SCR.

The same behaviour was observed for the catalyst $\text{V/Ce}_{0.5}\text{Ti}_{0.3}\text{Mn}_{0.2}\text{O}_{2-\delta}$ (Figure 6.9B). However, compared to the V-free support, the spectra of the catalyst differ more significantly in intensity during subsequent treatment in NH_3 , NO/O_2 and SCR feed. This might be due to the reduction of VO^{3+} to VO^{2+} species in NH_3 , their reoxidation in NO/O_2 and subsequent partial re-reduction during NH_3 -SCR. Since the broad isotropic singlet of magnetically interacting VO^{2+} species overlaps with

that of clustered Mn^{2+} species, (compare Figure 6.9C to Figure 5.7, page 59, section 5.2.2), the effect of both species cannot be distinguished. Remarkably, no hfs signal of isolated VO^{2+} species was formed. This is evident from Figure 6.10B, in which difference spectra recorded after 30 min in total SCR feed are shown (spectra after proceeding 30 min exposure to $\text{NO}+\text{O}_2$ subtracted). This may be due to strong magnetic interactions between paramagnetic VO^{2+} and Mn^{n+} species. On the other hand, the redox potential of $\text{Mn}^{3+}/\text{Mn}^{2+}$ (1.5 V) is higher than that of $\text{V}^{5+}/\text{V}^{4+}$ (approximately 1.0 V).¹⁵⁴ Therefore, it cannot be excluded that V species in close contact to Mn^{n+} ($n>2$) are kept in their highest valence state +5 while Mn^{n+} is reduced to Mn^{2+} , contributing to the EPR signal. The contribution of VO^{2+} (or additional Mn^{2+}) species to the total EPR signal intensity under reductive conditions in NH_3 flow or total NH_3 -SCR feed is also evident from Figure 6.10A, in which the ratio of the total EPR intensity under different gas atmosphere is normalized on the initial one under argon flow.

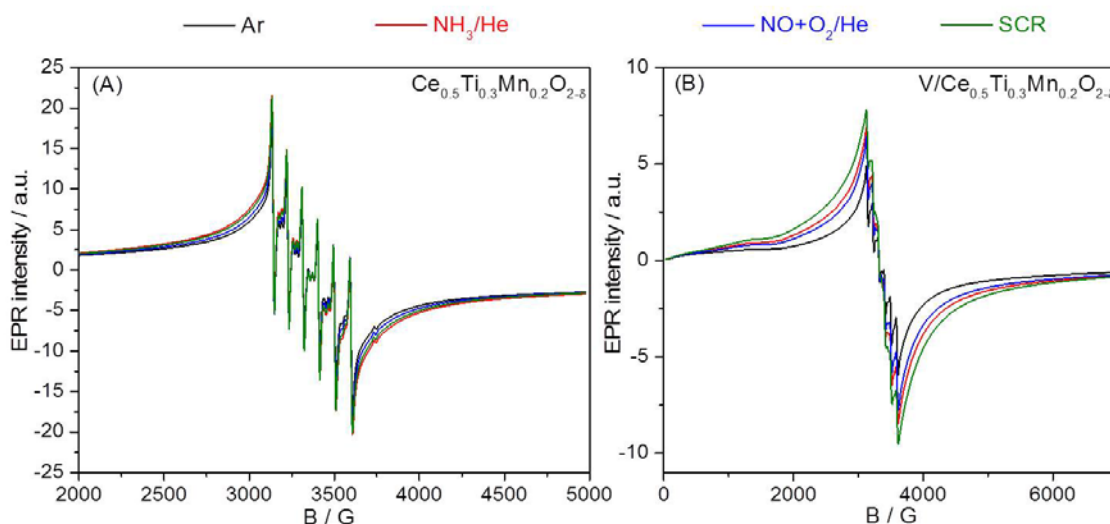


Figure 6.9: *In-situ*-EPR spectra of support $\text{Ce}_{0.5}\text{Ti}_{0.3}\text{Mn}_{0.2}\text{O}_{2-\delta}$ (A) and catalyst $\text{V}/\text{Ce}_{0.5}\text{Ti}_{0.3}\text{Mn}_{0.2}\text{O}_{2-\delta}$ (B) recorded at 150 °C after 1 h pretreatment in O_2 flow at 300 °C and cooling to 150 °C in Ar flow, followed by 30 min exposure to 0.1% NH_3/Ar , then 30 min exposure to 0.1% NO, 5% O_2/Ar , finally 30 min exposure to total SCR feed flow.

In general, the behaviour of the supports and catalysts with lower Mn content was similar to that of $\text{Ce}_{0.5}\text{Ti}_{0.3}\text{Mn}_{0.2}\text{O}_{2-\delta}$ and $\text{V}/\text{Ce}_{0.5}\text{Ti}_{0.3}\text{Mn}_{0.2}\text{O}_{2-\delta}$, respectively. Therefore, it is not shown here. The only difference is the effect of Mn content on the reduction degree of the supports. As seen from Figure 6.10B, sample $\text{Ce}_{0.5}\text{Ti}_{0.45}\text{Mn}_{0.05}\text{O}_{2-\delta}$ contains the smallest amount of clustered Mn^{2+} species. However, the reduction degree of this sample is generally highest between the supports $\text{Ce}_{0.5}\text{Ti}_{0.5-x}\text{Mn}_x\text{O}_{2-\delta}$ ($x=0.05-0.2$) (Figure 6.10A). This may be a reason for the least active of this support (Figure 6.1A).

The difference spectra recorded after 30 min in total SCR feed (spectra after proceeding 30 min exposure to NO+O₂ subtracted) shown almost exclusively the broad signal of clustered Mn²⁺ species (Figure 6.10B). The intensity of these spectra, which is related to the amount of clustered Mn²⁺ species, increased the order Ce_{0.5}Ti_{0.45}Mn_{0.05}O_{2-δ} < Ce_{0.5}Ti_{0.4}Mn_{0.1}O_{2-δ} < Ce_{0.5}Ti_{0.3}Mn_{0.2}O_{2-δ}, which parallels the trend in catalytic behaviour of these supports.

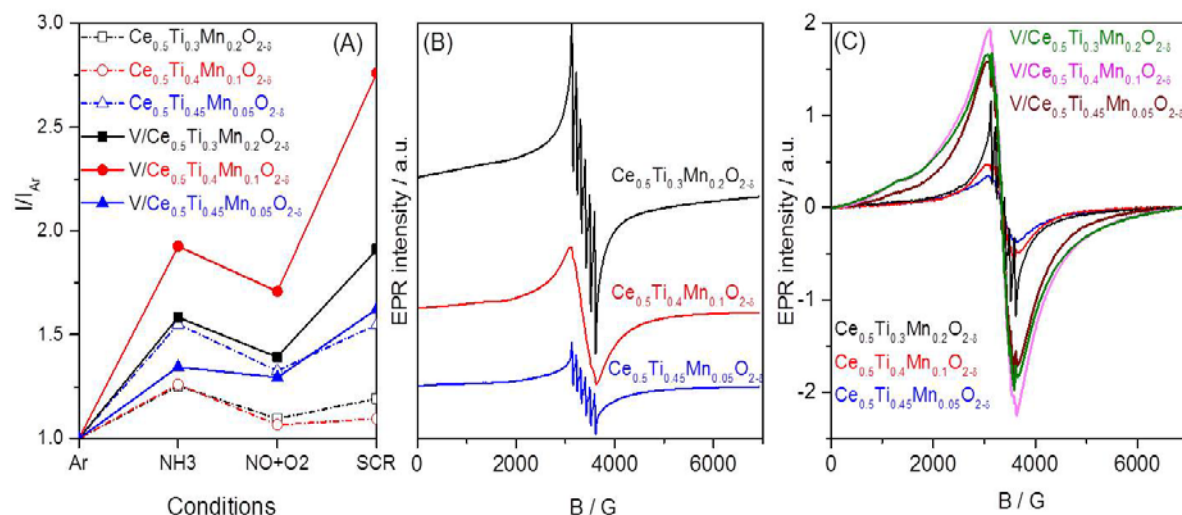


Figure 6.10: (A): The ratio of double integrals of the EPR spectra of samples recorded after 30 min exposure to different gas flows to that recorded under Ar flow at 150 °C; (B): The EPR spectra of supports recorded at 150 °C after 30 min exposure to total SCR feed flow; (C) Comparison of the difference EPR spectra of samples recorded after 30 min in total SCR feed (spectra after proceeding 30 min exposure to NO+O₂ subtracted).

6.3. Conclusions

This chapter pointed out the significant influence of Mn for the mixed-oxide support CeO₂-TiO₂ to obtain the higher catalytic activity of supported vanadia catalysts for NH₃-SCR at lower temperatures. With a certain amount of Mn, supports Ce_{0.5}Ti_{0.45}Mn_{0.05}O_{2-δ} and Ce_{0.5}Ti_{0.4}Mn_{0.1}O₂ were already very active in the absence of vanadia achieving both NO and NH₃ conversion above 85% from 175 to 300 °C and remaining N₂ selectivity at 95% until 300 °C. Only for the highest Mn content in Ce_{0.5}Ti_{0.3}Mn_{0.2}O₂, a strong selectivity decrease appeared above 200 °C. Deposition of vanadia on these supports slightly enhanced catalytic performance with NO conversion above 88% and N₂ selectivity around 98% from 175 to 300 °C. The XRD results revealed the formation of homogeneous Ce_{0.5}Ti_{0.5-x}Mn_xO_{2-δ} solid solutions with $x \leq 0.1$. In contrast, a separate Mn₂O₃ and Ce₂O₃ was found with $x = 0.2$ indicating the presence of heterogeneous solid.

Comprehensive studies of structure-reactivity relationships using *in-situ* and *operando* spectroscopy pointed to interesting role differences of vanadium and

manganese sites in NH_3 -SCR. While NH_3 can be adsorbed and activated on all surface species, NO_x species are only adsorbed on M (M= Mn, Ce, Ti) surface sites but not on vanadium species. EPR revealed the contribution of both vanadium and manganese sites to the low-temperature NH_3 -SCR over $\text{V/Ce}_{0.5}\text{Ti}_{0.5-x}\text{Mn}_x\text{O}_{2-\delta}$ catalysts. Among different types of Mn species, those in clusters are more active than isolated species. The Mn-O-Ce-O-Ti interaction results in high redox activity of ternary oxide supports. Therefore, their interaction with adjacent vanadium surface species kept the latter in an equilibrium V valence state close to +5 during NH_3 -SCR. Furthermore, DRIFTS results demonstrated that NH_3 -SCR over Mn-containing bare supports proceeds after a L-H mechanism, in which both NO and NH_3 are first adsorbed to give activated surface species that further react to produce N_2 and H_2O . This agrees with the behaviour of the Ti-containing supports. Active Mn species improved the formation of bridged and bidentate nitrates and, thus, enhanced the catalytic performance of NH_3 -SCR at low temperature. In the case of supported vanadia catalysts, the NH_3 -SCR reaction proceeds mainly according to an E-R mechanism involving the reaction of adsorbed NH_3 species and gas-phase NO_x , however, in contrast to the $\text{V/Ce}_{1-x}\text{Ti}_x\text{O}_2$ catalysts, NO_x is also partly adsorbed on $\text{V/Ce}_{0.5}\text{Ti}_{0.5-x}\text{Mn}_x\text{O}_{2-\delta}$ catalysts. This is possibly a reason for the slightly higher performance of these samples in comparison to the former.

7. Effect of preparation methods of supports on structure and performance of VO_x/CeO₂ catalysts

In chapter 4 it has been shown that VO_x/Ce_{1-x}Zr_xO₂ materials, in which the supports were prepared by citrate sol-gel method, are efficient catalysts for low-temperature NH₃-SCR of NO. They contain –O–Ce–O–V(=O)–O–Zr–O– moieties in which the V sites shuttle reversibly between V⁵⁺ and V⁴⁺ while Ce and Zr species remain essentially tetravalent. Interestingly, the same amount of vanadia deposited on a CeO₂ support prepared by precipitation (chapter 5) resulted in catalysts of rather different performance. A sensitive dependence of the performance of ceria-based catalysts on the synthesis procedure was also observed in other reactions, such as methanol oxidation and carbonylation of glycerol with CO₂ to glycerol carbonate,²³²⁻²³⁴ for which ceria was prepared by hydrothermal,²³⁵ precipitation,^{232, 236} citrate sol-gel,^{124, 233} solution combustion,²³⁷ or microemulsion protocols²³⁴. It has been supposed in previous reports that, depending on the synthesis protocol, oxygen vacancies and structural defects are formed that in turn influence the Ce⁴⁺/Ce³⁺ redox behaviour.^{19, 238} In NH₃-SCR, however, a detailed analysis of these relations has not yet been performed. Therefore, in this chapter a detailed investigation of structure-reactivity relationships of catalysts is presented, in which the same impregnation procedure was used to deposit 5 wt.% of V₂O₅ on CeO₂ supports that were prepared by different methods, namely by precipitation and a citrate sol-gel method (leading to catalysts V/CeO₂-P and V/CeO₂-C).

7.1. Catalytic performance

As illustrated in Figure 7.1B, the pure CeO₂ supports already show some activity in the catalytic reaction. While NO_x and NH₃ conversions were almost equal and low over the whole temperature range on support CeO₂-P, sample CeO₂-C was slightly more active below 200 °C. However, NO conversion decreased significantly with rising temperature and dropped to 0% at 300 °C. This is caused by undesired NH₃ combustion and N₂O formation above 200 °C. Thus, both pure supports shown detrimental catalytic behaviour and are therefore not further considered here.

Catalyst V/CeO₂-C is much less active than V/CeO₂-P, reaching a maximum NO conversion of 90% at only 275 °C which even dropped at higher temperature due to undesired oxidation of NH₃ (Figure 7.1A). In contrast, V/CeO₂-P reached full conversion already at 225 °C and remained stable.

To find out reasons for their different behaviour, a comprehensive characterization study of the catalysts was performed. These results are discussed in relation to the catalytic performance in the following sections of this chapter.

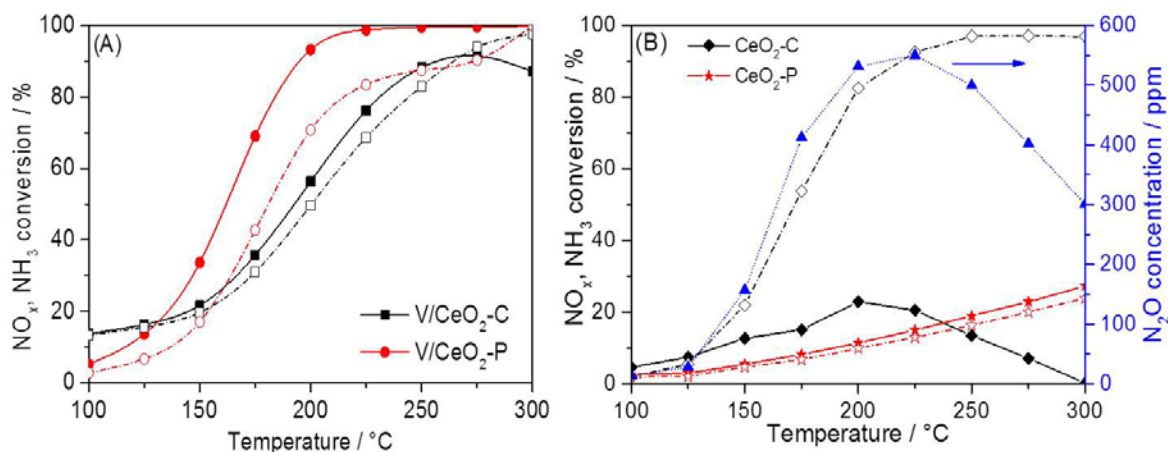


Figure 7.1: NO_x (solid symbols and lines), NH_3 conversion (open symbols and dashed lines) over (A) $\text{V/CeO}_2\text{-C}$ (squares) and $\text{V/CeO}_2\text{-P}$ (circles); (B) $\text{V-free CeO}_2\text{-C}$ (diamonds) and $\text{CeO}_2\text{-P}$ (stars); and N_2O concentration (solid triangles and dotted lines) over $\text{V-free CeO}_2\text{-C}$ as a function of temperature; Feed composition: 0.1% NO , 0.1% NH_3 , 5% O_2/He , $\text{GHSV} = 70,000 \text{ h}^{-1}$.

7.2. Catalyst characterization

XRD patterns of both $\text{CeO}_2\text{-C}$ and $\text{CeO}_2\text{-P}$ supports showed the characteristic peaks of the cubic fluorite structure (Figure 4.2A and 5.3A). They are sharper and more intense for $\text{CeO}_2\text{-C}$ probably due to its larger mean crystallite size and a smaller strain derived by the Williamson-Hall equation (Equation 3.6 and Table 7.1). The strain in $\text{CeO}_2\text{-P}$ is about twice as high as in $\text{CeO}_2\text{-C}$, which might promote oxygen mobility inside the support.

Table 7.1: The mean crystallite size, specific surface area and pore volume, band gap energy of supports and catalysts.

Sample	Mean crystallite size ^[a] (nm)	Strain ^[a]	Surface area ($\text{m}^2 \text{g}^{-1}$)	Pore volume ($\text{cm}^3 \text{g}^{-1}$)	Band gap energy (eV) ^[b]
$\text{CeO}_2\text{-C}$	24.3	0.00138	12.7	0.026	3.00
$\text{CeO}_2\text{-P}$	14.1	0.00265	61.2	0.060	2.72
$\text{V/CeO}_2\text{-C}$			11.5	0.043	2.58
$\text{V/CeO}_2\text{-P}$			45.4	0.053	2.25

^[a] from XRD using the Williamson-Hall E.q. (Eq. 3.6), ^[b] from UV-Vis-DRS

Moreover, the BET surface area and pore volume of $\text{CeO}_2\text{-P}$ and $\text{V/CeO}_2\text{-P}$ are significantly larger than those of $\text{CeO}_2\text{-C}$ and $\text{V/CeO}_2\text{-C}$. This result is most

probably due to the fact that the P-samples are mesoporous while the C-samples are non-porous or macroporous (Figure A.23A).¹³¹

The UV-Vis-DR spectra of the pure CeO_2 supports showed bands below 250 nm, around 280 and 350 nm. The first is usually assigned to $\text{O}^{2-} \rightarrow \text{Ce}^{3+}$ charge-transfer transitions while the latter arose from $\text{O}^{2-} \rightarrow \text{Ce}^{4+}$ CT and interband transitions (Figure 7.2).^{139, 144} The intensity below 250 nm of $\text{CeO}_2\text{-P}$ is higher suggesting a higher content of Ce^{3+} which, for maintaining electroneutrality, must create oxygen vacancies. This assumption is supported by the fact that the absorption edge of $\text{CeO}_2\text{-P}$ ($E_g = 2.72$ eV) is red-shifted compared to $\text{CeO}_2\text{-C}$, for which $E_g = 3.00$ eV is close to the value of bulk CeO_2 (3.15 eV),²³⁹ as well as by Raman data discussed below. Such red shift is caused by a drop in lattice symmetry due to increased disorder, which may result from small nanoparticles with abundant surface defects and/or replacement of Ce by other metal ions with a different diameter.^{139, 144} It agrees well with the smaller crystallite size and higher strain of $\text{CeO}_2\text{-P}$ (Table 7.1).

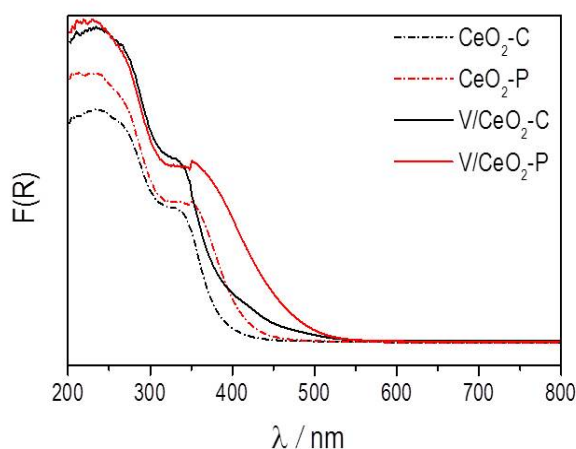


Figure 7.2: UV-Vis spectra of pure CeO_2 supports and 5% $\text{V}_2\text{O}_5/\text{CeO}_2$ catalysts.

Deposition of vanadia on these supports led to an increase of absorbance below 400 nm, due to characteristic for $\text{O}^{2-} \rightarrow \text{V}^{5+}$ CT bands of VO_x single sites and small V_xO_y clusters.¹⁵⁸ The weak shoulder extending from 400 to 500 nm in sample $\text{V}/\text{CeO}_2\text{-C}$ might arise from few V_2O_5 nanocrystals,¹⁵⁵ which were evident, too, from the Raman spectra. Interestingly, a marked red shift of the absorption edge was observed for $\text{V}/\text{CeO}_2\text{-P}$. One could suppose that this is due to a higher V site agglomeration in this sample since it has been shown previously that the absorption edge energy of V_xO_y -containing oxides decreases with the number of V-O-V bridges.¹⁵⁹ However, the Raman spectra in Figure 5.5 (page 55) do not indicate more intense V_2O_5 bands for sample $\text{V}/\text{CeO}_2\text{-P}$ and the EPR spectra in Figure 7.3 (discussed below) suggest a higher V site agglomeration in $\text{V}/\text{CeO}_2\text{-C}$ rather than in $\text{V}/\text{CeO}_2\text{-P}$. Based on these results, the red shift of the absorption edge in sample V/CeO_2 is probably assigned to an incorporation of V in the surface of CeO_2 and, thus, a more efficient attachment of the VO_x species to the support than in $\text{V}/\text{CeO}_2\text{-C}$.

7.3. *In-situ* investigation of the formation and structure of active moieties

As mentioned in Section 4.3, page 42, *in-situ*-UV-Vis spectra of V/CeO₂-C recorded at 200 °C after 60 min pretreatment in air flow at 275 °C and 45 min exposure to the NH₃-SCR feed stream at 200 °C indicate a loss of intensity in the region of CT bands of V⁵⁺ between 400-500 nm, while the band of d-d transitions of reduced V^{5-x} species above 600 nm rises (Figure A.6). This change is reversible in NO/O₂ flow after removing NH₃ from the feed. A similar behaviour has been observed, too, for V/CeO₂-P (Figure A.24). In Section 4.3, the time dependent UV-Vis experiments were conducted with the V/Ce_{1-x}Zr_xO₂ catalyst series, indicating that the reduction/reoxidation rates of surface VO_x species (derived by kinetic evaluation of the time-dependent UV-Vis absorbance at 700 nm) scaled with catalytic activity, the least active V/CeO₂-C catalyst showing the lowest rates. Therefore, for comparison, the same experiment was performed with V/CeO₂-P. The rate constants of V reduction in a flow of 0.1% NH₃/He and reoxidation in 5% O₂/He flow at 200 °C (Table 7.2) were derived from fits of the experimental data in Figure A.25 by a first-order rate law (E.q. 4.1 and 4.2)

Table 7.2: Rate constants of V reduction and reoxidation (k/min⁻¹).

Sample	V/CeO ₂ -C ^[a]	V/CeO ₂ -P
k _{red1}	0.104	0.0185
k _{red2}	0.271	0.0185
k _{reox1}	0.003	0.023
k _{reox2}	0.181	1.096

^[a] from Table 4.3

The fits revealed two V reduction and reoxidation processes, a fast and a slow one (Figure A.25). It can be assumed that the fast processes (k_{red2} and k_{reox2}) might be related to V sites on the top surface. These are the ones in immediate contact with reactants and most probably govern the catalytic activity. The slow processes (k_{red1} and k_{reox1}) may reflect V sites in subsurface layers, which might play, if at all, only a minor role in catalysis, since particularly their reoxidation is hindered. Interestingly, reduction and reoxidation of top surface V species proceed with similar rates in the less active catalyst V/CeO₂, while in V/CeO₂-P reduction is by 2 orders of magnitude slower, yet reoxidation is by a factor of about 10 faster. For NH₃-SCR of NO on FeO_x and MnO_x containing catalysts, it was found that NO is not directly reduced by NH₃ but first oxidized to adsorbed nitrite and/or nitrate species by Fe³⁺ or Mn⁴⁺ according to a Mars-van Krevelen mechanism – a process which is hardly catalysed by metal ions in non-reducible valence states such as Fe²⁺ or Mn²⁺.^{226, 240}

Anticipating that a $V^{n+}/V^{(n-1)+}$ redox shuttle is working in NH_3 -SCR of NO over V/CeO_2 , too, fast reoxidation of reduced V species would be beneficial to ensure high catalytic activity. Thus, the high reoxidation rate of V/CeO_2 -P could be one reason for its higher activity compared to V/CeO_2 -C.

A more accurate analysis of reaction-dependent changes on the surface was performed by pseudo-in-situ-XPS after 60 min pretreatment in air flow at 300 °C and after 30 min exposure to SCR feed at 200 °C without subsequent contact to ambient atmosphere (Table 7.3, spectra plotted in Figure 4.7 and A.10). Generally, six features observed in the Ce 3d region are labeled with v, v'', v''' ($3d_{5/2}$) and u, u'', u''' ($3d_{3/2}$) (Figure A.5). For clarity, only E_B values of the v peak are summarised in Table 7.3.

Table 7.3: Pseudo-in-situ-XPS Binding Energies (E_B /eV) and Atomic Ratios of V/CeO_2 after pretreatment in the air and SCR feed at 200 °C.

Sample	E_B (V 2p _{3/2})	E_B (Ce 3d _{3/2})	V/Ce
V/CeO ₂ -C air	516.5 ($V^{4+} + V^{5+}$)	885.5 (Ce^{4+})	0.73
	518.0 (V^{5+})		
V/CeO ₂ -C after SCR	516.6 ($V^{4+} + V^{5+}$)	885.5 (Ce^{4+})	0.67
	515.0 (V^{3+})		
V/CeO ₂ -P air	517.0 (V^{5+})	885.5 (Ce^{4+})	0.52
V/CeO ₂ -P after SCR	516.2 (V^{4+})	885.5 (Ce^{4+})	0.44
		882.5 (Ce^{3+})	

The surface V/Ce ratio of the more active catalyst V/CeO_2 -P was lower than that of V/CeO_2 -C, probably since its higher surface area leads to a lower V surface concentration, despite a similar V dispersion. After air pretreatment, the surface of this catalyst consisted of exclusively V^{5+} (reflected by $E_B = 517.0$ eV) while that of V/CeO_2 -C represented a mixture of V^{5+} and V^{4+} ($E_B = 518.0$ and 516.5 eV).¹⁴⁸ After treatment in SCR feed, the surface V^{5+} sites on V/CeO_2 -P were partially reduced to V^{4+} while on V/CeO_2 -C, a considerable part of V^{3+} was formed. Under the same conditions, Ce remained essentially tetravalent in V/CeO_2 -C, while it was partially reduced to Ce^{3+} in V/CeO_2 -P. This phenomenon may be explained by the removal of O and localisation of the residual electrons at the neighbouring Ce, leaving behind $-Ce^{3+}-\square-V^{5+}(=O)-O-Ce^{3+}-$ and $-Ce^{3+}-\square-V^{4+}(=O)-O-Ce^{4+}-$ species. This assumption has been confirmed by DFT calculations of VO_x/CeO_2 catalysts.¹⁰⁶ Preferential electron trapping by Ce^{4+} could keep a considerable part of the V sites in V/CeO_2 -P in their most active valence state +5 under reaction conditions, which would agree very well with the observed higher activity.

In-situ-EPR widely supports the conclusions drawn from UV-Vis and XPS data. After pre-oxidation, the EPR spectra of both catalysts consisted of only tiny signals around $g = 2.00$ from oxygen defects such as O^{\bullet} and/or $O_2^{\bullet-}$ (Figure 7.3, C1 and P1). No V^{4+} signal was detected, which is surprising at least for V/CeO_2-C as XPS points to some surface V^{4+} . Possibly, this is due to the local environment of these sites on the surface of V/CeO_2-C , leading to short relaxation times. Exposure to NH_3/He flow at $200\text{ }^{\circ}C$ reduced the V^{5+} species in sample V/CeO_2-P to VO^{2+} , evident from the original EPR

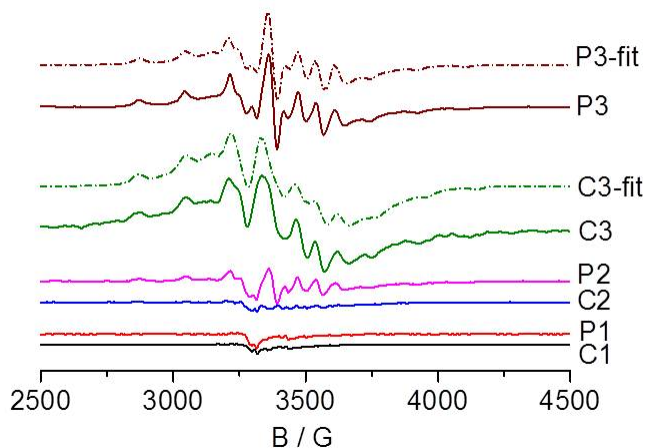


Figure 7.3: *In-situ*-EPR spectra of V/CeO_2-C and V/CeO_2-P recorded at $200\text{ }^{\circ}C$ in Ar after pretreatment in O_2 at $300\text{ }^{\circ}C$ (C1 and P1), after 30 min treatment in 0.2% NH_3/He (C2 and P2) and after 30 min exposure to total SCR feed flow (C3 and P3), spectrum in 0.2% NO, 5% O_2/He subtracted. The dashed lines show spectra fitted with spin Hamiltonian parameters in Table A.3.

signal with hyperfine structure (hfs). Switching to the total SCR feed containing also NO and O_2 raised the intensity of this signal. This result points to oxidation of EPR-silent V^{3+} (formed during the previous treatment in NH_3) to EPR-active VO^{2+} and agrees very well with the *in-situ*-XPS result (Table 7.3). It is noted that no VO^{2+} signal was obtained in V/CeO_2-C after NH_3 -treatment (Figure 7.3, C2) indicating that reduction to V^{3+} may have been very pronounced which is, however, at least partly reversible under SCR feed (Figure 7.3, C3). From the g and A tensor parameters derived by simulated spectra and explained in more detail in Table A.3, it is evident that the hfs spectrum of catalyst V/CeO_2-C could be fitted with one single VO^{2+} site, while two different VO^{2+} species A and B were required for V/CeO_2-P . The parameters of the single VO^{2+} sites in $V-CeO_2-C$ and of VO^{2+} species A in $V-CeO_2-P$ were rather similar but differ significantly from VO^{2+} species B in $V-CeO_2-P$, which are less distorted and less ionic. Similar species have been found in $V/Ce_{0.7}Zr_{0.3}O_2$ and $V/Ce_{0.5}Ti_{0.5}O_2$ catalysts and assigned to V incorporated in $-O-Ce-O-V(=O)-O-Zr/Ti-O-$ surface moieties as discussed in Section 4.3, page 47 and Section 5.2.2, page 59, respectively. Accordingly, we assign the VO^{2+} species B in V/CeO_2-P to similar sites, tightly incorporated into the catalyst surface.

7.4. Conclusions

It has been demonstrated that the preparation method of supports crucially affects the resulting support structure and in turn the properties and activity of the VO_x sites deposited on them. In contrast to the citrate sol-gel protocol, the precipitation method exhibits many advantages since it can create a mesoporous $\text{CeO}_2\text{-P}$ support with a markedly higher surface area, a higher concentration of Ce^{3+} bulk species and oxygen vacancies, which favour oxygen transport through the lattice. This is beneficial for the corresponding $\text{V/CeO}_2\text{-P}$ (assuming a Mars-van Krevelen redox cycle) which is much more active than the respective $\text{V/CeO}_2\text{-C}$ material and approaches full NO conversion and N_2 selectivity already below 225 °C. While surface V sites are partly reduced under SCR conditions to (probably inactive) V^{3+} on $\text{V/CeO}_2\text{-C}$, this deep reduction does not occur on $\text{V/CeO}_2\text{-P}$ on which, instead, Ce^{4+} is preferentially reduced to Ce^{3+} . Moreover, EPR results suggest that V sites in $\text{V/CeO}_2\text{-P}$ might be in a more tight junction with the CeO_2 surface, probably forming active $-\text{Ce}^{3+}-\square-\text{V}^{5+/4+}(=\text{O})-\text{O}-\text{Ce}^{3+/4+}-$ which are anticipated to boost catalytic activity.

8. General conclusions and outlook

In this PhD research, supported $\text{VO}_x/\text{Ce}_{1-x}\text{M}_x\text{O}_2$ ($\text{M} = \text{Zr}, \text{Ti}, \text{Mn}$) catalysts have revealed to be promising ones for low-temperature $\text{NH}_3\text{-SCR}$. Incorporation of smaller cations ($\text{M} = \text{Zr}, \text{Ti}, \text{Mn}$) into CeO_2 formed ceria-based solid solutions with the cubic fluorite structure of ceria. These solid solutions have smaller crystallite size and/or higher disorder than pure ceria. These properties might improve oxygen mobility and redox capability of ceria leading to enhanced catalytic performance of supported vanadia catalysts.

The properties of supports play an essential role in the catalytic behaviour of supported vanadia catalysts depending on the co-elements. The gain in catalytic activity upon vanadia deposition increased in the same order as activity improvement of V-free supports $\text{CeO}_2 < \text{Ce}_{0.7}\text{Zr}_{0.3}\text{O}_2 < \text{Ce}_{0.5}\text{Ti}_{0.5}\text{O}_2 < \text{Ce}_{0.5}\text{Ti}_{0.4}\text{Mn}_{0.1}\text{O}_2$. The redox properties of supports are seen as the key factor determining the deNO_x activity of supported vanadia catalysts. Isovalent nonreducible co-elements of Zr^{4+} affect the redox capability of supports due to the distortion of the ceria structure by different cation size, whereas the influence of Ti^{4+} is related to both structural distortion and higher redox activity of this cation. In the case of Mn^{n+} co-component, this property also originates from the electronic modification. Therefore, in comparison with $\text{Ce}_{0.7}\text{Zr}_{0.3}\text{O}_2$, the higher reducible co-component of Ti^{4+} results in higher redox capability of the $\text{Ce}_{0.5}\text{Ti}_{0.5}\text{O}_2$ support, resulting in higher catalytic performance of the resulting catalysts. The best 5 wt.% $\text{V}_2\text{O}_5/\text{Ce}_{1-x}\text{Ti}_x\text{O}_2$ catalysts ($x = 0.3\text{-}0.5$) already reached full NO_x conversion and N_2 selectivity slightly below 200 °C with GHSV of 70,000 h^{-1} . The catalytic performance was still appreciable at a tenfold higher space velocity of 750,000 h^{-1} , which belongs to the most active and selective catalysts known so far for deNO_x at temperatures below 300 °C. Incorporation of both Ti and Mn into ceria results in high NO_x conversion even at lower temperatures (from 175 °C). However, the strong oxidation activity of Mn ions makes these supports slightly less selective. This limitation is ameliorated by the coverage of VO_x species on these supports.

Besides the influence of co-components, the preparation process of supports also crucially affects the structure and properties of resulting supports and, thus, the activity of supported vanadia catalysts. In contrast to the citrate sol-gel protocol, the precipitation method has many advantages. This method could create a mesoporous $\text{CeO}_2\text{-P}$ support with markedly higher surface area, a higher concentration of Ce^{3+} bulk species and oxygen vacancies, which favour oxygen transport through the lattice. As a consequence, the corresponding catalyst $\text{V/CeO}_2\text{-P}$ was much more active than the vanadia supported on ceria prepared by the citrate sol-gel method.

In-situ-spectroscopic studies indicated that the activity of low-temperature NH_3 -SCR is mainly related to the presence of highly dispersed vanadyl species tightly connected via oxygen bridges to both Ce and M ($\text{M} = \text{Zr}, \text{Ti}, \text{Mn}$). These vanadyl species enable to reduce and reoxidise easily during NH_3 -SCR of NO reaction. Apparently, the intimate contact with Ce/M renders the V species in their highest and most active equilibrium valence state +5. The high steady-state concentration of V^{5+} maintained under SCR conditions might improve Lewis acidity and, thus, NH_3 adsorption. Therefore, these findings strongly suggest that it is the efficiency of this process which is responsible for the catalytic performance of supported vanadia catalysts.

The comprehensive studies of structure-reactivity relationships using *in-situ* and *operando* spectroscopy revealed significant mechanistic differences. While on V-free supports, NH_3 -SCR proceeded after a Langmuir-Hinshelwood (L-H) mechanism implying the reaction of adsorbed NH_3 and nitrate species (formed on the surface by reaction of NO/O_2), an Eley-Rideal (E-R) mechanism operates on supported vanadia catalysts, in which adsorbed NH_3 and NH_4^+ react with NO/O_2 from the gas phase. The switch in reaction mechanism has its roots in structural differences of catalysts and supports. While NH_3 adsorbs on both Lewis and Brønsted sites present in all samples (though to a different extent), nitrate is preferentially formed from NO/O_2 by the participation of Ce/Mn-O moieties.

Although much progress has been made on ceria-based catalysts, further improvements in the NO_x conversion and N_2 selectivity over these materials are still required in order to facilitate the possible commercialization of these catalysts. The challenge will be to design a new generation of these catalysts that can achieve full NO_x conversion without any formation of N_2O . The performance of ceria-based catalysts is highly dependent on their structures and redox properties. To achieve high activity, catalysts with a high surface area, porous structures and high redox active are required. Therefore, further studies should focus on the synthesis of nanostructured modified ceria with controlled structures, morphologies and redox properties to enhance the catalytic performance. In addition, the oxygen storage capacity (OSC) and oxygen mobility, as well as the electron transport through the lattice of ceria-based oxides, might boost the reaction rate. It has been demonstrated that incorporation of lower valent cations such as Cu^{2+} , La^{3+} , Fe^{3+} into ceria could create a material with higher oxygen mobility and OSC. Therefore, the introduction such cations with redox properties might be an attractive option for further modification ceria.

Another big challenge for the low-temperature active catalysts is the stability. In comparison with the high-temperature operations, the effects of H_2O and SO_2 on the catalytic activity are more evident at low temperatures. Therefore, long-time

stability test and the resistance against H_2O and SO_2 of these catalysts are also needed. Furthermore, more studies need to be done to transfer catalysts developed in laboratory scale to practical industry. Therefore, further work should design the experimental activity tests more directly related to “real” catalyst working under industrial or diesel engine conditions at high GHSV and in the presence of H_2O and SO_2 .

References

1. Bruckner, A., *Chem. Soc. Rev.* **2010**, 39, 4673-4684.
2. Skalska, K.; Miller, J. S.; Ledakowicz, S., *Sci. Total Environ.* **2010**, 408, 3976-3989.
3. Pereira, C. J.; Amiridis, M. D., *ACS Symp. Ser.* **1995**, 587, 1-13.
4. Aneja, V. P.; Roelle, P. A.; Murray, G. C.; Southerland, J.; Erisman, J. W.; Fowler, D.; Asman, W. A. H.; Patni, N., *Atmos. Environ.* **2001**, 35, 1903-1911.
5. Bosch, H.; Janssen, F., *Catalytic Reduction of Nitrogen Oxides: A Review on the Fundamentals and Technology*. Elsevier: **1998**.
6. Busca, G.; Lietti, L.; Ramis, G.; Berti, F., *Appl. Catal., B* **1998**, 18, 1-36.
7. Cobb, D.; Glatch, L.; Ruud, J.; Snyder, S., *Environ. Prog.* **1991**, 10, 49-59.
8. Li, J.; Chang, H.; Ma, L.; Hao, J.; Yang, R. T., *Catal. Today* **2011**, 175, 147-156.
9. Chen, H.-Y., Cu/Zeolite SCR Catalysts for Automotive Diesel NO_x Emission Control. In *Urea-SCR Technology for deNO_x After Treatment of Diesel Exhausts*, Nova, I.; Tronconi, E., Eds. Springer New York: **2014**; pp 123-147.
10. Liu, X.; Wu, X.; Weng, D.; Si, Z., *Catal. Commun.* **2015**, 59, 35-39.
11. Wang, J.; Yu, T.; Wang, X.; Qi, G.; Xue, J.; Shen, M.; Li, W., *Appl. Catal., B* **2012**, 127, 137-147.
12. Li, C.; Li, Q.; Lu, P.; Cui, H.; Zeng, G., *Front. Environ. Sci. Engin.* **2012**, 6, 156-161.
13. Lian, Z.; Liu, F.; He, H., *Catal. Sci. Technol.* **2015**, 5, 389-396.
14. Peng, Y.; Wang, C.; Li, J., *Appl. Catal., B* **2014**, 144, 538-546.
15. Liu, Z.; Yi, Y.; Zhang, S.; Zhu, T.; Zhu, J.; Wang, J., *Catal. Today* **2013**, 216, 76-81.
16. Liu, C.; Shi, J.-W.; Gao, C.; Niu, C., *Appl. Catal., A* **2016**, 522, 54-69.
17. Trovarelli, A., *Catal. Rev.* **1996**, 38, 439-520.
18. Beckers, J.; Rothenberg, G., *Green Chem.* **2010**, 12, 939-948.
19. Vivier, L.; Duprez, D., *ChemSusChem* **2010**, 3, 654-678.
20. Li, S.; Zhu, H.; Qin, Z.; Wang, G.; Zhang, Y.; Wu, Z.; Li, Z.; Chen, G.; Dong, W.; Wu, Z.; Zheng, L.; Zhang, J.; Hu, T.; Wang, J., *Appl. Catal., B* **2014**, 144, 498-506.
21. Tang, C.; Zhang, H.; Dong, L., *Catal. Sci. Technol.* **2016**, 6, 1248-1264.
22. Ramis, G.; Yi, L.; Busca, G., *Catal. Today* **1996**, 28, 373-380.
23. Vittadini, A.; Casarin, M.; Selloni, A., *J. Phys. Chem. B* **2005**, 109, 1652-1655.
24. Inomata, M.; Miyamoto, A.; Murakami, Y., *J. Catal.* **1980**, 62, 140-148.
25. Soyer, S.; Uzun, A.; Senkan, S.; Onal, I., *Catal. Today* **2006**, 118, 268-278.
26. Topsoe, N. Y.; Dumesic, J. A.; Topsoe, H., *J. Catal.* **1995**, 151, 241-252.
27. Giraud, F.; Couble, J.; Geantet, C.; Guilhaume, N.; Puzenat, E.; Gros, S.; Porcheron, L.; Kanniche, M.; Bianchi, D., *J. Phys. Chem. C* **2015**, 119, 16089-16105.

28. Wang, J.; Yan, Z.; Liu, L.; Chen, Y.; Zhang, Z.; Wang, X., *Appl. Surf. Sci.* **2014**, *313*, 660-669.
29. Liu, Z.; Zhang, S.; Li, J.; Zhu, J.; Ma, L., *Appl. Catal., B* **2014**, *158–159*, 11-19.
30. Centeno, M. A.; Carrizosa, I.; Odriozola, J. A., *Appl. Catal., B* **2001**, *29*, 307-314.
31. Boningari, T.; Koirala, R.; Smirniotis, P. G., *Appl. Catal., B* **2013**, *140–141*, 289-298.
32. Takagi, M.; Kawai, T.; Soma, M.; Onishi, T.; Tamaru, K., *J. Catal.* **1977**, *50*, 441-446.
33. Topsoe, N. Y., *Science (New York, N.Y.)* **1994**, *265*, 1217-1219.
34. Xiong, S.; Xiao, X.; Liao, Y.; Dang, H.; Shan, W.; Yang, S., *Ind. Eng. Chem. Res.* **2015**, *54*, 11011-11023.
35. *Air quality in Europe - 2015 report*, No 5; Luxembourg: Publications Office of the European Union, **2015**.
36. Wright, J., *Environmental Chemistry*. Routledge Taylor Francis Group: **2003**.
37. Ogawa, M.; Yoshida, N., *Atmos. Environ.* **2005**, *39*, 3421-3429.
38. Bailey, R.; Claxton, R.; Jones, L.; Kilroy, E.; Misselbrook, T.; Pang, Y.; Passant, N.; Salisbury, E.; Smith, H.; Thistlethwaite, G.; Wakeling, D.; Walker, C. *Air quality pollutant inventories for England, Scotland, Wales and Northern Ireland: 1990-2014*; Ricardo Energy & Environment/R/3463; **2016**.
39. Vascellari, M., NO_x Emission and Mitigation Technologies. In *Handbook of Clean Energy Systems*, Yan, J., Ed. John Wiley & Sons: **2015**; Vol. 3, pp 1605-1628.
40. Wang, S. X.; Zhao, B.; Cai, S. Y.; Klimont, Z.; Nielsen, C. P.; Morikawa, T.; Woo, J. H.; Kim, Y.; Fu, X.; Xu, J. Y.; Hao, J. M.; He, K. B., *Atmos. Chem. Phys.* **2014**, *14*, 6571-6603.
41. Yeh, J. T.; Chen, W.-Y., *Control of NO_x during stationary combustion*. Humana Press Inc.: **2005**; Vol. 2, p 113-126.
42. Hoekman, S. K.; Robbins, C., *Fuel Process. Technol.* **2012**, *96*, 237-249.
43. Rosenberg, H. S.; Curran, L. M.; Slack, A. V.; Ando, J.; Oxley, J. H., *Prog. Energy Combust. Sci.* **1980**, *6*, 287-302.
44. Harrison, B.; Diwell, A. F.; Wyatt, M., *Platinum Met. Rev.* **1985**, *29*, 50-6.
45. Granger, P.; Parvulescu, V. I., *Chem. Rev.* **2011**, *111*, 3155-3207.
46. Corcoran, T., How does a hybrid car work? **2016**.
47. Nakajima, F.; Hamada, I., *Catal. Today* **1996**, *29*, 109-115.
48. Koebel, M.; Elsener, M.; Madia, G., *Ind. Eng. Chem. Res.* **2001**, *40*, 52-59.
49. Forzatti, P.; Lietti, L., *Chim. Ind. (Milan)* **1996**, *78*, 685-691.
50. Chen, L.; Li, J.; Ge, M., *J. Phys. Chem. C* **2009**, *113*, 21177-21184.
51. Nova, I.; Lietti, L.; Tronconi, E.; Forzatti, P., *Catal. Today* **2000**, *60*, 73-82.
52. Forzatti, P.; Nova, I.; Tronconi, E.; Kustov, A.; Thøgersen, J. R., *Catal. Today* **2012**, *184*, 153-159.
53. Ma, Z.; Wu, X.; Feng, Y.; Si, Z.; Weng, D.; Shi, L., *Prog. Nat. Sci. Mater. Int.* **2015**, *25*, 342-352.

54. Shan, W.; Song, H., *Catal. Sci. Technol.* **2015**, *5*, 4280-4288.
55. Qi, G.; Yang, R. T., *Chem. Commun.* **2003**, 848-849.
56. Chang, H.; Chen, X.; Li, J.; Ma, L.; Wang, C.; Liu, C.; Schwank, J. W.; Hao, J., *Environ. Sci. Technol.* **2013**, *47*, 5294-5301.
57. Liu, Z.; Zhu, J.; Li, J.; Ma, L.; Woo, S. I., *ACS Appl. Mater. Interfaces* **2014**, *6*, 14500-14508.
58. Xu, L.; Shi, C.; Zhang, Z.; Gies, H.; Xiao, F.-S.; De Vos, D.; Yokoi, T.; Bao, X.; Feyen, M.; Maurer, S.; Yilmaz, B.; Müller, U.; Zhang, W., *Microporous Mesoporous Mater.* **2014**, *200*, 304-310.
59. Zhu, L.; Zhang, L.; Qu, H.; Zhong, Q., *J. Mol. Catal. A: Chem.* **2015**, *409*, 207-215.
60. Chen, P.; Simboeck, J.; Schoenebaum, S.; Rauch, D.; Simons, T.; Palkovits, R.; Moos, R.; Simon, U., *Sens. Actuators, B* **2016**, *236*, 1075-1082.
61. Jangjou, Y.; Wang, D.; Kumar, A.; Li, J.; Epling, W. S., *ACS Catal.* **2016**, *6*, 6612-6622.
62. Leistner, K.; Olsson, L., *Appl. Catal., B* **2015**, *165*, 192-199.
63. Tang, X.; Li, J.; Sun, L.; Hao, J., *Appl. Catal., B* **2010**, *99*, 156-162.
64. Tang, X.; Hao, J.; Xu, W.; Li, J., *Catal. Commun.* **2007**, *8*, 329-334.
65. Xiao, X.; Sheng, Z.; Yang, L.; Dong, F., *Catal. Sci. Technol.* **2016**, *6*, 1507-1514.
66. Zuo, J.; Chen, Z.; Wang, F.; Yu, Y.; Wang, L.; Li, X., *Ind. Eng. Chem. Res.* **2014**, *53*, 2647-2655.
67. Zhang, P.; Sun, Y.; Su, W.; Wei, Y.; Liu, J., *RSC Adv.* **2016**, *6*, 107270-107277.
68. Mu, W.; Zhu, J.; Zhang, S.; Guo, Y.; Su, L.; Li, X.; Li, Z., *Catal. Sci. Technol.* **2016**, Ahead of Print.
69. Shen, B.; Wang, Y.; Wang, F.; Liu, T., *Chem. Eng. J.* **2014**, *236*, 171-180.
70. Guo, R.-T.; Zhen, W.-L.; Zhou, Y.; Pan, W. G.; Xu, H.-J.; Jin, Q.; Ding, C.-G.; Guo, S.-Y., *Asian J. Chem.* **2014**, *26*, 407-410.
71. Lian, Z.; Liu, F.; He, H., *Ind. Eng. Chem. Res.* **2014**, *53*, 19506-19511.
72. Gao, X.; Jiang, Y.; Zhong, Y.; Luo, Z.; Cen, K., *J. Hazard. Mater.* **2010**, *174*, 734-739.
73. Shan, W.; Liu, F.; He, H.; Shi, X.; Zhang, C., *Catal. Today* **2012**, *184*, 160-165.
74. Li, P.; Xin, Y.; Li, Q.; Wang, Z.; Zhang, Z.; Zheng, L., *Environ. Sci. Technol.* **2012**, *46*, 9600-9605.
75. Lian, Z.; Liu, F.; He, H.; Liu, K., *RSC Adv.* **2015**, *5*, 37675-37681.
76. Deng, Y.; Chen, X.; Shao, R.; Hu, L.; Tang, J.; Wang, C., *Key Eng. Mater.* **2016**, *697*, 275-278.
77. Gan, L.; Guo, F.; Yu, J.; Xu, G., *Catalysts* **2016**, *6*, 25.
78. Marberger, A.; Elsener, M.; Ferri, D.; Krocher, O., *Catalysts* **2015**, *5*, 1704-1720.
79. Yashima, M., Crystal and electronic structures, structural disorder, phase transformation, and phase diagram of ceria-zirconia and ceria-based materials. In

Catalysis by Ceria and Related Materials, 2nd ed.; Trovarelli, A.; Fornasiero, P., Eds. Imperial College Press: **2013**.

80. Sun, C.; Li, H.; Chen, L., *Energy Environ. Sci.*, **2012**, 5, 8475-8505.
81. Lietti, L., *Appl. Catal., B* **1996**, 10, 281-297.
82. Vanpoucke, D. E. P. Investigation of tunable buffer layers for coated superconductors: from solid state physics to quantum chemistry. Doctoral degree, Ghent University, Ghent, Belgium, **2012**.
83. Trovarelli, A.; Zamar, F.; Llorca, J.; Leitenburg, C. d.; Dolcetti, G.; Kiss, J. T., *J. Catal.* **1997**, 169, 490-502.
84. Dutta, G.; Waghmare, U. V.; Baidya, T.; Hegde, M. S.; Priolkar, K. R.; Sarode, P. R., *Chem. Mater.* **2006**, 18, 3249-3256.
85. Reddy, B. M.; Reddy, G. K.; Ganesh, I.; Ferreira, J. M. F., *J. Mater. Sci.* **2009**, 44, 2743-2751.
86. McFarland, E. W.; Metiu, H., *Chem. Rev.* **2013**, 113, 4391-4427.
87. Hori, C. E.; Permana, H.; Ng, K. Y. S.; Brenner, A.; More, K.; Rahmoeller, K. M.; Belton, D., *Appl. Catal., B* **1998**, 16, 105-117.
88. Bonk, A.; Remhof, A.; Maier, A. C.; Trottman, M.; Schlupp, M. V. F.; Battaglia, C.; Vogt, U. F., *J. Phys. Chem. C* **2016**, 120, 118-125.
89. Xu, L.; Li, X.-S.; Crocker, M.; Zhang, Z.-S.; Zhu, A.-M.; Shi, C., *J. Mol. Catal. A: Chem.* **2013**, 378, 82-90.
90. Zhang, Q.-L.; Qiu, C.-T.; Xu, H.-D.; Lin, T.; Lin, Z.-E.; Gong, M.-C.; Chen, Y.-Q., *Catal. Today* **2011**, 175, 171-176.
91. Xiong, Y.; Tang, C.; Yao, X.; Zhang, L.; Li, L.; Wang, X.; Deng, Y.; Gao, F.; Dong, L., *Appl. Catal., A* **2015**, 495, 206-216.
92. Vuurman, M. A.; Wachs, I. E., *J. Phys. Chem.* **1992**, 96, 5008-5016.
93. Martinez-Huerta, M. V.; Deo, G.; Fierro, J. L. G.; Banares, M. A., *J. Phys. Chem. C* **2007**, 111, 18708-18714.
94. Wu, Z.; Rondinone, A. J.; Ivanov, I. N.; Overbury, S. H., *J. Phys. Chem. C* **2011**, 115, 25368-25378.
95. Li, Y.; Wei, Z.; Gao, F.; Kovarik, L.; Peden, C. H. F.; Wang, Y., *J. Catal.* **2014**, 315, 15-24.
96. Weckhuysen, B. M.; Keller, D. E., *Catal. Today* **2003**, 78, 25-46.
97. Abbott, H. L.; Uhl, A.; Baron, M.; Lei, Y.; Meyer, R. J.; Stacchiola, D. J.; Bondarchuk, O.; Shaikhutdinov, S.; Freund, H. J., *J. Catal.* **2010**, 272, 82-91.
98. Keller, D. E. X-ray absorption spectroscopy of supported vanadium oxide catalysts. Doctoral degree, Utrecht University, Utrecht University, **2006**.
99. Janssen, F. J. J. G.; Van den Kerkhof, F. M. G.; Bosch, H.; Ross, J. R. H., *J. Phys. Chem.* **1987**, 91, 5921-5927.
100. Went, G. T.; Leu, L.-J.; Rosin, R. R.; Bell, A. T., *J. Catal.* **1992**, 134, 492-505.
101. Lietti, L.; Alemany, J. L.; Forzatti, P.; Busca, G.; Ramis, G.; Giamello, E.; Bregani, F., *Catal. Today* **1996**, 29, 143-148.
102. Forzatti, P., *Appl. Catal., A* **2001**, 222, 221-236.
103. Alemany, L. J.; Lietti, L.; Ferlazzo, N.; Forzatti, P.; Busca, G.; Giamello, E.; Bregani, F., *J. Catal.* **1995**, 155, 117-30.

104. Amores, J. M. G.; Escribano, V. S.; Busca, G., *J. Mater. Chem.* **1995**, *5*, 1245-1249.
105. Baron, M.; Abbott, H.; Bondarchuk, O.; Stacchiola, D.; Uhl, A.; Shaikhutdinov, S.; Freund, H.-J.; Popa, C.; Ganduglia-Pirovano, M. V.; Sauer, J., *Angew. Chem. Int. Ed.* **2009**, *48*, 8006-8009.
106. Ganduglia-Pirovano, M. V.; Popa, C.; Sauer, J.; Abbott, H.; Uhl, A.; Baron, M.; Stacchiola, D.; Bondarchuk, O.; Shaikhutdinov, S.; Freund, H.-J., *J. Am. Chem. Soc.*, **2010**, *132*, 2345-2349.
107. Wu, Z.; Li, M.; Overbury, S. H., *ChemCatChem* **2012**, *4*, 1653-1661.
108. Daniell, W.; Ponchel, A.; Kuba, S.; Anderle, F.; Weingand, T.; Gregory, D. H.; Knözinger, H., *Top. Catal.* **2002**, *20*, 65-74.
109. He, Y.; Ford, M. E.; Zhu, M.; Liu, Q.; Tumuluri, U.; Wu, Z.; Wachs, I. E., *Appl. Catal., B* **2016**, *193*, 141-150.
110. Dumesic, J. A.; Topsøe, N. Y.; Topsøe, H.; Chen, Y.; Slabiak, T., *J. Catal.* **1996**, *163*, 409-417.
111. Nova, I.; Ciardelli, C.; Tronconi, E.; Chatterjee, D.; Bandl-Konrad, B., *AIChE J.* **2006**, *52*, 3222-3233.
112. Gasior, M.; Haber, J.; Machej, T.; Czeppe, T., *J. Mol. Catal.* **1988**, *43*, 359-369.
113. Efsthathiou, A. M.; Fliatoura, K., *Appl. Catal., B* **1995**, *6*, 35-59.
114. Busca, G.; Martra, G.; Zecchina, A., *Catal. Today* **2000**, *56*, 361-370.
115. Zhao, W.; Zhong, Q.; Pan, Y.; Zhang, R., *Chem. Eng. J.* **2013**, *228*, 815-823.
116. Busca, G., *Physi. Chem. Chem. Phys.* **1999**, *1*, 723-736.
117. Lietti, L.; Forzatti, P.; Berti, F., *Catal. Lett.* **1996**, *41*, 35-39.
118. Tronconi, E.; Nova, I.; Ciardelli, C.; Chatterjee, D.; Weibel, M., *J. Catal.* **2006**, *245*, 1-10.
119. Nova, I.; Ciardelli, C.; Tronconi, E.; Chatterjee, D.; Weibel, M., *AIChE J.* **2009**, *55*, 1514-1529.
120. Beck, B.; Harth, M.; Hamilton, N. G.; Carrero, C.; Uhlrich, J. J.; Trunschke, A.; Shaikhutdinov, S.; Schubert, H.; Freund, H.-J.; Schlögl, R.; Sauer, J.; Schomäcker, R., *J. Catal.* **2012**, *296*, 120-131.
121. Artiglia, L.; Agnoli, S.; Granozzi, G., *Coord. Chem. Rev.* **2015**, *301-302*, 106-122.
122. Lietti, L.; Forzatti, P., *J. Catal.* **1994**, *147*, 241-249.
123. Huang, B.; Huang, R.; Jin, D.; Ye, D., *Catal. Today* **2007**, *126*, 279-283.
124. Pham, P. T. M.; Le, M. T.; Nguyen, T. T.; Driessche, I. V., *Materials* **2014**, 7379-7397.
125. Monte, R. D.; Fornasiero, P.; Stefano Desinan, S.; Kas̆par, J., *Chem. Mater.* **2004**, *16*, 4273-4285.
126. Vélez, R. P. Structural characterization of iron species in Fe-ZSM-5 catalysts and the elucidation of their role in the mechanism. Doctoral degree, University of Rostock, **2014**.
127. Birkholz, M., *Thin film analysis by X-ray scattering*. Wiley-VCH, Weinheim: **2005**.

128. Speakman, S. A., Estimating Crystallite Size Using XRD. MIT center for materials science and Engineering: **2009**.
129. Langford, J. I.; Wilson, A. J. C., *J. Appl. Crystallogr.* **1978**, *11*, 102-113.
130. Ross, J. R. H., *Heterogeneous Catalysis: Fundamentals and Applications*. Elsevier: **2011**; p 36-42.
131. Sing, K. S. W.; Everett, D. H.; Haul, R. A. W.; Moscou, L.; Pierotti, R. A.; Rouquerol, J.; Siemieniewska, T., *Pure Appl. Chem.* **1985**, *57*, 17.
132. Hou, X.; Jones, B. T., Inductively coupled plasma/ Optical emission spectrometry. In *Encyclopedia of Analytical Chemistry*, Meyers, R. A., Ed. John Wiley & Sons Ltd: Chichester, **2000**; pp 9468-9485.
133. Venezia, A. M., *Catal. Today* **2003**, *77*, 359-370.
134. Eaton, G. R.; Eaton, S. S.; Barr, D. P.; Weber, R. T., *Quantitative EPR*. Springer-Verlag/Wien: **2010**.
135. Brückner, A., Electron Paramagnetic Resonance. In *In-situ Spectroscopy of Catalysts*, Weckhuysen, B. M., Ed. American Scientific Publishers: **2004**; pp 219-252.
136. Davydov, A. A., *Molecular spectroscopy of oxide catalyst surfaces*. John Wiley & Son Ltd,: The Atrium, Southern Gate, Chichester, England, **2003**.
137. Schoonheydt, R. A., *Chem. Soc. Rev.* **2010**, *39*, 5051-5066.
138. Viezbicke, B. D.; Patel, S.; Davis, B. E.; Birnie, D. P., *phys. stat. sol. (b)* **2015**, *252*, n/a-n/a.
139. Choudhury, B.; Choudhury, A., *Mater. Chem. Phys.* **2012**, *131*, 666-671.
140. Channei, D.; Inceesungvorn, B.; Wetchakun, N.; Ukritnukun, S.; Nattestad, A.; Chen, J.; Phanichphant, S., *Sci. Rep.* **2014**, *4*, 5757.
141. Stuart, B., *Infrared Spectroscopy: Fundamentals and Applications*. John Wiley & Sons, Ltd: **2004**.
142. Bruno, T. J., *Appl. Spectrosc. Rev.* **1999**, *34*, 91-120.
143. Niemantsverdriet, J. W., *Spectroscopy in catalysis: An introduction*. VCH: VCH Verlagsgesellschaft, Weinheim, Germany, **1993**.
144. Reddy, B. M.; Bharali, P.; Saikia, P.; Park, S.-E.; van den Berg, M. W. E.; Muhler, M.; Grunert, W., *J. Phys. Chem. C* **2008**, *112*, 11729-11737.
145. Vuong, T. H.; Radnik, J.; Kondratenko, E.; Schneider, M.; Armbruster, U.; Brückner, A., *Appl. Catal., B* **2016**, 159-167.
146. Alifanti, M.; Baps, B.; Blangenois, N.; Naud, J.; Grange, P.; Delmon, B., *Chem. Mater.* **2003**, *15*, 395-403.
147. Bensalem, A.; Muller, J. C.; Bozon-Verduraz, F., *J. Chem. Soc. Faraday Trans.* **1992**, *88*, 153-154.
148. Moulder, J. F.; Stickle, W. F.; Sobol, P. E.; Bomben, K. D., *Handbook of x-ray photoelectron spectroscopy : a reference book of standard spectra for identification and interpretation of XPS data*. Eden Prairie, Minn. : Physical Electronics, c**1995**.: 1995.
149. Zhang, C.; Lin, J., *Phys. Chem. Chem. Phys.* **2011**, *13*, 3896-3905.
150. Bêche, E.; Charvin, P.; Perarnau, D.; Abanades, S.; Flamant, G., *Surf. Interface Anal.* **2008**, *40*, 264-267.

151. Biesinger, M. C.; Lau, L. W. M.; Gerson, A. R.; Smart, R. S. C., *Appl. Surf. Sci.* **2010**, *257*, 887-898.
152. Adamski, A.; Sojka, Z.; Dyrek, K.; Che, M., *Solid State Ionics* **1999**, *117*, 113-122.
153. Valentín, C.; Folgado, J. V.; Alarco'n, J., *Mater. Res. Bulletin* **2001**, *36*, 1615-1627.
154. CRC Handbook of Chemistry and Physics. Lide, D. R., Ed. CRC Press, Boca Raton, FL: **2005**.
155. Rybarczyk, P.; Berndt, H.; Radnik, J.; Pohl, M. M.; Buyevskaya, O.; Baerns, M.; Brückner, A., *J. Catal.* **2001**, *202*, 45-58.
156. Berndt, H.; Martin, A.; Brückner, A.; Schreier, E.; Müller, D.; Kosslick, H.; Wolf, G. U.; Lücke, B., *J. Catal.* **2000**, *191*, 384-400.
157. Khodakov, A.; Olthof, B.; Bell, A. T.; Iglesia, E., *J. Catal.* **1999**, *181*, 205-216.
158. Brückner, A., *Appl. Catal., A: Gen.* **2000**, *200*, 287-197.
159. Gao, X.; Wachs, I. E., *J. Phys. Chem. B* **2000**, *104*, 1261-1268.
160. Wang, X. J.; Li, H. D.; Fei, Y. J.; Wang, X.; Xiong, Y. Y.; Nie, Y. X.; Feng, K. A., *Appl. Surf. Sci.* **2001**, *177*, 8-14.
161. Matta, J.; Lamonier, J.-F.; Abi-Aad, E.; A. Zhilinskaya, E.; Aboukais, A., *Phys. Chem. Chem. Phys.* **1999**, *1*, 4975-4980.
162. Nowińska, K.; Więckowski, A. B., *Z. Phys. Chem. NF* **1989**, *162*, 231-244.
163. Gionco, C.; Paganini, M. C.; Giamello, E.; Burgess, R.; Di Valentin, C.; Pacchioni, G., *Chem. Mater.* **2013**, *25*, 2243-2253.
164. Ratnasamy, P.; Srinivas, D.; Satyanarayana, C. V. V.; Manikandan, P.; Senthil Kumaran, R. S.; Sachin, M.; Shetti, V. N., *J. Catal.* **2004**, *221*, 455-465.
165. Fierro, J. L. G.; Soria, J.; Sanz, J.; Rojo, J. M., *J. Solid State Chem.* **1987**, *66*, 154-162.
166. Abi-aad, E.; Bechara, R.; Grimblot, J.; Aboukais, A., *Chem. Mater.* **1993**, *5*, 793-797.
167. Schwartz, R. W.; Hill, N. J., *J. Chem. Soc. Faraday Trans.* **1974**, *70*, 124-131.
168. Kiel, A.; Mims, W. B., *Phys. Rev. B* **1972**, *6*, 34-39.
169. Havlíček, V.; Novák, P.; Vichr, M., *phys. stat. sol. (b)* **1971**, *44*, K21-K24.
170. Ball, D.; Wanklyn, B. M., *phys. stat. sol. (a)* **1976**, *36*, 307-316.
171. Topsøe, N. Y., *Cattech* **1997**, 125-134.
172. Bosch, H.; Janssen, F. J. J. G.; van den Kerkhof, F. M. G.; Oldenziel, J.; van Ommen, J. G.; Ross, J. R. H., *Appl. Catal.* **1986**, *25*, 239-248.
173. Jug, K.; Homann, T.; Bredow, T., *J. Phys. Chem. A* **2004**, *108*, 2966-2971.
174. Ovsitser, O.; Cherian, M.; Brueckner, A.; Kondratenko, E. V., *J. Catal.* **2009**, *265*, 8-18.
175. Brückner, A.; Kondratenko, E., *Catal. Today* **2006**, *113*, 16-24.
176. Weckhuysen, B. M.; Keller, D. E., *Catal. Today* **2003**, *78*, 25-46.
177. Risse, T.; Hollmann, D.; Bruckner, A., Chapter 1 In situ electron paramagnetic resonance (EPR) - a unique tool for analysing structure and reaction

- behaviour of paramagnetic sites in model and real catalysts. In *Catalysis: Vol. 27*, The Royal Society of Chemistry: **2015**; Vol. 27, pp 1-32.
178. McGarvey, B. R., *J. Phys. Chem.* **1967**, *71*, 51-66.
 179. Boucher, L. J.; Tynan, E. C.; Yen, T. F., *Electron Spin Resonance of Metal Complexes*. Plenum Press: New York, **1969**.
 180. Popa, C.; Ganduglia-Pirovano, M. V.; Sauer, J., *J. Phys. Chem. C* **2011**, *115*, 7399-7410.
 181. Beck, B.; Harth, M.; Hamilton, N. G.; Carrero, C.; Uhlrich, J. J.; Trunschke, A.; Shaikhutdinov, S.; Schubert, H.; Freund, H.-J.; Schlögl, R.; Sauer, J.; Schomäcker, R., *J. Catal.* **2012**, *296*, 120-131.
 182. Vuong, T. H.; Radnik, J.; Rabeah, J.; Bentrup, U.; Schneider, M.; Atia, H.; Armbruster, U.; Grünert, W.; Brückner, A., *ACS Catal.* **2017**, 1693-1705.
 183. Cha, W.; Ehrman, S. H.; Jurng, J., *J. Environ. Chem. Eng.* **2016**, *4*, 556-563.
 184. Wachs, I. E.; Deo, G.; Weckhuysen, B. M.; Andreini, A.; Vuurman, M. A.; Boer, M. d.; Amiridis, M. D., *J. Catal.* **1996**, *161*, 211-221.
 185. Yu, J.; Si, Z.; Zhu, M.; Wu, X.; Chen, L.; Weng, D.; Zou, J., *RSC Adv.* **2015**, *5*, 83594-83599.
 186. Watanabe, S.; Ma, X.; Song, C., *J. Phys. Chem. C* **2009**, *113*, 14249-14257.
 187. Reddy, B. M.; Khan, A.; Yamada, Y.; Kobayashi, T.; Loridant, S.; Volta, J.-C., *J. Phys. Chem. B* **2003**, *107*, 5162-5167.
 188. B. M. Reddy, P. L., A. Khan, *J. Phys. Chem. B* **2004**, *108*, 16855-16863.
 189. Bensalem, A.; Bozon-Verduraz, F.; Delamar, M.; Bugli, G., *Appl. Catal., A* **1995**, *121*, 81-93.
 190. Che, M.; Tench, A. J., Characterization and Reactivity of Molecular Oxygen Species on Oxide Surfaces. In *Advances in Catalysis*, D.D. Eley, H. P.; Paul, B. W., Eds. Academic Press: **1983**; Vol. Volume 32, pp 1-148.
 191. Gao, X.; Wachs, I. E., *J. Phys. Chem. B* **2000**, *104*, 1261-1268.
 192. Rodella, C. B.; Franco, R. W. A.; Magon, C. J.; Donoso, J. P.; Nunes, L. A. O.; Saeki, M. J.; Aegerter, M. A.; Sargentelli, V.; Florentino, A. O., *J. Sol-Gel Sci. Technol.* **2002**, *25*, 83-88.
 193. Inoue, F.; Ando, R. A.; Corio, P., *J. Raman Spectrosc.* **2011**, *42*, 1379-1383.
 194. Corma, A., *Chem. Rev.* **1995**, *95*, 559-614.
 195. Hughes, T. R.; White, H. M., *J. Phys. Chem.* **1967**, *71*, 2192-2201.
 196. Wu, Z.; Mann, A. K. P.; Li, M.; Overbury, S. H., *J. Phys. Chem. C* **2015**, *119*, 7340-7350.
 197. Lercher, J. A.; Gründling, C.; Eder-Mirth, G., *Catal. Today* **1996**, *27*, 353-376.
 198. Nowińska, K.; Więckowski, A. B., *Z. Phys. Chem. NF* **1989**, 231-244.
 199. McGarvey, B. R., *J. Phys. Chem.* **1967**, *71*, 51-66.
 200. *Nanostructured Photocatalysts: Advanced Functional Materials*. Springer International Publishing: Switzerland, **2016**.
 201. Centeno, M. A.; Carrizosa, I.; A. Odriozola, J., *Phys. Chem. Chem. Phys.* **1999**, *1*, 349-354.
 202. Gu, X.; Ge, J.; Zhang, H.; Auroux, A.; Shen, J., *Thermochim. Acta* **2006**, *451*, 84-93.

203. Ruggeri, M. P.; Nova, I.; Tronconi, E.; Pihl, J. A.; Toops, T. J.; Partridge, W. P., *Appl. Catal., B* **2015**, 166-167, 181-192.
204. Philipp, S.; Drochner, A.; Kunert, J.; Vogel, H.; Theis, J.; Lox, E. S., *Top. Catal.* **2004**, 30/31, 235-238.
205. Martinez-Arias, A.; Soria, J.; Conesa, J. C.; Seoane, X. L.; Arcoya, A.; Cataluna, R., *J. Chem. Soc., Faraday Trans.* **1995**, 91, 1679-1687.
206. Kantcheva, M., *J. Catal.* **2001**, 204, 479-494.
207. Azambre, B.; Zenbourny, L.; Koch, A.; Weber, J. V., *J. Phys. Chem. C* **2009**, 113, 13287-13299.
208. Ramis, G.; Busca, G.; Bregani, F.; Forzatti*, P., *Appl. Catal.* **1990**, 64, 259-278.
209. Brückner, A., *Catal. Rev.* **2003**, 45, 97-150.
210. Liu, C.; Gao, G.; Shi, J.-W.; He, C.; Li, G.; Bai, N.; Niu, C., *Catal. Commun.* **2016**, 86, 36-40.
211. Section 12: Properties of Solids In *CRC Handbook of Chemistry and Physics*, Lide, D. R., Ed. CRC Press, Boca Raton, FL: **2005**; pp 12-14-12-16.
212. Wang, Z.; Shen, G.; Li, J.; Liu, H.; Wang, Q.; Chen, Y., *Appl. Catal., B* **2013**, 138-139, 253-259.
213. Reddy, B. M.; Lakshmanan, P.; Khan, A., *J. Phys. Chem. B* **2004**, 108, 16855-16863.
214. Liu, L.; Yao, Z.; Liu, B.; Dong, L., *J. Catal.* **2010**, 275, 45-60.
215. Moreno, K. J.; Fuentes, A. F.; Maczka, M.; Hanuza, J.; Amador, U., *J. Solid State Chem.* **2006**, 179, 3805-3813.
216. Traqueia, L. S. M.; Pagnier, T.; Marques, F. M. B., *J. Eur. Ceram. Soc.* **1997**, 17, 1019-1026.
217. Boyero Macstre, J.; Fernández López, E.; Gallardo-Amores, J. M.; Ruano Casero, R.; Sánchez Escribano, V.; Pérez Bernal, E., *Int. J. Inorg. Mater.* **2001**, 3, 889-899.
218. Baldi, M.; Milella, F.; Manuel Gallardo-Amores, J.; Busca, G., *J. Mater. Chem.* **1998**, 8, 2525-2531.
219. Naccache, C.; Meriaudeau, P.; Che, M.; Tench, A. J., *Trans. Faraday Soc.* **1971**, 67, 506-512.
220. Coronado, J. M.; Javier Maira, A.; Martinez-Arias, A.; Conesa, J. C.; Soria, J., *J. Photochem. Photobiol., A* **2002**, 150, 213-221.
221. Yamazoe, S.; Teramura, K.; Hitomi, Y.; Shishido, T.; Tanaka, T., *J. Phys. Chem. C* **2007**, 111, 14189-14197.
222. Murugan, B.; Ramaswamy, A. V.; Srinivas, D.; Gopinath, C. S.; Ramaswamy, V., *Chem. Mater.* **2005**, 17, 3983-3993.
223. Lettenmayr, H.; Jantsch, W.; Palmetshofer, L., *Solid State Commun.* **1987**, 64, 1253-1255.
224. de Biasi, R. S.; Grillo, M. L. N., *J. Phys. Chem. Solids* **2003**, 64, 1365-1369.
225. Hadjiivanov, K. I., *Catal. Rev.* **2000**, 42, 71-144.
226. Bentrup, U.; Brückner, A.; Richter, M.; Fricke, R., *Appl. Catal., B* **2001**, 32, 229-241.

227. Hu, H.; Cai, S.; Li, H.; Huang, L.; Shi, L.; Zhang, D., *ACS Catal.* **2015**, *5*, 6069-6077.
228. García Pintos, D.; Juan, A.; Irigoyen, B., *J. Phys. Chem. C* **2013**, *117*, 18063-18073.
229. Hu, H.; Zha, K.; Li, H.; Shi, L.; Zhang, D., *Appl. Surf. Sci.* **2016**, *387*, 921-928.
230. Li, X.; Li, Y., *J. Mol. Catal. A: Chem.* **2014**, *386*, 69-77.
231. Savva, P. G.; Efstathiou, A. M., *J. Catal.* **2008**, *257*, 324-333.
232. Natile, M. M.; Boccaletti, G.; Glisenti, A., *Chem. Mater.* **2005**, *17*, 6272-6286.
233. Liu, J.; Li, Y.; Zhang, J.; He, D., *Appl. Catal., A* **2016**, 9-18.
234. Rebellato, J.; Natile, M. M.; Glisenti, A., *Appl. Catal., A* **2008**, *339*, 108-120.
235. Hirano, M.; Kato, E., *J Mater Sci Lett* **1996**, *15*, 1249-1250.
236. Djuričić, B.; Pickering, S., *J. Eur. Ceram. Soc.* **1999**, *19*, 1925-1934.
237. Bumajdad, A.; Eastoe, J.; Mathew, A., *Adv. Colloid Interfac. Sci.* **2009**, *147–148*, 56-66.
238. Li, L.; Zhan, Y.; Zheng, Q.; Zheng, Y.; Chen, C.; She, Y.; Lin, X.; Wei, K., *Catal. Lett.* **2009**, *130*, 532-540.
239. Yuejuan, W.; Jingmeng, M.; Mengfei, L.; Ping, F.; Mai, H., *J. Rare Earth* **2007**, *25*, 58-62.
240. Pérez Vélez, R.; Ellmers, I.; Huang, H.; Bentrup, U.; Schünemann, V.; Grünert, W.; Brückner, A., *J. Catal.* **2014**, *316*, 103-111.
241. Zhang, X.; Klabunde, K. J., *Inorg. Chem.* **1992**, *31*, 1706-1709.
242. Figaj, M.; Becker, K. D., *Solid State Ionics* **2001**, *141–142*, 507-512.
243. Oliva, C.; Termignone, G.; Vatti, F. P.; Forni, L.; Vishniakov, A. V., *J. Mater. Sci.* **1996**, *31*, 6333-6338.
244. Gideoni, M.; Steinberg, M., *J. Solid State Chem.* **1972**, *4*, 370-373.
245. Baker, J. M.; Hayes, W.; Jones, D. F., *Proc. Phys. Soc. (London)* **1959**, *73*, 4.

Appendix

Further analyses on the $V_2O_5/Ce_{1-x}Zr_xO_2$ catalysts from chapter 4

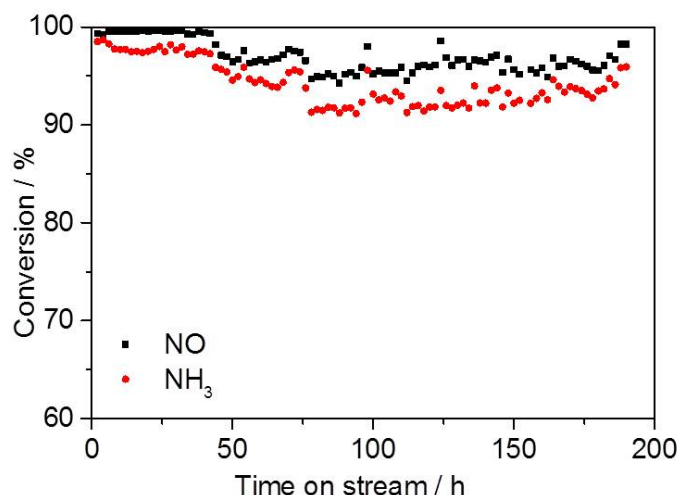


Figure A.1: NO and NH_3 conversion of 5% $V_2O_5/Ce_{0.3}Zr_{0.7}O_2$ at 250 °C as a function of time on stream. Feed composition: 0.1% NO, 0.1% NH_3 , 5% O_2/He , GHSV = 70,000 h^{-1} .

The Raman shift at 464.1 cm^{-1} is attributed to CeO_2 (F_{2g} mode). This peak shifted to 476.8 cm^{-1} and became weaker and broader after long-term NH_3 -SCR of NO_x , indicating less crystalline CeO_2 on the surface of the used catalyst. The V=O modes were observed at 702.1 and 995.8 cm^{-1} , which are attributed to crystalline V_2O_5 , increased after catalytic test. Moreover, a weak and broad feature at 845.4 cm^{-1} was observed on the used catalyst, which can be assigned to the Ce-O-V mode. No band at 864 cm^{-1} and 921 or 953 cm^{-1} of the $CeVO_4$ formation can be seen.

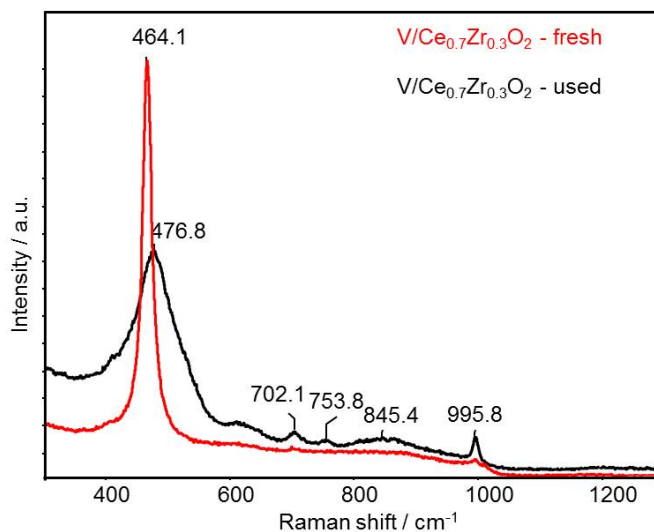


Figure A.2: Raman spectra of catalysts $V/Ce_{0.7}Zr_{0.3}O_2$ fresh (red) and used (black) for long-term NH_3 -SCR of NO_x catalytic test recorded at room temperature.

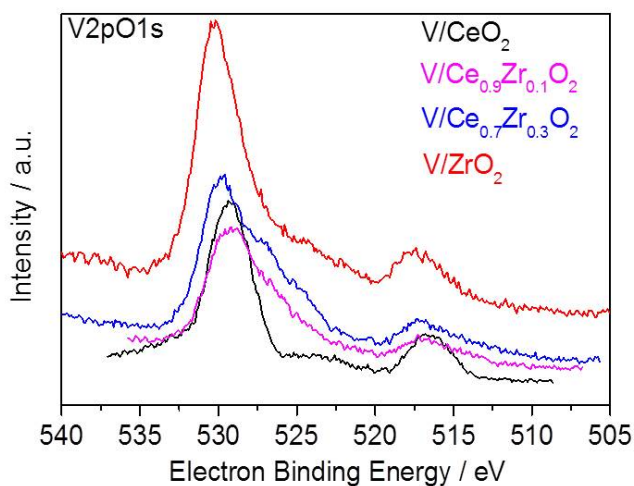


Figure A.3: XP spectra in the region of the O1s and V 2p peaks.

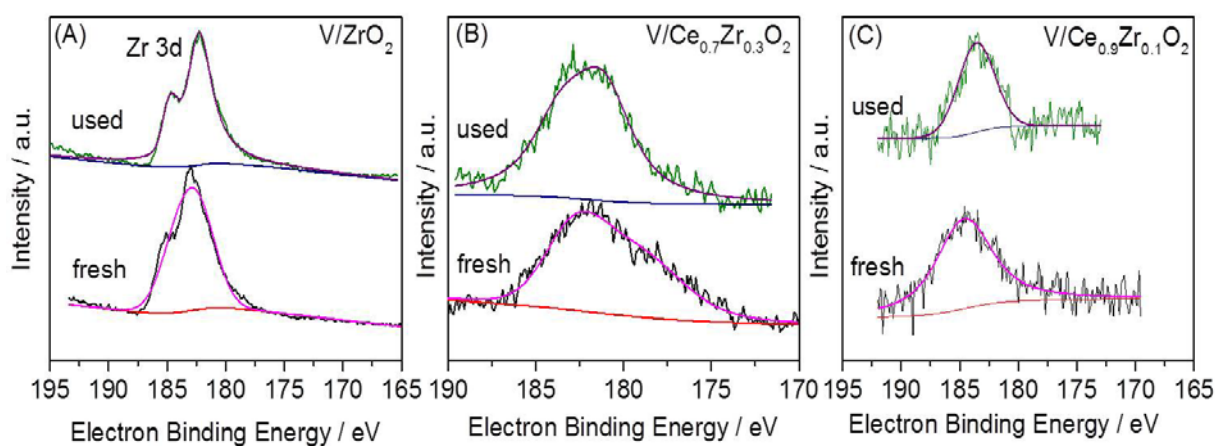


Figure A.4: XP spectra in the region of the Zr 3d peaks of V/ZrO₂ (A), V/Ce_{0.7}Zr_{0.3}O₂ (B), and V/Ce_{0.9}Zr_{0.1}O₂ (C).

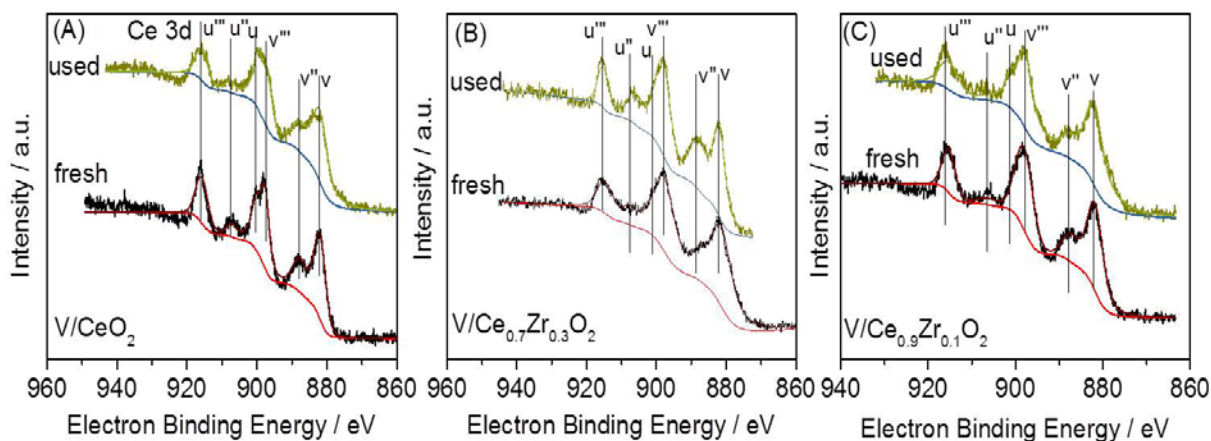


Figure A.5: XP spectra in the region of the Ce 3d peaks of V/CeO₂ (A), V/Ce_{0.7}Zr_{0.3}O₂ (B) and V/Ce_{0.9}Zr_{0.1}O₂ (C).

All Ce 3d spectra show the six features which are well-known for CeO₂. In agreement with the literature the peaks are labelled with v, v'', v''', u, u'' and u''' whereas v, v'' and v''' correspond to the 3d_{5/2} core holes, and u, u'' and u''' can be correlated to 3d_{3/2}. Especially u''' at 917 eV is characteristic for Ce (IV). The lowest binding energy of all spectra was between 882 and 883 eV which correspond to the value known for tetravalent Ce. Due to these observations, it must be concluded that Ce (IV) dominated in these samples. Hints for three valent Ce, for which a lowest 3d electron binding energy between 880 and 881 eV is expected, were not observed. The observed differences between the spectra can be explained by the different width of the subpeaks caused by a different degree of intermixing between the components, which leads to a different chemical heterogeneity in the neighbourhood of the Ce atoms.

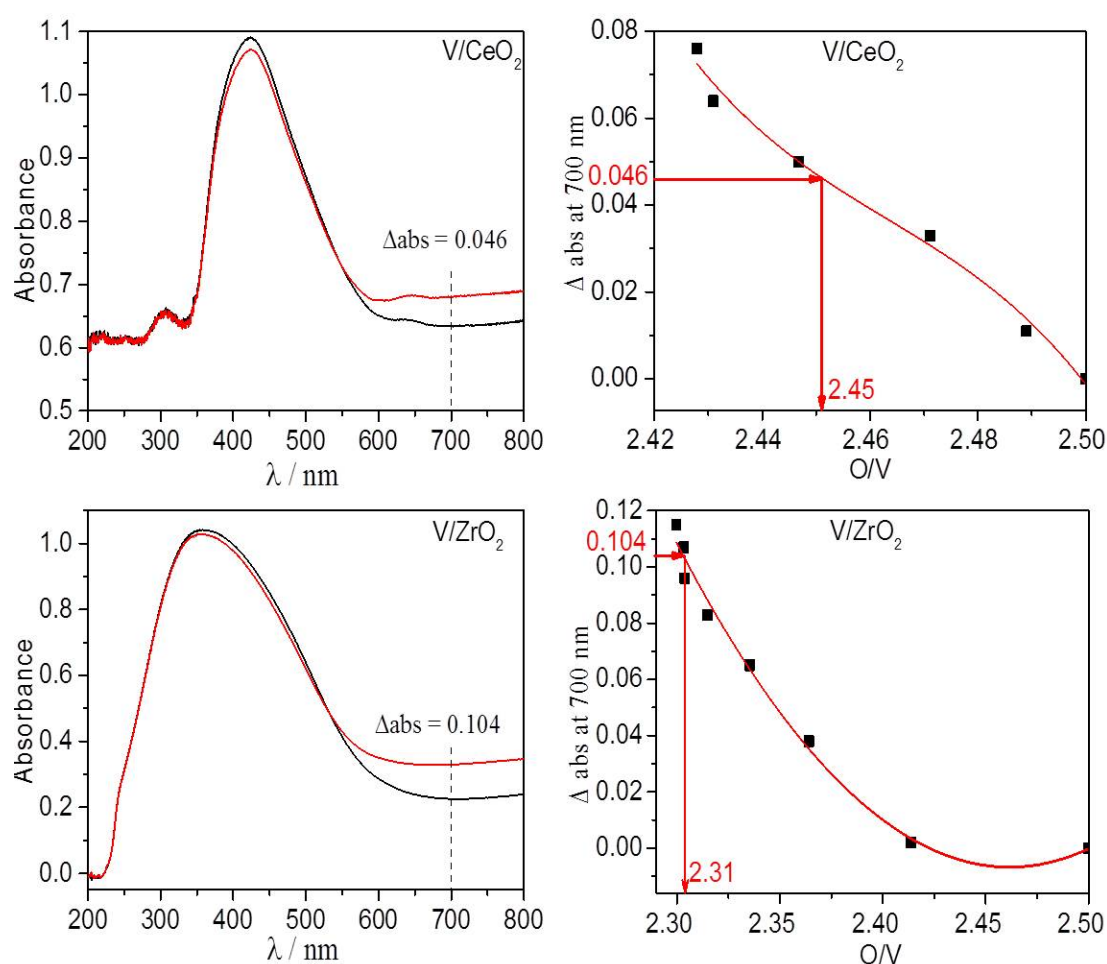


Figure A.6: Left column: UV-Vis spectra of catalysts V/CeO₂ and V/ZrO₂ recorded at 200 °C under air (black) and after 20 min switching to the total SCR feed flow. Right column: Corresponding calibration curves derived by simultaneous TPR/UV-Vis experiments.

Δabs (700 nm) values taken from the left spectra have been used to derive the O/V ratio from the calibration curves and from this the mean steady state V valence state.

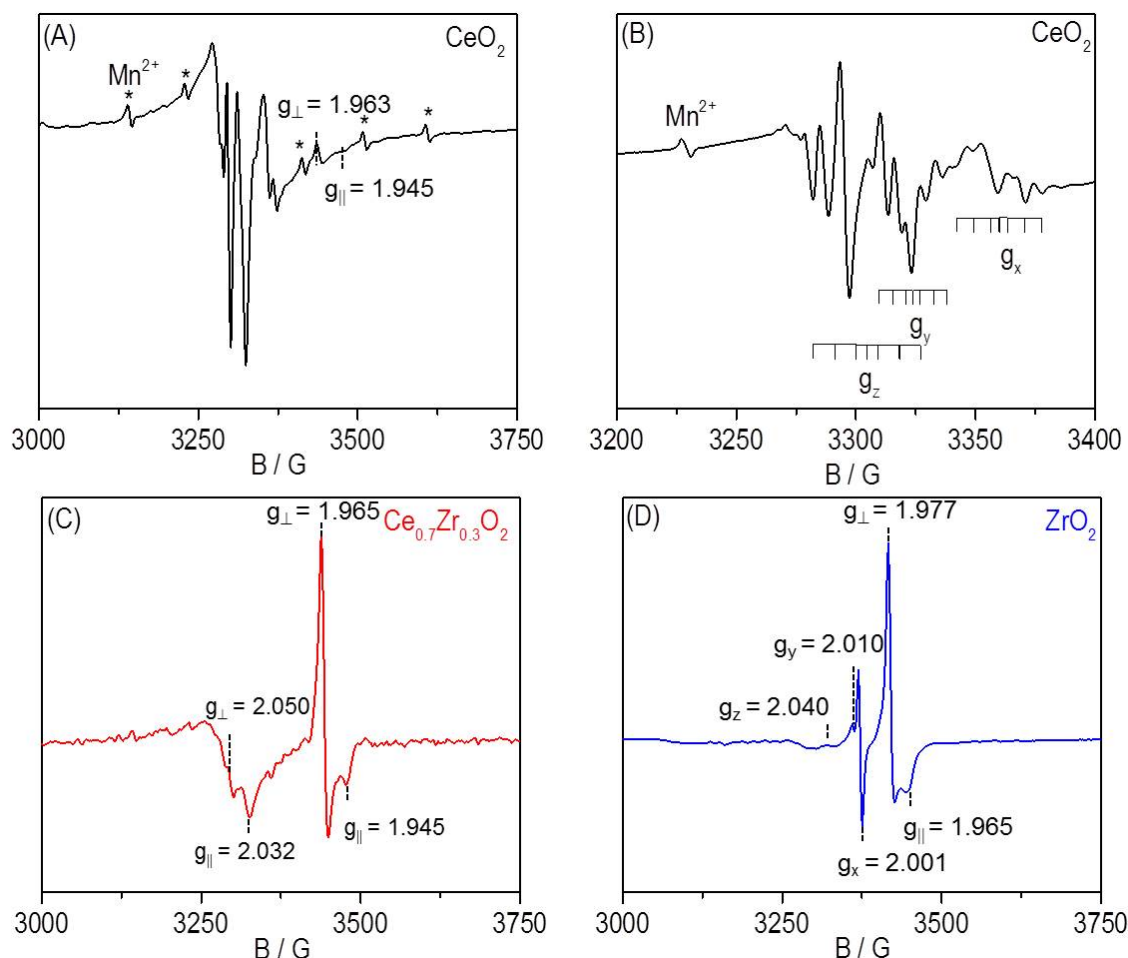


Figure A.7: EPR spectra of CeO_2 (A and B), $\text{Ce}_{0.7}\text{Zr}_{0.3}\text{O}_2$ (C) and ZrO_2 (D) recorded at 92 K.

The EPR spectra of CeO_2 (Figure A.7A) is complicated with three elements. The first part is exhibited 8 lines in the g range between 2.064 and 2.002 can be attributed to surface adsorbed O_2^- species, which were mentioned by several previously authors. To see clearly, the EPR spectra of CeO_2 (Figure A.7B) was recorded in the narrow range of field. In this case, the signal of O_2^- with $g_z = 2.049$, $g_y = 2.035$ and $g_x = 2.011$ exhibits a superhyperfine structure of $A_{zz} = 9.6$ G, $A_{yy} = 6.0$ G and $A_{xx} = 7.6$ G. This has been considered in some transition metal oxides when the formation of O_2^- is near a cation with delocalized unpaired electron spin. The second element with the parameters $g_{\text{iso}} = 2.000$ and $A_{\text{iso}} = 90.7$ G can be assigned to Mn^{2+} impurity. The last weak axial signal with $g_{\perp} = 1.963$ and $g_{\parallel} = 1.945$ has been occasionally assigned to Ce^{3+} . Moreover, due to short relaxation times,

Ce^{3+} is detectable only at low temperatures, usually below 77 K. Therefore, this signal should be from Cr^{3+} impurity or minor Zr^{3+} single sites.

The EPR spectra of ZrO_2 shows the signal with $g_z = 2.040$, $g_y = 2.010$ and $g_x = 2.001$ can be assigned to $\text{O}_2^- - \text{Zr}^{4+}$ and the signal with $g_{\perp} = 1.977$ and $g_{\parallel} = 1.965$ can be attributed to Zr^{3+} .

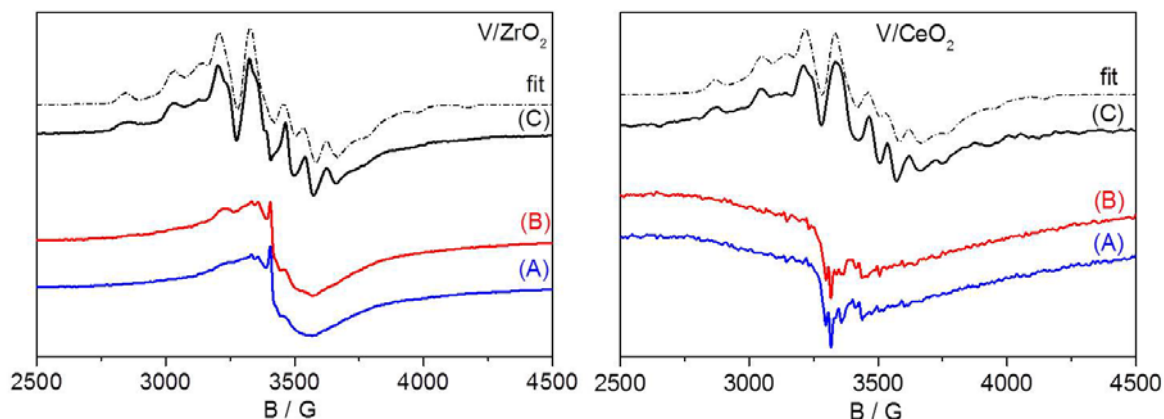


Figure A.8: *In-situ*-EPR spectra of V/ZrO_2 (left) and V/CeO_2 (right) recorded at 200 °C after (A) 1 h pretreatment in O_2 flow at 400 °C, (B) 30 min exposure to 0.1% NO , 5% O_2/He and (C) 30 min exposure to total SCR feed flow (spectrum B subtracted). Dashed line shows spectrum fitted with spin Hamiltonian parameters in Table 4.4.

Further analyses on the $\text{V}_2\text{O}_5/\text{Ce}_{1-x}\text{Ti}_x\text{O}_2$ catalysts from chapter 5

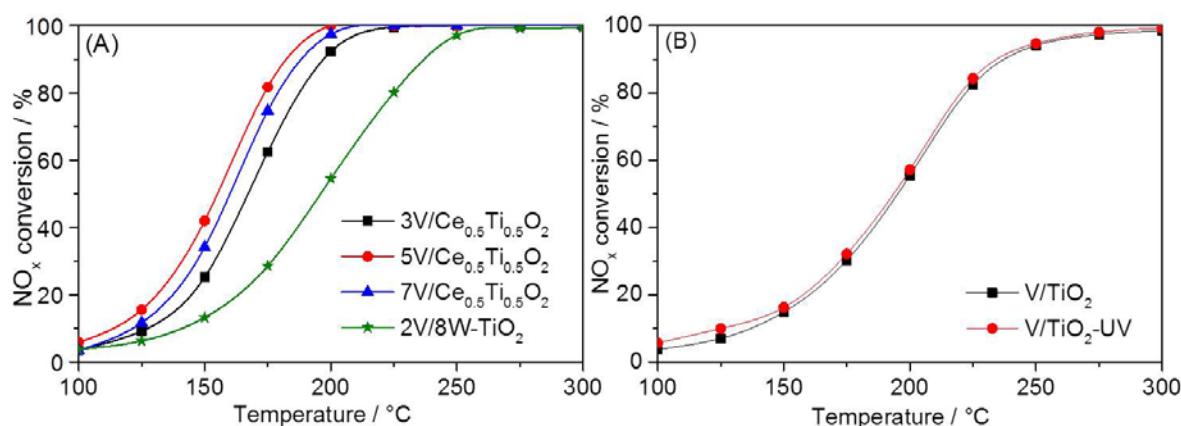


Figure A.9: NO_x conversion over (A): $\text{V}_2\text{O}_5/\text{Ce}_{0.5}\text{Ti}_{0.5}\text{O}_2$ catalysts synthesized with 3, 5 and 7 wt.-% of V_2O_5 in comparison to a commercial 2% $\text{V}_2\text{O}_5/8\% \text{WO}_3\text{-TiO}_2$ catalyst (2V/8W-TiO₂) and (B): 5% V/TiO_2 ($S_{\text{BET}} = 18.6 \text{ m}^2\text{g}^{-1}$) and 5% $\text{V/TiO}_2\text{-UV}$ ($S_{\text{BET}} = 350 \text{ m}^2\text{g}^{-1}$) as a function of temperature. Feed composition: 0.1% NO , 0.1% NH_3 , 5% O_2/He , GHSV = 70,000 h^{-1} .

EPR spectra of fresh catalysts are shown in Figure A.11 together with the supports without vanadium. In the latter, weak EPR signals are detected, which might arise from paramagnetic oxygen defects such as O^{\bullet} and/or $O_2^{\bullet-}$ species in the range of $g = 2.06$ - 2.00 depending on the supports and minor impurity of Cr^{3+} ($g_{\perp} = 1.968$, $g_{\parallel} = 1.945$).^{190, 241-242} Several authors assigned the latter signals to Ce^{3+} or quasi-free electrons.^{166, 243, 244} This is, however, very unlikely since Ce^{3+} as a $4f^1$ ion is characterised by strong spin-orbit coupling leading to significant deviations of the g tensor components from the Landé factor ($g_e = 2.0023$). Thus, tetragonally distorted Ce^{3+} centres with $g_{\parallel} = 3.038$ and $g_{\perp} = 1.396$ and/or $g_{\parallel} = 0.725$ and $g_{\perp} = 2.402$ have been observed in crystalline solids with fluorite structure which has similar lattice constant of ceria.^{242, 245} Also, Ce^{3+} is detectable usually only at temperatures below -196 °C because of its short relaxation times. Additional lines with hyperfine structure (hfs) sextet observed in the Figure S3A were assigned to a Mn^{2+} impurity in ceria. The EPR spectra of V/TiO_2 contains a broad signal of VO^{2+} species around $g = 1.963$ (Figure A.11D). This result indicates the stabilisation of V^{4+} in Ti^{4+} bulk positions as XPS data suggest that V is close to V^{5+} state on the surface of this sample. In contrast, no significant VO^{2+} signal is seen in the EPR spectra of catalysts V/CeO_2 (Figure A.11A) $V/Ce_{0.7}Ti_{0.3}O_2$ (Figure A.11B), and $V/Ce_{0.5}Ti_{0.5}O_2$ (Figure A.11C), which is confirmed by high dispersion of surface V^{5+} of these samples determined from XPS results.

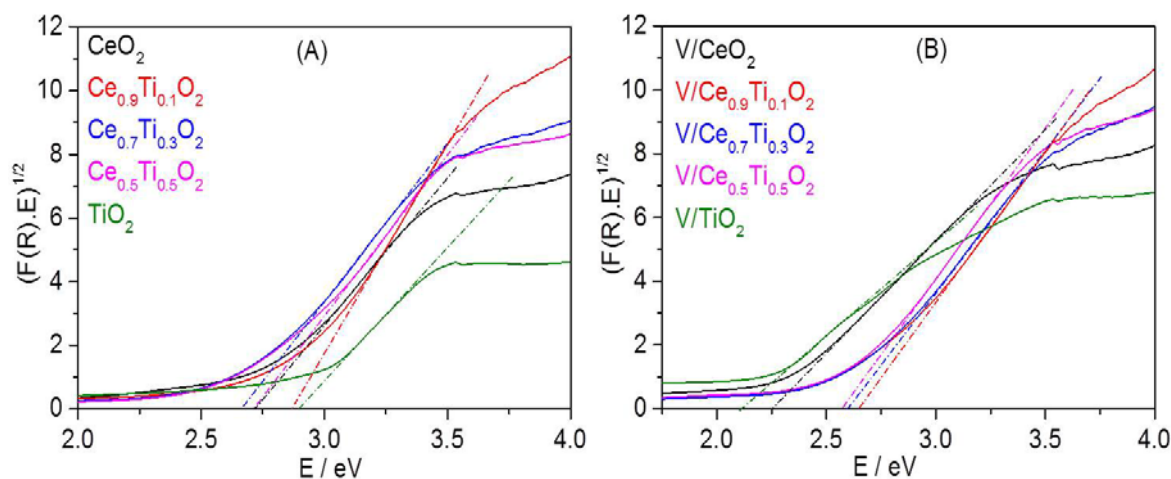


Figure A.12: Band gap estimation of supports $Ce_{1-x}Ti_xO_2$ (A) and catalysts $V/Ce_{1-x}Ti_xO_2$ (B) using Tauc's plot.

Table A.1: Relative amount of acidic sites, calculated by normalizing the band area at 1545 cm⁻¹ (Brønsted) and 1445 cm⁻¹ (Lewis) on the surface area, corresponding to Figure 5.6.

Sample	S _{BET} /m ² g ⁻¹	I _{Lewis}	I _{Lewis} /S _{BET}	I _{Brønsted}	I _{Brønsted} /S _{BET}
CeO ₂	61.2	0,67	0,011	-	-
TiO ₂	20.1	6.29	0,313	-	-
Ce _{0.5} Ti _{0.5} O ₂	113.5	2.61	0,023	-	-
V/CeO ₂	45.4	1.54	0,034	0.544	0,012
V/TiO ₂	18.6	0.37	0,020	0.911	0,049
V/Ce _{0.5} Ti _{0.5} O ₂	119.0	2.14	0,018	0.714	0,006

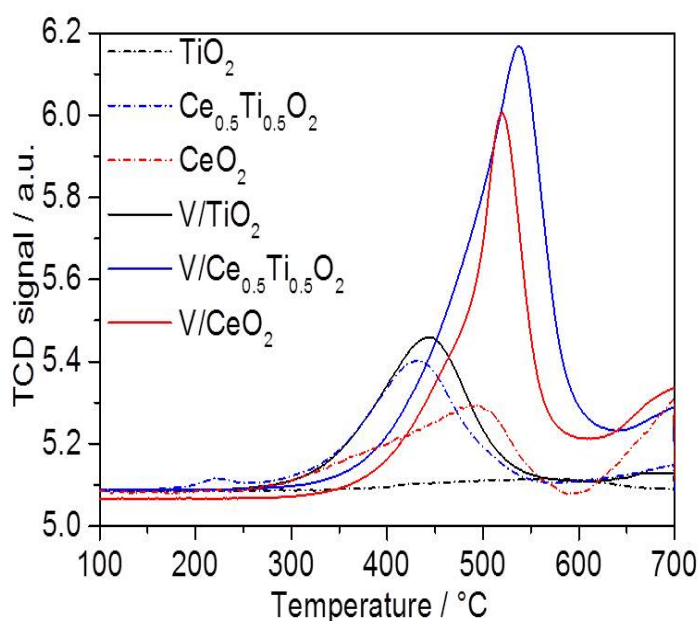


Table A.2: H₂ consumption derived from H₂-TPR experiments.

Sample	H ₂ consumption (μmol/g)
CeO ₂	855,67
TiO ₂	69,18
Ce _{0.5} Ti _{0.5} O ₂	1032,09
V/CeO ₂	1056,66
V/TiO ₂	572,00
V/Ce _{0.5} Ti _{0.5} O ₂	1587,54

Figure A.13: H₂-TPR profile of pure supports TiO₂, CeO₂, Ce_{0.5}Ti_{0.5}O₂, and vanadium containing catalysts V/TiO₂, V/CeO₂, and V/Ce_{0.5}Ti_{0.5}O₂.

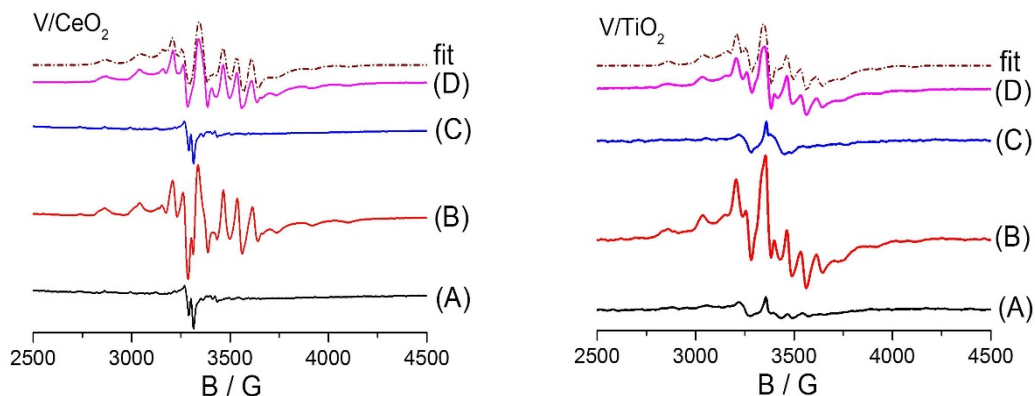


Figure A.14: *In-situ*-EPR spectra of V/CeO₂ and V/TiO₂ recorded at room temperature after (A) 1 h pretreatment in O₂ flow at 300 °C, (B) 30 min exposure to 0.1% NH₃/Ar (C) 30 min exposure to 0.1% NO, 5% O₂/Ar and (D) 30 min exposure to total SCR feed flow (spectrum fitted with spin Hamiltonian parameters in Table 5.3).

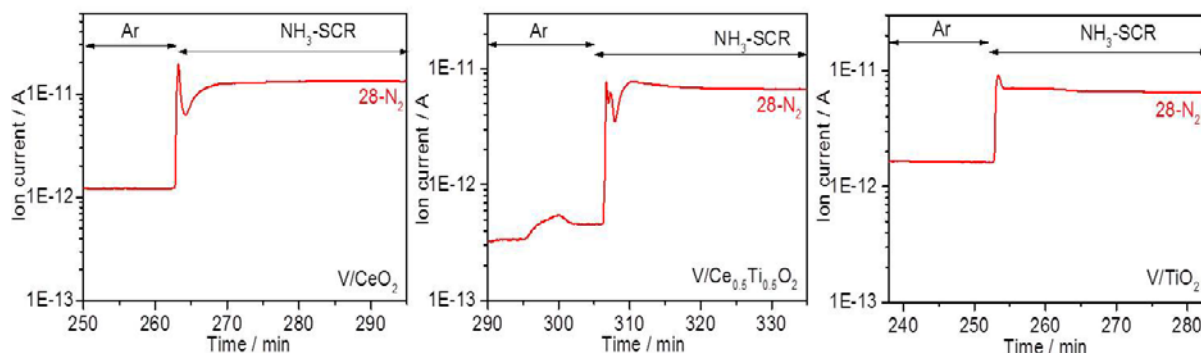


Figure A.15: N₂ formation detected by mass spectrometric analysis of the effluent gas stream during NH₃-SCR over 3 catalysts V/Ce_{1-x}Ti_xO₂ (x=0; 0.5; 1) at 200 °C, carried out parallel to the *operando* EPR measurements.

The MS signals of N₂ recorded parallel to the *operando* EPR spectra are shown in Figure A.15. The NO reduction increases in the order V/TiO₂ < V/CeO₂ < V/Ce_{0.5}Ti_{0.5}O₂, which agrees well with the activity tests over these catalysts. For the best catalyst V/Ce_{0.5}Ti_{0.5}O₂, after 30 min NO is almost completely converted to N₂ since the only trace of NO is detectable in the flow of Ar. Moreover, no N₂O was formed, indicating that 100% selectivity is achieved over these catalysts.

Figure A.16: Difference DRIFT spectra of bare supports: CeO_2 , $\text{Ce}_{0.5}\text{Ti}_{0.5}\text{O}_2$, TiO_2 and supported vanadium catalysts: V/CeO_2 , $\text{V}/\text{Ce}_{0.5}\text{Ti}_{0.5}\text{O}_2$, V/TiO_2 recorded at 200 °C after 45 min in 0.1% NH_3/He flow.

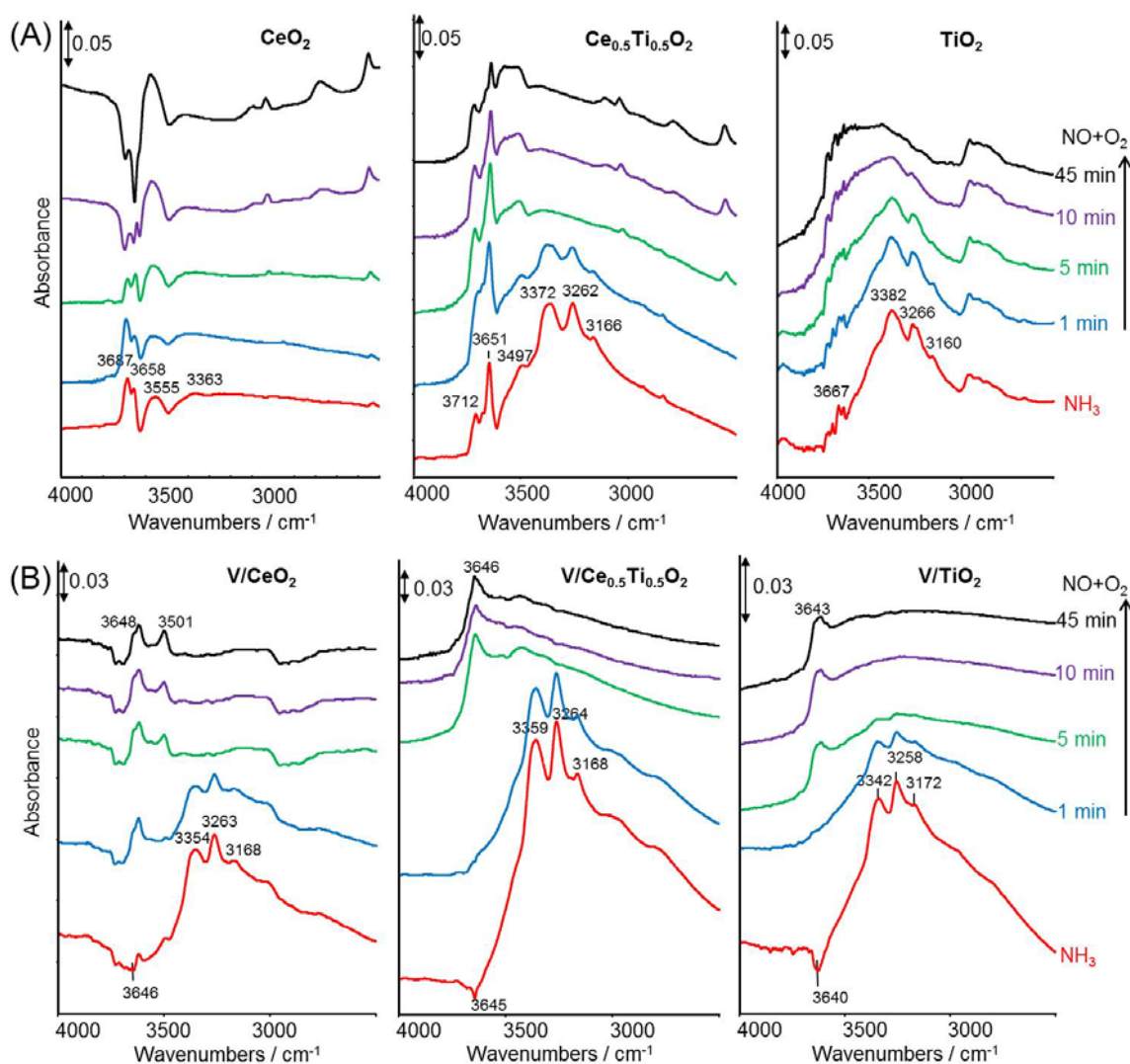
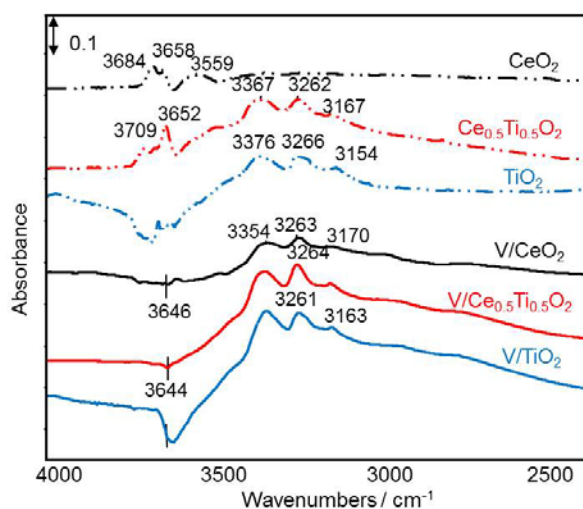


Figure A.17: Difference DRIFT spectra recorded at 200 °C under flowing 0.1% NO , 5% O_2/He of supports: CeO_2 , $\text{Ce}_{0.5}\text{Ti}_{0.5}\text{O}_2$, TiO_2 (A) and supported vanadium catalysts: V/CeO_2 , $\text{V}/\text{Ce}_{0.5}\text{Ti}_{0.5}\text{O}_2$, V/TiO_2 (B) (after pretreatment at 200 °C for 45 min in 0.1% NH_3/He flow).

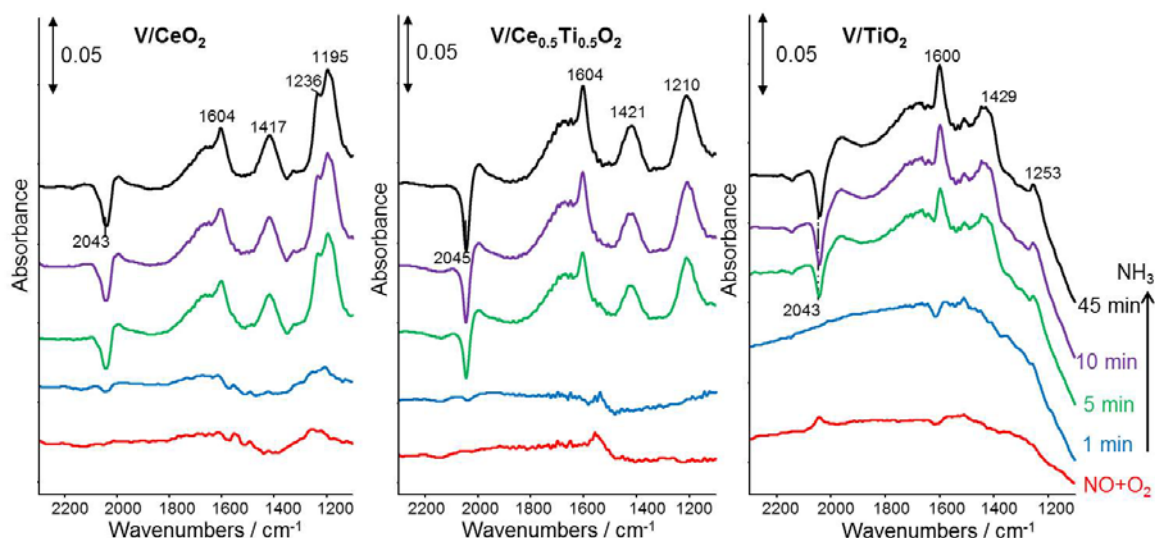


Figure A.18: Difference DRIFT spectra recorded at 200 °C under flowing 0.1% NH_3/He of supported vanadium catalysts: V/CeO_2 , $\text{V}/\text{Ce}_{0.5}\text{Ti}_{0.5}\text{O}_2$, V/TiO_2 (after pretreatment at 200 °C for 45 min in 0.1% NO , 5% O_2/He flow).

In-situ-DRIFTS of $\text{Ce}_{0.5}\text{Ti}_{0.5}\text{O}_2$ was performed as follows: 145 mg of particles (250–350 μm) were pretreated for 1 h at 300 °C in synthetic air and subsequently cooled to 23 °C under a flow of He for 30 min and then exposed to 0.1% NH_3/He flow and 0.1% NO , 5% O_2/He flow for 45 min each at 23 °C. Then the flow was switched to He and the sample was heated to 125 °C and kept at this temperature for 10 min. Background spectra were recorded in a flow of He and subtracted from the sample spectra for each measurement at the experiment temperature. The reaction cell was connected to a quadrupole mass spectrometer at the outlet for on-line product analysis.

Upon heating under He flow, the bands of adsorbed NH_3 above 3150 cm^{-1} and nitrate below 1600 cm^{-1} at 1550, 1437, and 1180 cm^{-1} disappeared (Figure A.19A & B). Simultaneously, the formation of N_2 was detected by on-line MS. This formation is a clear indication that both types of adsorbed species react with each other to form N_2 (Figure A.19C).

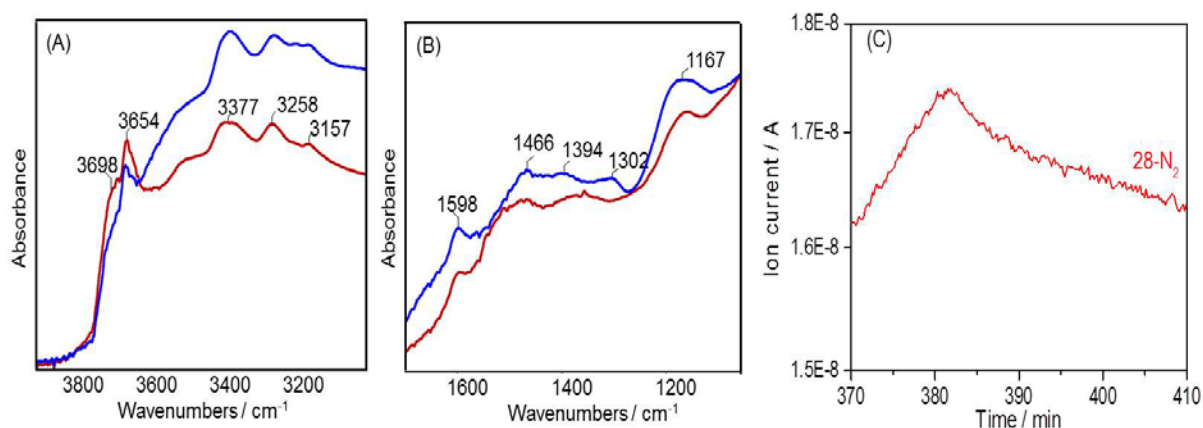


Figure A.19: DRIFT spectra of $\text{Ce}_{0.5}\text{Ti}_{0.5}\text{O}_2$ (A and B) recorded under flowing He after exposure to 0.1% NH_3/He flow for 45 min and subsequently to 0.1% NO , 5% O_2/He flow for 45 min at 23 °C (blue lines), followed by heating in He flow to 125 °C; (C) Corresponding on-line mass spectrometric analysis of N_2 during heating in He flow.

Further analyses on the $\text{V}_2\text{O}_5/\text{Ce}_{0.5}\text{Ti}_{0.5-x}\text{Mn}_x\text{O}_{2-\delta}$ catalysts from chapter 6

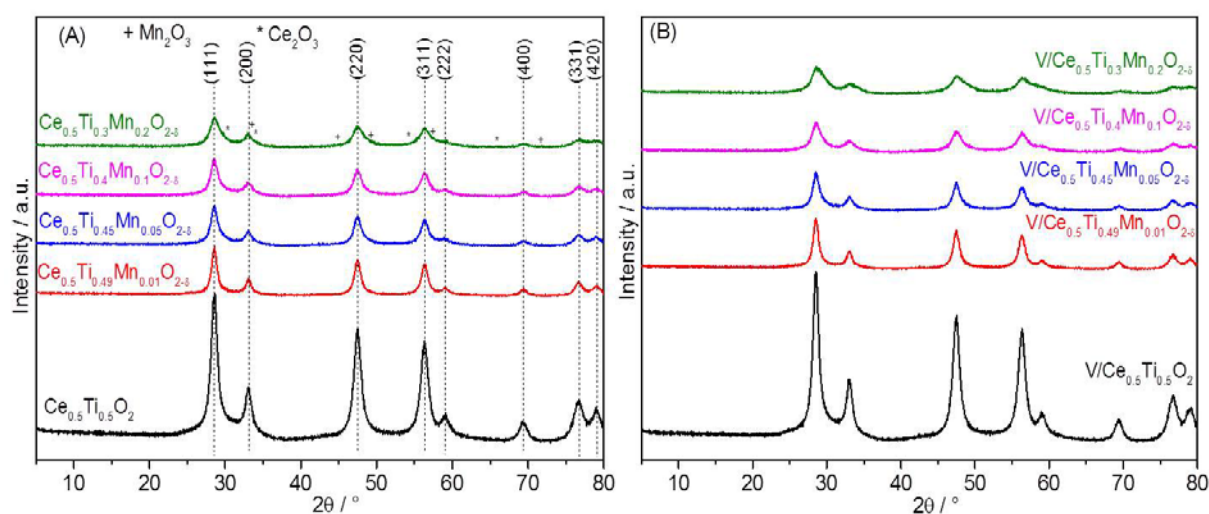


Figure A.20: X-ray diffraction patterns of pure supports $\text{Ce}_{0.5}\text{Ti}_{0.5-x}\text{Mn}_x\text{O}_{2-\delta}$ ($x = 0-0.2$) (A) and 5% $\text{V}_2\text{O}_5/\text{Ce}_{0.5}\text{Ti}_{0.5-x}\text{Mn}_x\text{O}_{2-\delta}$ catalysts (B).

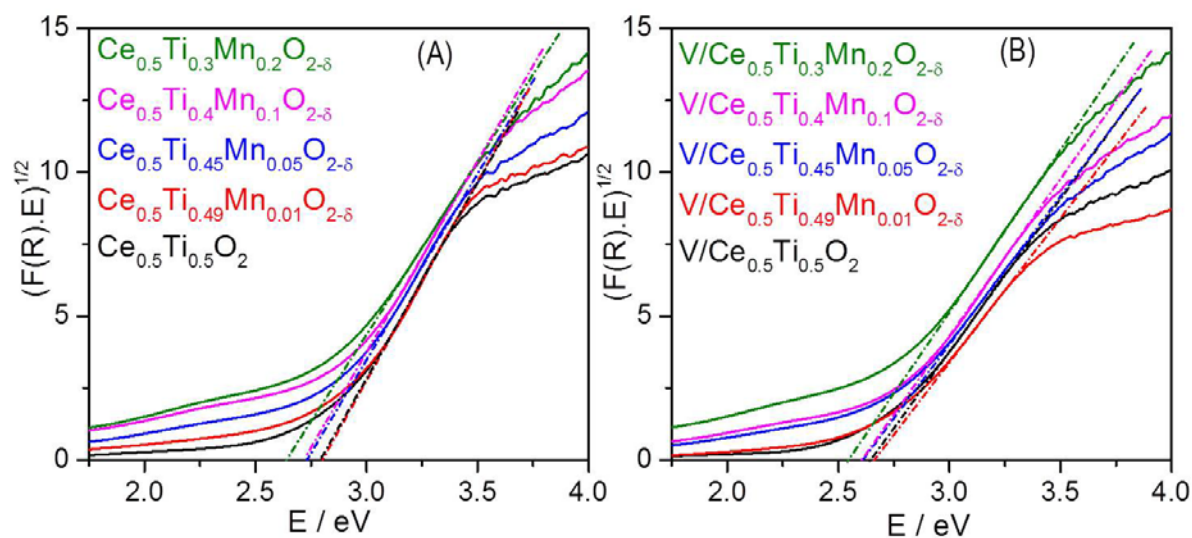


Figure A.21: Band gap estimation of supports $\text{Ce}_{0.5}\text{Ti}_{0.5-x}\text{Mn}_x\text{O}_{2-\delta}$ ($x = 0-0.2$) (A) and 5% $\text{V}_2\text{O}_5/\text{Ce}_{0.5}\text{Ti}_{0.5-x}\text{Mn}_x\text{O}_{2-\delta}$ catalysts (B) using Tauc's plot.

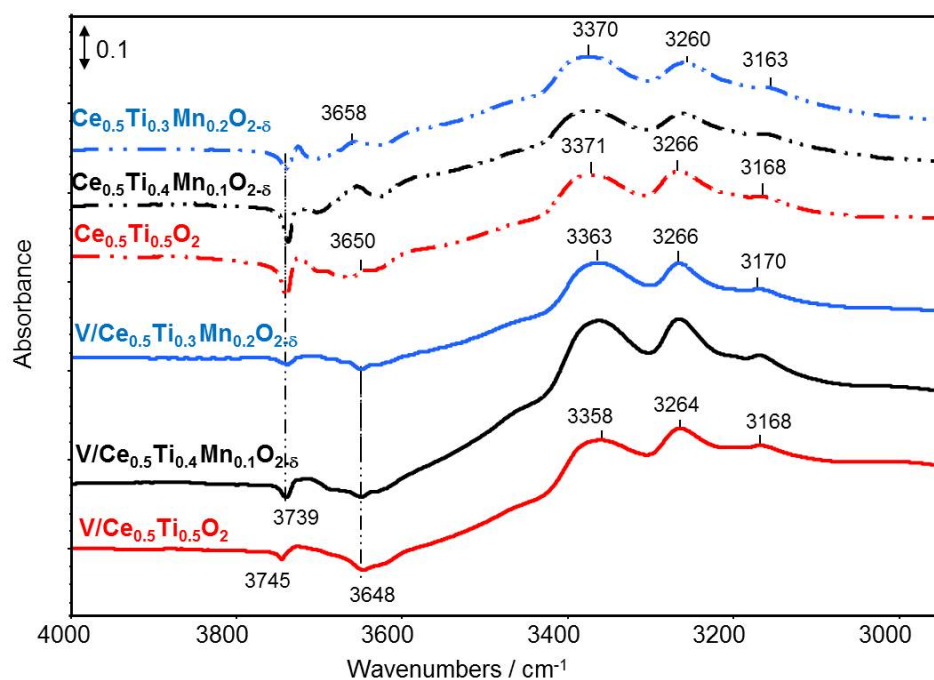


Figure A.22: Difference DRIFT spectra of bare supports $\text{Ce}_{0.5}\text{Ti}_{0.5-x}\text{Mn}_x\text{O}_{2-\delta}$ ($x = 0; 0.1; 0.2$) and 5% $\text{V}_2\text{O}_5/\text{Ce}_{0.5}\text{Ti}_{0.5-x}\text{Mn}_x\text{O}_{2-\delta}$ catalysts recorded at 175 °C after 45 min in 0.1% NH_3/He flow.

Further analyses on the VO_x/CeO_2 catalysts from chapter 7

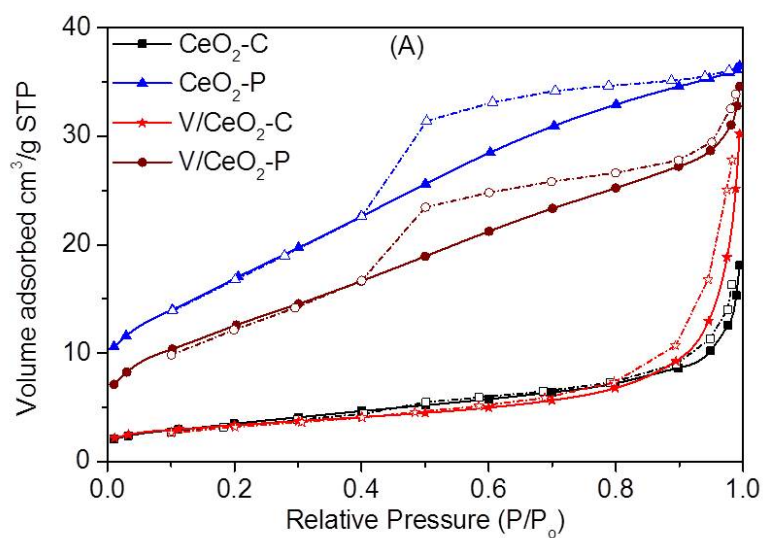


Figure A.23: N_2 adsorption (solid lines, filled symbols) and desorption isotherms (dashed lines, open symbols) of pure supports and catalysts.

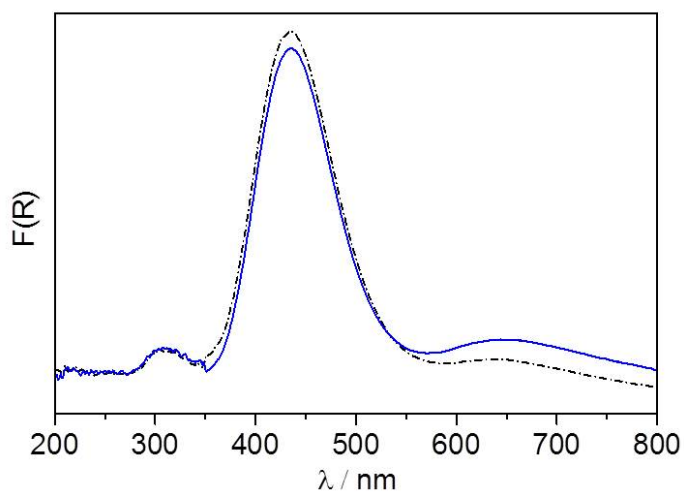


Figure A.24: *In-situ*-UV-Vis-DR spectra of $\text{V/CeO}_2\text{-P}$ catalyst with $\text{CeO}_2\text{-P}$ as reference white standard recorded at 200 °C after treatment in air (dashed lines) and 45 min in $\text{NH}_3\text{-SCR}$ feed (solid lines).

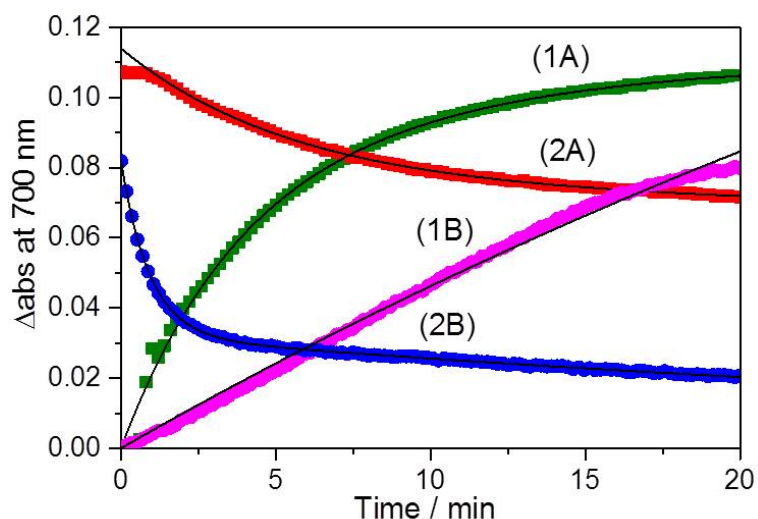


Figure A.25: Difference of absorbance at 700 nm as a function of time for catalysts at 200 °C during reduction in 0.1% NH₃/He and during reoxidation in 5% O₂/He: V/CeO₂-C (1A) and (2A); V/CeO₂-P (1B) and (2B), respectively. Experimental data – coloured symbols, black solid lines – kinetic fits.

Table A.3: Spin Hamiltonian parameters derived by simulation of difference spectra (NO/NH₃/O₂)-(NO/O₂) (Line C3-fit and P3-fit).

	$g_{ }$	g_{\perp}	$A_{ }$ (G)	A_{\perp} (G)	$\Delta g_{ } / \Delta g_{\perp}$	β_2^{*2}
V/CeO ₂ -C	1.922	1.978	182.5	64.0	3.30	0.832
V/CeO ₂ -P	A) 1.922	1.976	185.3	65.7	3.08	0.839
	B)* 1.933	1.967	175.1	55.8	1.96	0.821

* amounts to $\approx 20\%$ of single V⁴⁺ species

Scientific publications

Parts of this thesis have been published:

Journal articles fully related to this work

1. Vuong, T. H.; Radnik, J.; Kondratenko, E.; Schneider, M.; Armbruster, U.; Brückner, A., Structure-reactivity relationships in $\text{VO}_x/\text{Ce}_x\text{Zr}_{1-x}\text{O}_2$ catalysts used for low-temperature NH_3 -SCR of NO. *Appl. Catal., B* **2016**, 197, 159-167.
2. Vuong, T. H.; Radnik, J.; Schneider, M.; Atia, H.; Armbruster, U.; Brückner, A., Effect of support synthesis methods on structure and performance of VO_x/CeO_2 catalysts in low-temperature NH_3 -SCR of NO. *Catal. Commun.* **2016**, 84, 171-174.
3. Vuong, T. H.; Radnik, J.; Rabeah, J.; Bentrup, U.; Schneider, M.; Atia, H.; Armbruster, U.; Grünert, W.; Brückner, A., Efficient $\text{VO}_x/\text{Ce}_{1-x}\text{Ti}_x\text{O}_2$ catalysts for low-temperature NH_3 -SCR: Reaction mechanism and active sites assessed by *in-situ/operando* spectroscopy, *ACS Catal.*, **2017**, 1693-1705.

Additional articles

1. Tran, H. T. T. H.; Kosslick, M.; Ibad, F.; Fischer, C.; Bentrup, U.; Vuong, T. H.; Nguyen, L. Q.; Schulz, A., Photocatalytic Performance of Highly Active Brookite in the Degradation of Hazardous Organic Compounds Compared to Anatase and Rutile. *Appl. Catal., B* **2017**, 200, 647-658.

Contributions in conferences

Oral presentations

1. Vuong, T. H.; Radnik, J.; Kondratenko, E.; Brückner, A., Relations between dynamic redox behavior and catalytic performance of $\text{VO}_x/\text{Ce}_x\text{Zr}_{1-x}\text{O}_2$ catalysts during low-temperature NH_3 -SCR of NO studied by *in-situ* spectroscopy, The Workshop on Ceria- based Materials in Catalysis and Electrochemistry (MCE), Giessen (Germany), July 27-30, **2015**.
2. Vuong, T. H.; Radnik, J.; Armbruster, U.; Brückner, A., Structure-Reactivity relationships in low-temperature NH_3 -SCR of NO over highly effective $\text{V}_2\text{O}_5/\text{Ce}_x\text{Zr}_{1-x}\text{O}_2$ catalysts, 12th European Congress on Catalysis (EuropaCat), Kazan (Russia), August 30 – September 4, **2015**.

3. Vuong, T. H.; Radnik, J.; Rabeah, J.; Bentrup, U.; Armbruster, U.; Brückner, A., Low-temperature NH_3 -SCR of NO over excellent performing catalysts $\text{V}_2\text{O}_5/\text{Ce}_{1-x}\text{Ti}_x\text{O}_2$ studied by *operando* spectroscopies. 19th Northern German doctoral colloquium (NDDK), Hamburg (Germany), September 15-16, **2016**.

Poster presentations

1. Vuong, T. H.; Radnik, J.; Ambruster, U.; Brückner, A., $\text{V}_2\text{O}_5/\text{Ce}_x\text{Zr}_{1-x}\text{O}_2$ - Promising catalysts for SCR of NO with NH_3 at low temperatures, 17th Northern German doctoral colloquium (NDDK), Rostock (Germany), September 11-12, **2014**.
2. Vuong, T. H.; Brückner, A., Catalytic performance and redox behavior of supported $\text{VO}_x/\text{Ce}_x\text{M}_{1-x}\text{O}_2$ catalysts (M = Zr, Ti) during low-temperature NH_3 -SCR of NO studied by *in-situ* spectroscopy, 48th Jahrestreffen Deutscher Katalytiker, Weimar (Germany), March 11-13, **2015**.